The Effect of Magnetic Annealing on Crystallographic Texture, Microstructure and Magnetic properties Development in Fe-2.6%Si

Doctoral Thesis
Dissertation
To be awarded the degree
Doctor of Engineering (Dr.-Ing.)

Submitted by
Mohammed Zakria Salih
From Baghdad, Iraq

Approved by the Faculty of Natural and Materials Sciences
Clausthal University of Technology

Date of Oral Examination
03.04.2014

Chairperson of the Board of Examiners Prof. Dr. Diethelm Johannsmann

Chief Reviewer apl. Prof. Dr. rer. nat. Dr.-Ing. habil. Heinz-Günter Brokmeier

Reviewer PD. Dr.-Ing. habil. Bernd Weidenfeller

Abstract

Compared to other materials silicon steel, also named electrical steel, is a soft magnetic material of prime importance. Due to the increasing needs of a modern society, the electrical industry show has recently an enhanced interest in improving magnetic properties. Hundreds of thousands of tons are produced annually around the world making silicon steel the most produced the magnetic material, in terms of both total tonnage and total market value. Approximately 50% of the electrical energy produced worldwide is used in motors and the necessity of energy conservation interest on the development of high performance magnetic materials. In industrial practice, materials are submitted to many processing steps before they reach the final state in which they become consumer goods. These processing steps not only influence the final shape of the product but also affect the properties of the material such as mechanical, electrical and magnetic properties. Silicon steels are commonly used in hydroelectric power plant generators, transformers, and electrical motors. Also, the magnetic behavior of these materials is mostly controlled by several micro structural features by the final crystallographic texture; grain shape and the final average grain size distribution of a finished steel product are the result of a sequence of events occurring during the thermo-mechanical processing of the steel sheet. The crystallographic texture play an important role in improving the material properties after each processing and heat treatment conditions to reach the final product with optimum properties for best performance.

The present work attempts to investigate the effect of different rolling processes (hot rolling, cold rolling, cold rolling at two stages with intermediate annealing process) at different heat treatments and annealing time, also the effect of magnetic annealing with different external field on the crystallographic texture, microstructure, hardness and magnetic properties of Fe-2.6% Si. Crystallographic textures, magnetic properties and microstructures have been evaluated after each rolling processes and annealing treatments. Due to the coarse grained microstructure after annealing, neutron diffractions is an efficient tool for the analysis of bulk texture of polycrystalline materials. Magnetic annealing at high magnetics fields has influenced the final crystallographic texture through changes in the α, γ, θ and η fiber texture components. Moreover, high magnetic fields have been demonstrated as an important factor to improve the magnetic properties such as high permeability, low power loss and low coercive force.

Abstract

Siliziumhaltige Stähle oder elektrobleche sind weichmagnetische Werkstoffe mit großer Bedeutung für Industrie und Wirtschaft. Mehrere hunderttausend Tonnen werden weltweit jährlich produziert. Damit gehören sie zu den meist produzierten und verkauften magnetischen Werkstoffen weltweit. Etwa 50% der weltweit produzierten Energie wird in Elektromotoren umgewandelt. Dies und die Tatsache, dass mit Energieeinsparungen zumeist erhebliche Kosteneinsparungen einhergehen, zwingen zur Weiterentwicklung von magnetischen Hochleistungswerkstoffen.

Siliziumhaltige Stähle werden zu großen Teilen in Generatoren zur Energiegewinnung und in elektrischen Motoren verwendet. Die magnetischen Eigenschaften werden maßgeblich von zwei mikrostrukturellen Merkmalen beeinflusst: der Textur und der durchschnittlichen Korngröße.

Die vorliegende Arbeit untersucht den Einfluss verschiedener Walzprozesse (Warmwalzen, Kaltwalzen und Kaltwalzen in zwei Schritten mit Zwischenwärmebehandlung) bei verschiedenen Glühtemperaturen und -zeiten sowie den Effekt der Glühung in magnetischen Feldern auf die Gefüge- und kristallographische Texturentwicklung und deren Einfluss auf die magnetische Eigenschaften in Fe-2.6%Si Stahl.

Nach jedem Prozess- und Wärmebehandlungsschritt wurde die Entwicklung der Textur und des Gefüges mit Hilfe von lichtmikroskopischen Untersuchungen und Neutronenstreuexperimenten bewertet. Zusätzlich wurde der Einfluss auf die magnetischen Eigenschaften des Werkstoffes untersucht.

Glühungen in starken magnetischen Feldern wirken sich auf die kristallografische Textur aus. Dies zeigt sich in quantitativen Änderungen der α-, γ-, θ- und η Fasertexturkomponenten, was einen Einfluss auf die magnetischen Eigenschaften hat.

Es konnte gezeigt werden, dass starke magnetische Felder während einer Glühbehandlung zur Verbesserung bestimmter magnetischer Eigenschaften (hohe Permeabilität, geringe Koerzitivkraft) beitragen.

Neutronenstreuung eignet sich hervorragend zur Globaltexturanalyse von polykristallinen Werkstoffen mit grobkörniger Mikrostruktur.

Acknowledgements

This thesis has been submitted in partial fulfillment of the requirements for a doctoral degree in the Faculty of Natural and Materials Science of Clausthal University of Technology in Germany. This research was carried out between October 2010 to March 2014 supported between the Iraqi Ministry of Higher Education and Scientific Research (MOHESR) and Deutscher Akademischer Austausch Dienst (DAAD) through A/09/97961.

I would like to express my sincere regards for and gratitude to my supervisor Prof. Dr. Heinz-Günter Brokmeier at TexMat, for his patience, support, encouragement and guidance during the period of this work.

I am also grateful to the useful discussions with Dr. Bernd Weidenfeller and also for his helps for measuring the magnetic properties of my samples.

Thanks very much for Prof. Dr. Diethelm Johannsmann chairing my oral examination.

I would like to thank Dr. Jonathan Paul for his carefully reviewing my thesis.

I am grateful to the permission of the measurement beam time at, Stress-Spec (FRMII, Münich), PETRAIII (Desy, Hamburg) for giving me a chance to measure my samples.

I am also very grateful to Prof. Dr. F. Pyzak for measuring my samples by TEM and useful discussion with him.

I would like to thank Prof. Dr. Jochen Wonsitza to the permission for preparing my samples at Dresden High Magnetic Field laboratory, Helmholtz-Zentrum Dresden-Rossendorf (HZDR) and also I would like to thank Dr. M. Uhlarz for help and useful discussion with him.

Sincere grateful and thanks are also shown to colleagues at HZG (Helmholtz Zentrum Geesthacht).

I must show my sincere thanks to my colleagues PhD Candidate N. Al-hamdany, Dr. Emad Maawad, Dr. W. Gan, PhD Candidate Z.Y. Zhong, PhD Candidate Marcus Rackel, Mr. J. Schumann, Mr. P. König, and Mr. Falk Dorn, for their kind helps and nice discussions during experimental procedure.

Finally, special thanks are given to my father, mother, brothers and my sister for their patience and efforts to me during my studying at Germany.

Table of Contents

1 Introduction and Aims 1
1.1 Introduction 1
1.2 Aims and Objectives 7

2 Literature Survey and Theoretical Principles 9
2.1 Introduction 9
2.2 Iron 9
2.3 History of Magnetic Materials 12
2.4 Iron-Silicon 13
2.5 Electric Steels Composition 16
2.6 Magnetic Properties and Microstructural Factors 18
2.7 Crystallographic Texture 20
2.7.1 Pole Figure 21
2.7.2 Orientation Distribution Function (ODF) 22
2.8 Texture Measurement 27
2.8.1 X-ray 27
2.8.2 Neutron Diffraction 29
2.8.3 Synchrotron Diffraction 32
2.9 Crystallographic Texture in Iron Silicon Alloy 35
2.10 Magnetic Materials and Loop Hysteresis Loops 39
2.11 Magnetic Annealing 43
2.12 The Dislocation Density Evaluated By Hard X-ray Diffraction 45

3 Materials and Methods 47
3.1 Introduction 47
3.2 Materials 47
3.2.1 Hot Rolling 47
3.2.2 Cold Rolling at One Stage 47
3.2.3 Cold Rolling with an Intermediate Annealing Processes 48
3.3 Magnetic Annealing Measurment 48
3.4 TEM Measurment 51
3.5 Metallographic Sample Preparation 51
3.6 Chemical Etching 51
3.7 Bulk Crystallographic Texture by using Neutron Diffraction 52
3.8 Dislocation Density Evaluation by using Monochromatic Synchrotron Radiation 54
3.9 Hardness 55
3.10 Measuremnt of Magnetic Properties 56

4 Results and Discussions 57
- 4.1 Introduction 57
- 4.2 Texture and Microstructure Evolution 58
  - 4.2.1 As-Received (Hot rolling) 58
  - 4.2.2 Cold Rolling at one stage 62
  - 4.2.3 Cold Rolling Plus Different Annealing Temperatures for 20 min 65
  - 4.2.4 Cold Rolling Plus Different Annealing Temperatures for 60 min 70
  - 4.2.5 Grain Size 75
  - 4.2.6 Two Stages Cold Rolling with Intermediate Annealing Processes 75
  - 4.2.7 Magnetic Annealing at different External Field (0, 7, 14) Tesla 82
- 4.3 Dislocation Density 89
- 4.4 Magnetic Properties 93
- 4.5 Hardness 99

Conclusions and Recommendations 101

References 105

1. Introduction and Aims

1.1 Introduction

Industrial statics have shown that the largest tonnage of magnetic materials is consumed in the form of sheets or strips. Thus, rolling is an extremely important processing technique in this industry. During production the materials are put under so many processing steps before they reach their final form where they become consumer goods. Manufacturing begins with the melting of raw elements to obtain the desired alloy composition; follow by casting of the melt in to large ingots (metal that is cast in the shape of a block for convenient handling). The ingots are then subjected to a series of rolling steps, initially at elevated temperature for easy "reduction" of the ingots. Intermediate annealing is required of products such as plates, slaps and billets [1]. Additionally, cold rolling could be used at the end of the forming process depending on the end product, which is depending on [1]:

1. The crystals structure.
2. The grain structure and the mechanical behavior of the intermediate products
3. The specified metallurgical conditions of the final products.

Different metals and alloys have been used for many applications due to excellent specific properties that can be obtained via a wide variety of thermo-mechanical process. There are many microstructure sensitive physical properties such as electro-magnetic properties (e.g. permeability, coercive force, power loss, magnetostriction) and mechanical properties (e.g. Young's modules, yield strength, tensile strength). There are several ways to change the microstructure sensitive properties of metals such as (changing the chemical composition, optimizing the thermo-mechanical process parameters and changing the deformation and annealing parameters) as schematically illustrated in Fig. 1.1.

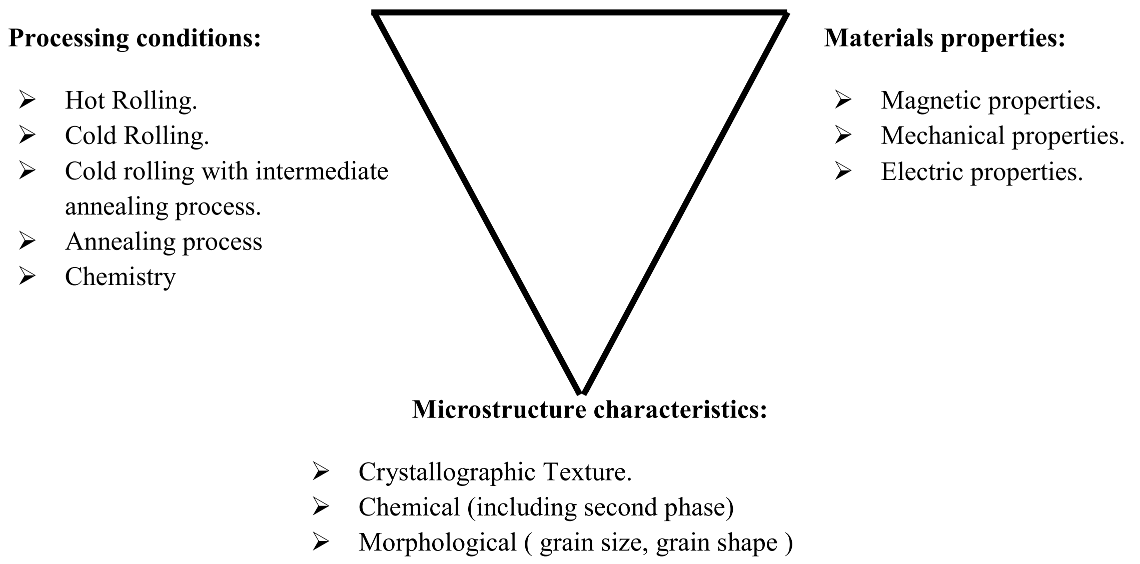

Processing conditions:

- Hot Rolling.
- Cold Rolling.
- Cold rolling with intermediate annealing process.
- Annealing process
- Chemistry

Materials properties:

- Magnetic properties.
- Mechanical properties.
- Electric properties.

Microstructure characteristics:

- Crystallographic Texture.
- Chemical (including second phase)
- Morphological (grain size, grain shape)

Figure 1.1: The materials science triangle showing structure sensitive properties of metals

Magnetic materials have been divided into:

1. **Hard magnetic** materials are utilized in permanent magnets, which produce a magnetic field in particular volume of space. There are two ways to produce a magnetic field: i) by current in a conductor or ii) by poles in a magnet. According to the hysteresis behavior, hard magnetic materials are characterized by a high coercivity ($100 \leq H_c \leq 30000$ Acm^{-1}), high remanence and saturation flux density as well as a low initial permeability and high power loss. For many applications a permanent magnet is the better choice, because it provides a constant field without the continuous use of electric power and without the generation of heat. The most common alloys for hard magnetic materials are (Cunife (Cu-Ni-Fe) alloys, Alnico (Al-Ni-Co) alloys, hexagonal ferrites (BaO-$6Fe_2O_3$), Samarium-Cobalt magnets ($SmCo_5$) and Neodymium-Iron-Boron magnets ($Nd_2Fe_{14}B$)).

2. **Soft magnetic** materials are utilized in applications that are subjected to alternating magnetic fields such as transformers, magnetic amplifier, inductors, generators and motors. The frequency required to operate these magnetic devices ranges between 10 to 50/60 Hz (only technical frequencies in Europe / USA and electrical steel). The characteristic of soft magnetic are: low coercive force ($0.001 \leq H_c \leq 1$ Acm^{-1}), low power loss and high permeability. There are two types of soft magnetic materials the choice of which depends on the application and requirements. Firstly, ferromagnetic materials are based on Iron-Silicon, Nickel-Iron and cobalt-Iron alloys, and are utilized for lower frequency <2 kHz. Secondly, ferromagnetic materials can be based on ceramic oxides which are compounds of iron oxides, Fe_2O_3 mixed with one or more oxide of metals such as (FeO, NiO, MgO, CuO, BaO, CoO and

MgO). Typically, these types of ferromagnetic materials are utilized for high frequency between 2kHz to 80 MHz [2].
The main factors affecting on the magnetic properties for ferromagnetic materials are:

- Chemical composition.
- Fabrication methods.
- Heat treatments.
- Temperature.
- Crystal structure.
- Crystal orientation.
- Dislocation contents.
- Impurities.
- Grain boundaries.

Magnetic properties such as permeability, coercive force and power loss are usually very sensitive and show extremely changes when a change is made to either chemical composition, fabrication process or heat treatment is varied.

The permeability is defined the response of a medium to magnetic fields; it is an expression for a proportional relationship between the flux density (B) in medium to the external field strength (H).

The coercive force or coercivity is defined as a measure of the magnitude of ferromagnetic materials as expresses by disappear of the flux density (B) during applied the external field (H).

There are many factors that influence permeability and coercive force such as heating and cooling rate, temperature, impurities, surface oxidation, cutting stress (inducing dislocations) and nitration in the final annealing [3]. The heating and cooling rate are very important factors to influence permeability and coercive force. The permeability will be reduced after increased the plastic deformation due to the internal strains that are generated during plastic deformation processes such as rolling, deep drawing or extrusion. The internal strains can usually be relieved by recovery annealing process. If the iron specimen is cooled and heated at very slow rates, the internal strains caused by the change in structure will be relieved by diffusion of the metal atoms. However when the iron specimen is very rapid by cooled there will not be sufficient time for strain relief [1, 2]. The temperature is influencing permeability even no change in phase occurs.

The magnetic materials should be included some elements such as carbon, oxygen and nitrogen to improve the magnetic properties and crystallographic texture. However, the level of such impurity elements affects magnetic properties. The impurities play an important role and effects on the permeability and coercive force. When the level of impurities is decreased the permeability will be increased and the coercive force decreases [1, 2].

The magnetic properties of soft magnetic materials such as silicon steel are strongly dependent on recrystallization and grain size morphology generated after hot and cold roll processing. The grain size of the silicon steel and low concentration of structure effect such as impurities, dislocations, grain boundaries and precipitates are the most important factors determining power loss. Thus, grain size optimization has attracted the interest of many researchers and therefore has almost reached its limit via control of chemical composition and processing parameters associated with hot, cold rolling and annealing temperature [4]. However, other factors that affect the magnetic properties such as atomic arrangement, domain walls, misorientation of the grain boundaries and the structure of grain boundaries still have room optimization.

According to the Weiss theory [5] ferromagnetic materials in the demagnetized state are divided in to a number of small regions called magnetic domains. For each domain all the atomic moments are aligned in one of the easy directions. Therefore, spontaneous magnetization does exist [1, 2]. The magnetic moment of any one domain is specified by the magnitude and direction of the magnetization and by its volume. Changes in the magnitude of the spontaneous magnetization are affected by changes in temperature or by high external magnetic fields during heat treatment [1, 2].

Usually at constant temperature the moment of domain and the magnetization of ferromagnetic materials can be changed by:

1. Changing the direction of domain magnetization or
2. Changing the domain volume.

Figure 1.2 shows a schematic representation of the domains structure of iron. Initially before applying the external field (*H*) all the domain have a random orientation (see figure 1.2a), when the external field (*H*) increasing until the domains will be change the size and shape of the domains via movement of domain boundaries (see figure 1.2 b and c), this process continues with increasing external field (*H*) until the domains are saturated and then all the domains have become oriented toward the direction of the external field (*H*).

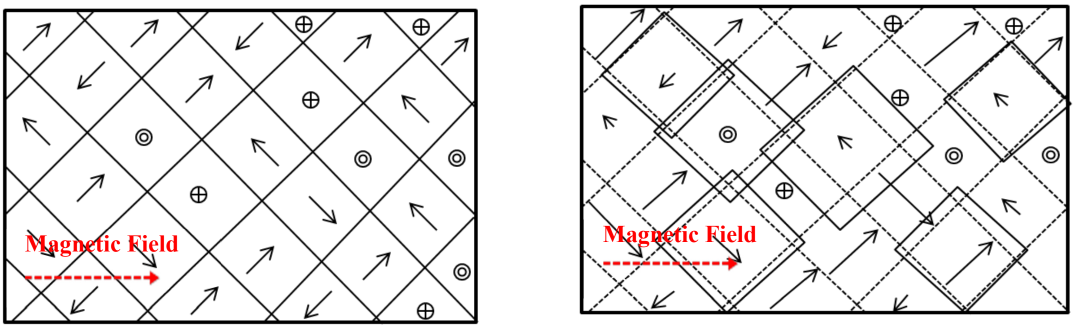

a) Demagnetzied **b)** Partial Magnetization

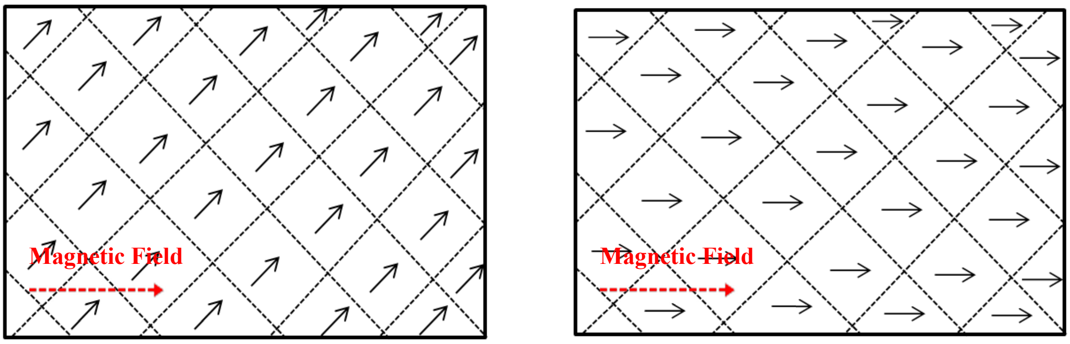

c) Complete magnetization **d)** Saturated

Figure 1.2: Schematic digram showing the domain structure in iron-silicon [2].

The crystal structure and strain are other factors that affect the direction of domain magnetization. Particularly the external field is absence. Low energy loss and coercive force combined with high permeability in soft magnetic materials can be attained by orienting the grains along their <100> axes which is the axis of easy magnetization. This crystallographic direction should be aligned along the applied magnetic field direction. Specific crystallographic texture is usually required in the magnetic materials applicants that affected on specific magnetic properties such as permeability, power loss, coercive force and conductivity. The crystallographic texture and specific of magnetic properties for the magnetic materials must be developed through a series of hot and cold rolling procedures that include some heat treatments between rolling process.

Soft magnetic materials such as Iron silicon are the most well-known examples for the use of crystallographic anisotropy in transformer core materials, as indicated in Fig. 1.3. The magnetic flux in a transformer core is runs in two alternately perpendicular directions. A high permeability of the core sheet is thus required only in these two directions. When the transformer core sheet material has a cubic structures (bcc) with the direction of easiest magnetization in the <100> direction then the cube {001}<100> component texture would provide the best magnetic properties [6].

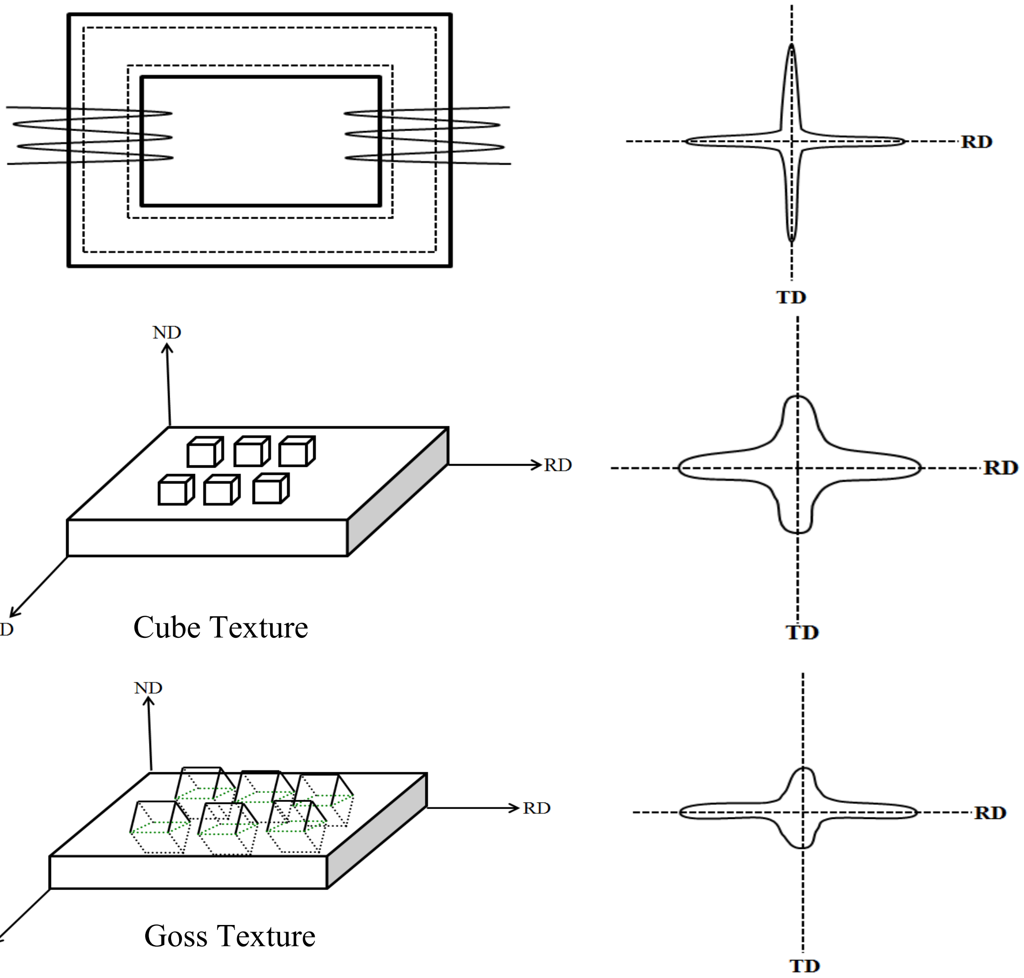

Figure 1.3: The application profile of transformer core sheet compared with the property profiles of the Cube and Goss texture materials [6].

This type of texture component can be obtained in Fe-Ni alloys (fcc). However, in Fe-Si alloys the cube texture is difficult to produce. It is much easier to obtain the Goss-texture {011}<100> which has the second best property profile. The Goss texture is obtained by sophisticated technology involving hot rolling followed by primary and secondary recrystallization [1]. Low energy loss, low coercive force and high permeability in electric steel can be further developed reached by orienting the grains into the <001> direction which is the direction of easy magnetization. This crystallographic direction is then oriented in a transformer in the direction of the applied magnetic fields.

1.2 Aims and Objectives

- Study the influence of different types of rolling on Fe-2.6% Si (97% hot rolling, 75% and 90% cross cold rolling) and the related on crystallographic texture.
- Study the influence of different annealing temperatures and times for 90% cross cold rolled Fe-2.6% Si after on crystallographic texture and magnetic properties.
- Study the influence of the thermo-mechanical process (two stages cold rolling with intermediate annealing) of Fe-2.6% Si on the crystallographic texture and magnetic properties.
- Study the influence of annealing under different external applied fields (magnetic annealing) after thermo-mechanical process (two stages cold rolling with intermediate annealing process) on crystallographic texture and magnetic properties of Fe-2.6% Si.
- Microstructural evolution of Fe-2.6% Si after different rolling and annealing processes, and after magnetic annealing.
- Evaluation of the defect density in Fe-2.6%Si using modified Williams and Hall method after different rolling processes using hard X-ray (synchrotron).
- Texture developments in Fe-2.6% Si after different rolling and annealing processes have been characterized by neutron radiation since neutron diffraction is powerful for bulk texture analysis.
- Evaluation of magnetic properties such as permeability, coercive force and power loss using digitals hysterias device.

2. Literature Survey and Theoretical Principles

2.1 Introduction

The main aim of this chapter is to briefly introduce a literature survey on types of silicon steel and various types of processes used to enhance the crystallographic texture and magnetic properties such as power loss, permeability and coercive force. Furthermore, a brief introduction to crystallographic texture, texture measurement, magnetic materials, magnetic history loops and magnetic annealing is given.

2.2 Iron

Iron is a chemical element with the symbol Fe, atomic number 26 and at space group Im-3m (space group number: 229). It is a metal in the first transition series. It is the most common element on the planet earth forming much of Earth's outer and inner core. Pure iron, upon heating, has two changes in crystal structure before melt. At room temperature the stable modifiable, called ferrite, or α-iron, has a bcc crystal structure as shown in Fig. 2.1. Ferrite bcc (α-iron) transforms to austenite fcc (γ-iron) at 912°C and δ (bcc-iron) at 1394°C. The physical properties of Fe are listed in table 2.1.

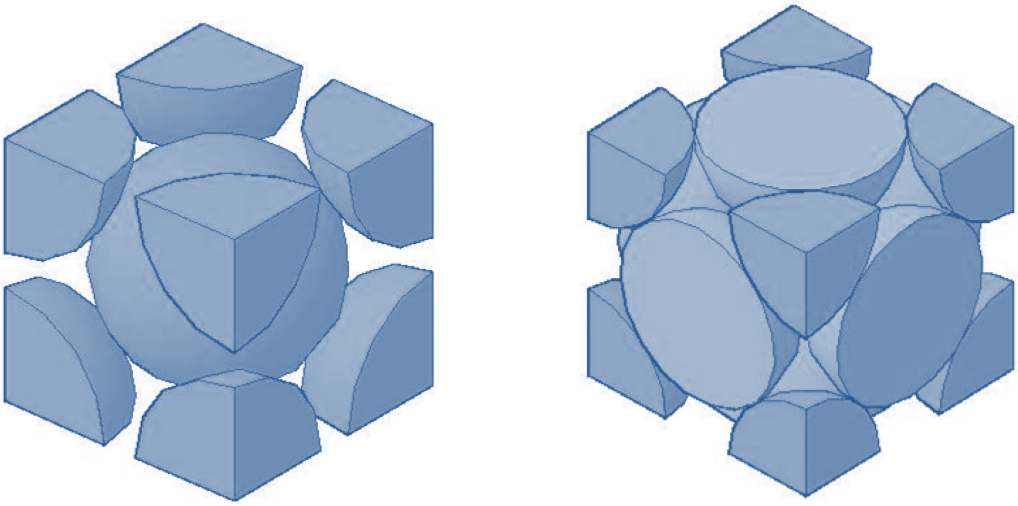

a) BCC **b) FCC**

Figure 2.1: Atomic arrangement in **a)** Body- Centered Cubic structure (ferrite) **b)** Face-Centered Cubic structure (austenite)

Table 2.1: Physical properties of Fe

Melting points	1538°C
Boiling points	2862°C
Latent heat of fusion	13.81 kJ.mol^{-1}
Latent heat of evaporation	340 kJ.mol^{-1}
Young's modules	211 GPa
Shear modules	82 GPa
Poisson ration	0.29
Electrical resistivity at 20°C	96.1 Ωm/cm
Thermal conductivity at 20°C	80.4 Wm^{-1}K^{-1}
Linear coefficient of thermal expansion at 20°C	11.8 µm.m^{-1}.k^{-1}
Density (solid) at 20°C	7.869 g mm^{-3}

Slip systems in crystals are defined by combinations of slip planes and slip directions. In austenite, an fcc crystal structure, the slip planes are the {111} planes and the slip directions are the face diagonals of the unit cell or the <110> directions. There are four equivalent {111} planes, each with three <110> directions, making a total of 12 slip systems in austenite. The Burgers vector of perfect dislocations in austenite is $a\sqrt{2}/2$, where *a* is the lattice parameter of the fcc unit cell [7].

In bcc ferrite, the slip directions are the body diagonals of the unit cell or <111> directions, and the slip planes have been found to be {110}, {112}, and {123} planes, all of which contain <111> directions, for a total of 48 slip systems. The Burgers vector of dislocations in ferrite is $a\sqrt{3}/2$ [7]. The pencil glide for bcc structure is <111> directions, this term means that the slip can occur on any plane that contains a <111> slip direction.

Steels have specific limitation of carbon, manganese, silicon, copper, phosphorus, sulfur and minimum quantities of silicon, aluminum, chromium, cobalt, niobium, molybdenum, nickel, titanium, tungsten, vanadium, zirconium, or any other element added to obtain a desired alloying effect [8]. For example the different grades of both high-manganese and Cr-Ni austenitic steels offer an exceptional combination of high-strength and ductility compared to conventional and advanced bcc lattice-based steels as shown in Fig. 2.2.

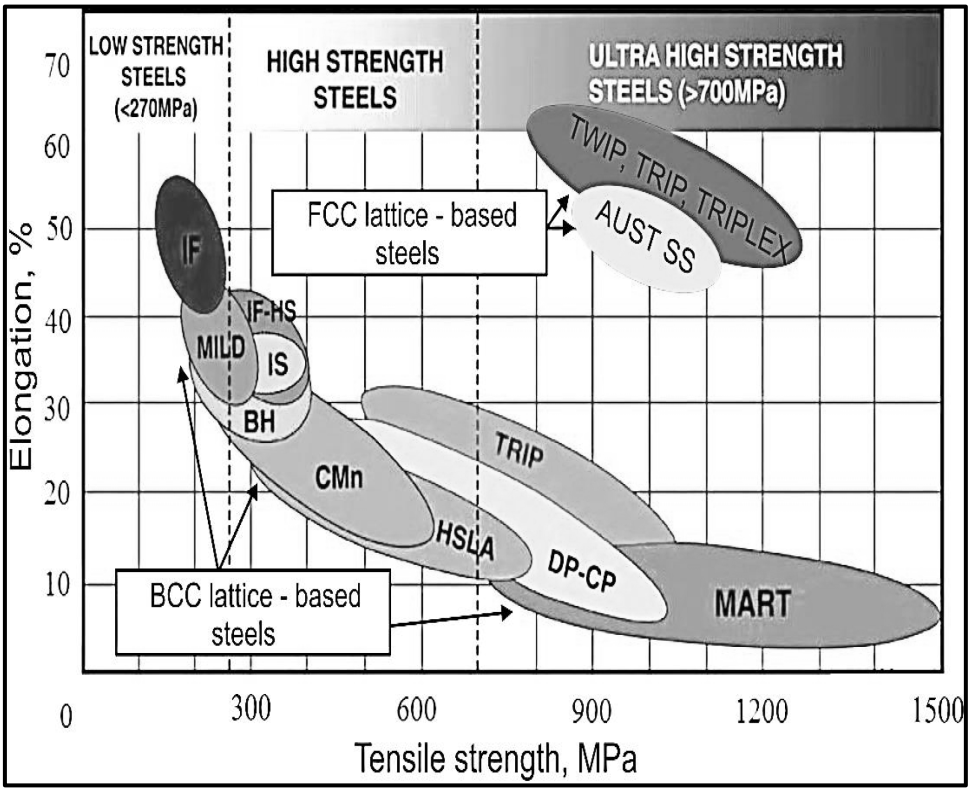

Figure 2.2: Schematic comparison of mechanical properties of conventional and advanced ferrite and austenitic alloys (International Iron & Steel Institute, 2006).

The technological formability of austenitic alloys and their unique mechanical properties arises from the great capability of γ phase to plastically deform, during which dislocation glide system or strain induced martensitic transformation (TRIP Transformation Induced Plasticity) and mechanical twinning (TWIP Twinning Induced Plasticity) can occur. TRIP steels have a triple phase microstructure based on ferrite, bainite and austenite. During plastic deformation the austenite phase transform in to martensitic phase that results in enhancement of mechanical characteristic such as strength and ductility. For this reason TRIP steels are normally used in the automotive industry. The mechanical properties that can be obtained as shown in Fig. 2.2 result from the high work hardening rate characterizing the plastic deformation of austenitic alloys. The delaying necking during straining is the result of the high ductility. When local necking takes place, strain induced martensitic transformation occurs in TRIP steels and deformation twins are generated for TWIP steels in the locally deformed areas. This leads to intensive local strain hardening of the steel and further plastic strain proceeds in less strain hardened contiguous zones. The situation is repeated in successive regions of the material and finally leads to delaying necking on a macro scale and high uniform and total elongation [9, 10].

Electrical steel comprises of a large family of steels, generally called soft magnetic materials. Without electrical steel the economic generation, distribution & utilization of electricity would not be practical. The wide diversity of electrical machines, equipment and systems requires specific electromagnetic and mechanical behavior of the transformer core material. The designers can select optimum steel grades required for standard high permeability and lowest core losses in applications ranging from micro motors to power generators and transformers, Fig. 2.3 show the standard production route for electric steels.

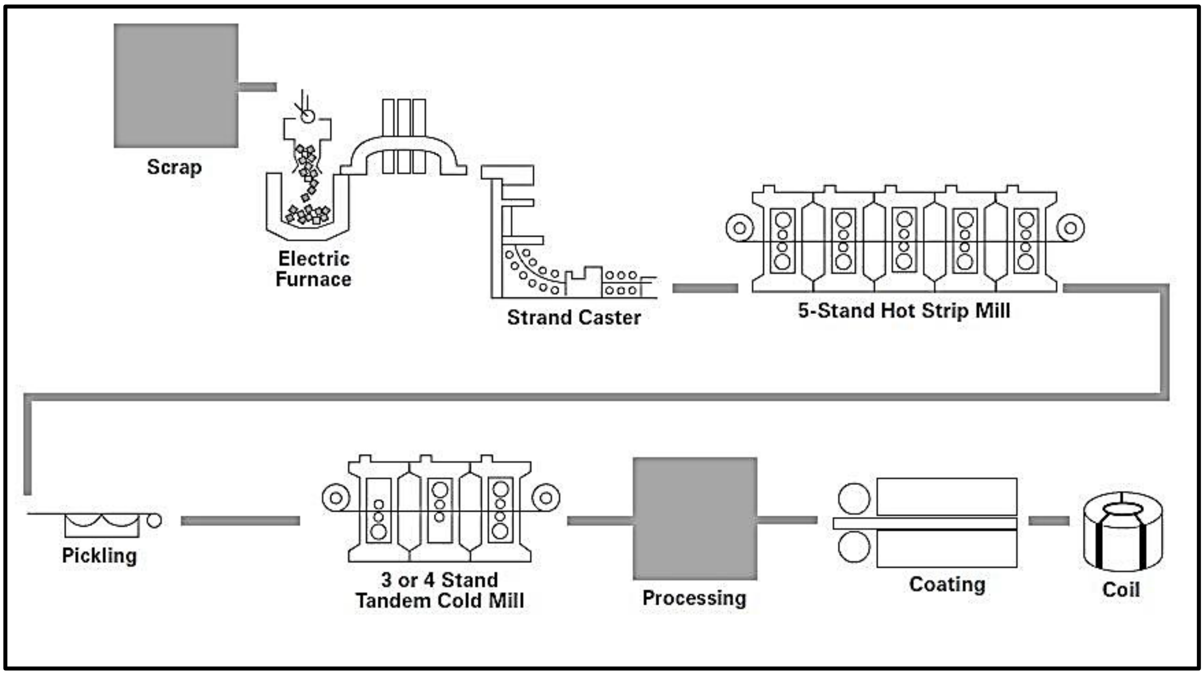

Figure 2.3: Manufacturing route for production of Electrical steels [ThyssenKrupp]

2.3 History of Magnetic Materials

The history of the evolution of magnetic materials is certainly long and splendid. According to the history of Asia Minor, a cradle of civilization, lodestone was found to be a natural magnet in Magnesia more than 3500 years ago. The stone was called magnes lapis, which means Magnesian stone "Magnet" and "magnetism" were originated from the word "Magnesian". Thales of Miletus, the Greek philosopher, stated that the magnetic interaction between a magnetic field and iron was known before 600BC. Modern Chinese historians have shown evidence that the world's first compass (a south pointing lodestone spoon balanced on a round bronze square plate) was invented in China about 85 AD [1, 7-13].

Magnetic materials also played a prominent role in the discovery of the New World and in the evolution of modern technology. Without the compass Christopher Columbus would not have made his voyages and discoveries. The excellent magnetic properties and low production cost of iron have made it possible to generate inexpensive electricity on a massive scale since 1886 when Westinghouse Electric Company built the first commercial alternating current generation station at Buffalo, New York [1].

The use of magnetic materials to perform vital function is not limited to the utility industry, other industries consuming considerable amounts of magnetic materials include communication, computer, audio-visual and home appliances [1, 7-13].

2.4 Iron-Silicon

Alloys of iron and silicon are of main significance in the electrical industry. Silicon steel, electrical steel or iron silicon is a soft magnetic material extensively utilized for electrical applications due to its high permeability and low power loss and low coercive force. Productions of electric steels are about 1% of the world wide steel production. In spite of these low percentage electric steels is one of the most important materials for electromagnetic components, which are essential for the function of electrical components [11]. The electrical steels belong to the group of the soft magnetic materials, which also include the crystalline or amorphous materials as well as nanocrystalline FeNi or FeCo based alloys, soft magnetic ferrites, soft magnetic sintered materials and soft magnetic powder composites[1-2, 11, 16]. Soft magnetic materials are generally utilized to increase and conduct the magnetic flux inside electromagnetic components. Figure 2.4 shows the worldwide market for electrical application of the soft magnetic materials according to the fabrication quantity and the production amounts.

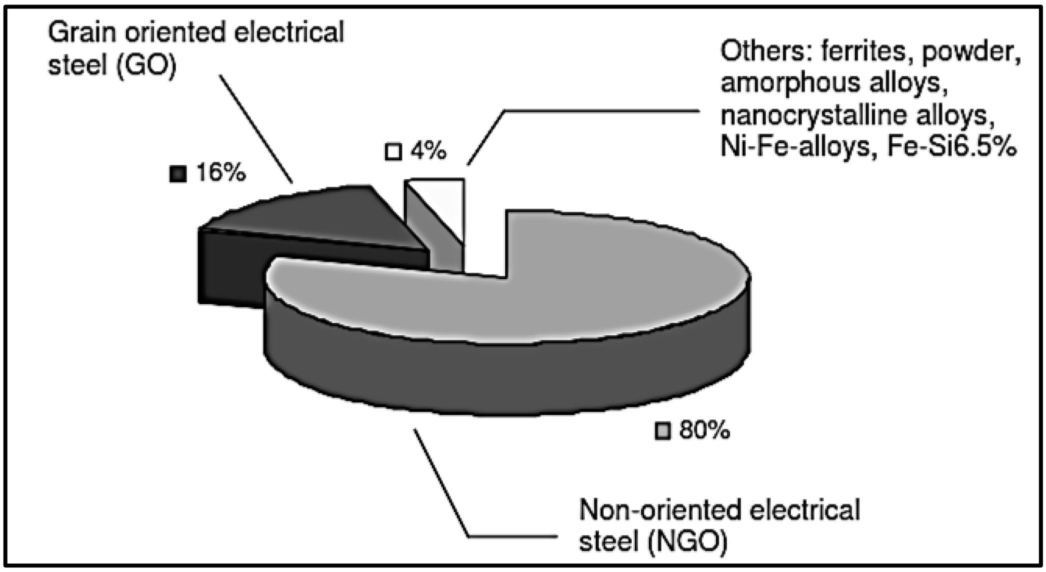

Figure 2.4: Worldwide market for soft magnetic materials (2006) [19]

Silicon steels are representative soft magnetic materials which can effectively convert electricity into magnetic energy, and are silicon steels are utilized as core materials of electrical power appliances. There are two different types of silicon steel Grain Oriented (GO) and Non Grain Oriented (NGO) silicon steel as shown in Fig. 2.5.

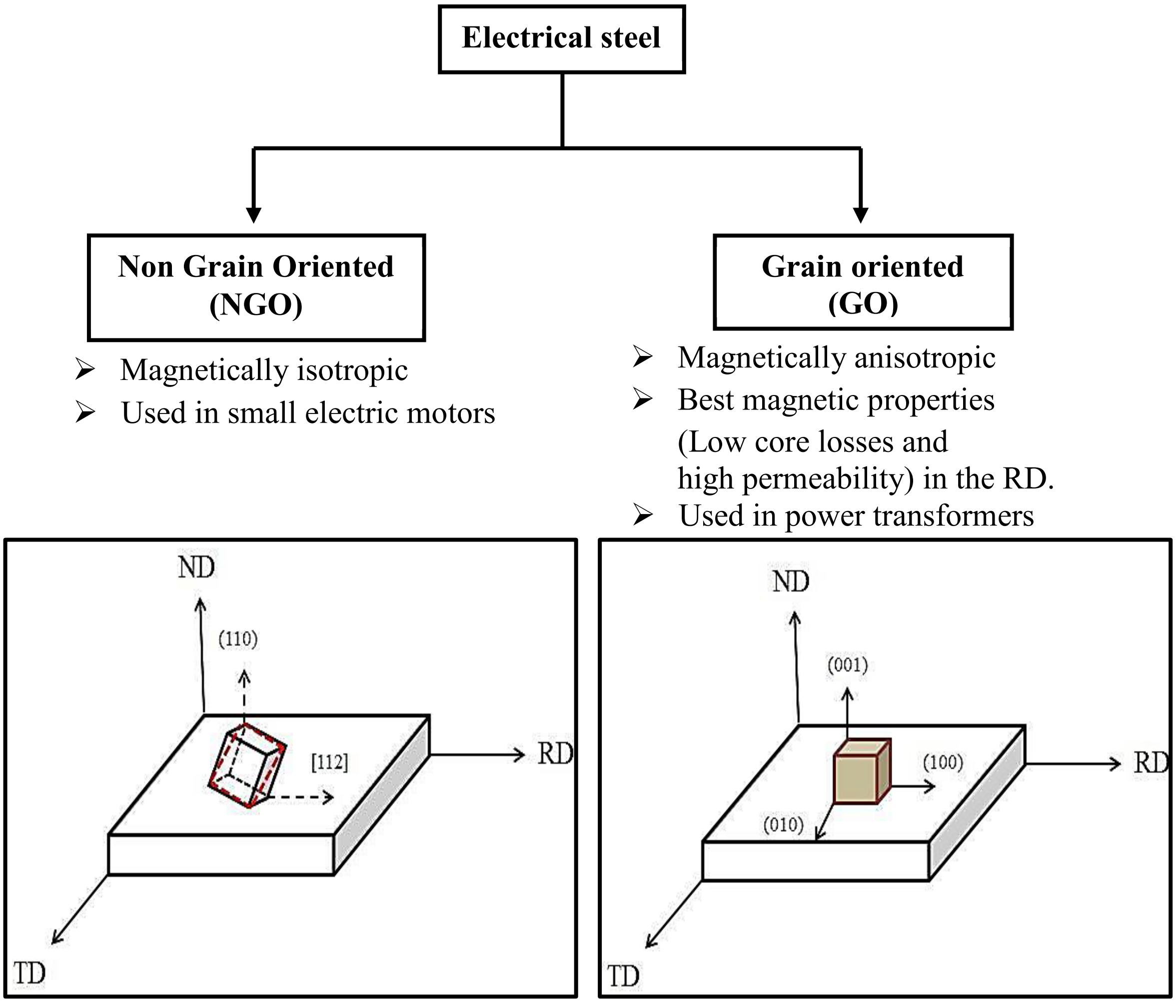

Non Grain Oriented (NGO):

- Magnetically isotropic
- Used in small electric motors

Grain oriented (GO):

- Magnetically anisotropic
- Best magnetic properties (Low core losses and high permeability) in the RD.
- Used in power transformers

Figure 2.5: The two main types of electrical steels employed in electrical device

The silicon steels are subdivided into:

1. Grain oriented (GO commercially name for materials used in transformer) materials which have optimum magnetic characteristics in the rolling direction. Usually, grain oriented steels are utilized mainly for transformers. In 1935, Norman P. Goss reported a thermomechanical procedure to obtain silicon steel sheets with a very high crystallographic texture, {110}<001>, also known as Goss texture [14]. Silicon steels having high Goss texture components are called grain oriented and are mainly used as the core material for power and distribution transformers where the magnetic flux is unidirectional. The Goss texture is a very attractive component of crystallographic texture because it has the <100> direction, recognized as an easy direction of magnetization, parallel to the rolling direction. Therefore, the cutting and assembling of the GO silicon steel sheets in a transformer must be designed so that the direction of the magnetic flux is along the rolling direction of the sheet.

2. Non-Grain-oriented (NGO commercially name for materials used in generators and motors) materials have been processed so that the specific magnetic characteristics are developed in the sheet. Usually, grain non oriented materials are utilized for generators and motors. Grain non-oriented silicon steel does not present a very high Goss texture and has its main technological application in rotating electrical machinery in which the magnetic field is in the plane of the sheet, but the angle between the field and the rolling direction is variable [11]. Although GO silicon steel has attracted more academic interests, NGO steels represent the highest tonnage of electrical steels being produced today [11-13]. For the case of rotating machines, there is no point in having the easiest direction of magnetization, <100>, parallel to the rolling direction and an adequate texture would be (100)[uvw], also known as [100] fiber texture [16], where most of the grains would have their {100} planes parallel to the plane of the sheet. The types processes of grain non oriented steel (NGO) are subdivided into:

1. The fully processed electrical steel: The process steps for fully processed non-grain-oriented steel (NGO) include casting, hot rolling, cold rolling in one step or cold rolling in two or more steps with an intermediate annealing process, final annealing and coating.

2. The semi-processed: The process steps for semi-processed material involved a temper rolling following annealing and a final annealing. The final step of production step, performed by the customer, consists of a final annealing treatment that is used to improve the magnetic characteristics. This is also carried out in order for decarburization, reduction of residual stresses and grain growth in order to obtain optimum magnetic characteristics. The effects resulting from the technological variation within the fabrication process on the structural features of grain non oriented steels such as inclusions, grain size and texture are not completely known, therefore providing therefore, a considerable potential for new solutions to improve the material properties [11]. The applications of electrical steel comprise electrical machines and devices for the generation of energy and their distribution as well as the utilization of electric energy in the public and private industrial sectors. The importance of electrical steels in the market is strongly connected with developments in the fields of power generation and distribution, industrial equipment likes pumps, compressors and fans, air conditioning and coolers, illumination engineering automatization, transport engineering, white goods and household equipment, electromagnetic components for audio, video and computer applications [11].

2.5 Electrical Steels Composition

Electrical steels are iron alloys with a Si content between zero and 6.5wt% as the main alloying element; other alloying elements being Al and Mn are added in order to increase the resistivity and hence to reduce eddy current losses, Mn is required to tie up free sulphur from the iron matrix. These steels, also referred to as Fe-Si steels, are soft magnetic materials because of the limited corrective field. Soft magnetic materials are ferromagnetic materials which display their ferromagnetism in the presence of an applied magnetic field and are easy to be magnetized and demagnetized [16].

The expression "soft magnetic material" comprises a wide family of materials such as metallic materials, ferrites, compounds, amorphous or nanocrystalline materials and thin films. The reduction of power loss by an addition of silicon in iron was discovered by Hadfield [20, 21]. The commercial production of silicon steel as soft magnetic materials started in 1903 in Germany and then in USA in 1906 [22]. The addition of silicon into iron leads to important changes in the magnetic characteristics and other physical and mechanical properties. Two of the major advantageous effects of silicon addition to iron on the magnetic properties are [23]:

1- Electrical resistivity increases, leading to a noticeable reduction in classical eddy currents and consequently in losses.
2- Crystal anisotropy decreases, causing an increase in permeability.
The addition of silicon in iron greatly modifies the phase changes leading to an increase in the $\alpha \rightarrow \gamma$ transformation. The $\gamma \rightarrow \delta$ transformation temperature is also lowered by the addition of silicon to iron. The above remarks apply however only to pure Fe-Si alloys.

In addition to the effect of silicon on the magnetic properties, aluminum also changes the magnetic properties by increasing electrical resistivity; these two elements are usually used in ranges up to 3.5% and 0.5%, respectively.

Silicon addition has also some disadvantages. It leads to a decrease of the saturation induction and tends to make the alloy brittle; making the material difficult to roll the material into sheet when the silicon content is around 5% or higher [16].

Figure 2.6 shows the effect of silicon on crystal anisotropy (K_1), saturation induction (B_S), resistivity (ρ) and percent of elongation.

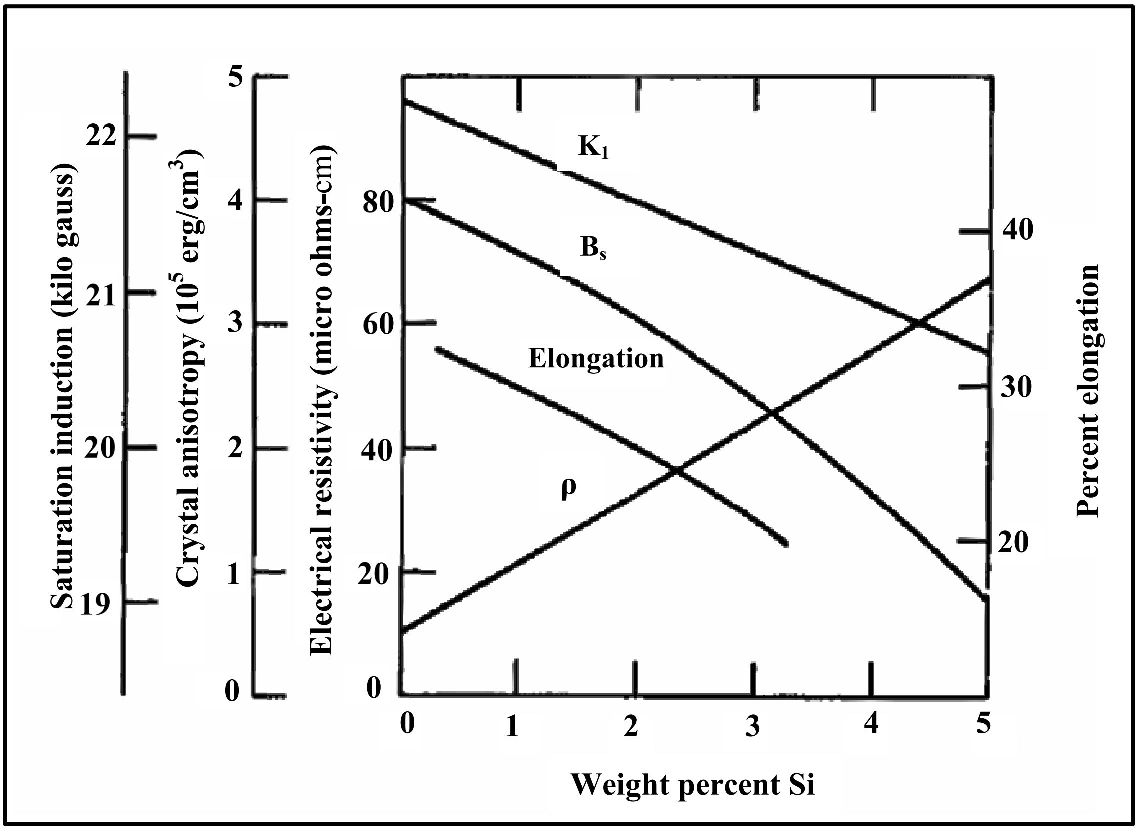

Figure 2.6: Effect of silicon on crystal anisotropy (K_1), saturation induction (B_S), resistivity (ρ) and percent of elongation for a non-oriented sheet [16]

Figure 2.7 shows the iron-silicon phase diagram, iron-silicon alloys with between 3-10 at.% Si no phase transformation occurs. Iron that contains 3-10 at.% Si always remains ferritic up to melting and recrystallization after the deformation is the only method of producing a completely new grain structure with a modified crystallographic texture and grain size.

Below 800 °C the solid solubility of silicon in α iron extends to about 10 at.% Si, above 10 at.% Si the phase α_1, α_2 ($Fe_{11}Si_5$) and η have been observed. The η has been identified as Fe_5Si_3 at 32 at.% Si contains, the η phase is stable only between 825 °C-1030 °C [2].

The solid solution area of greatest practical important for magnetic phenomena (single phase γ), only occurs in alloys containing less than 5 at.% Si and at temperatures between 912 and 1394°C. However, the existence of a few percent of carbon may extend the two-phase (α + γ) domain and extend the boundary between (α + γ) and α to beyond 5 at.% Si [2]. For this reason the annealing is usually carried out just below 800°C. The carbon content of silicon steel ranges from about 0.003% (non-oriented steel) to 0.001% (oriented Fe-Si) [7].

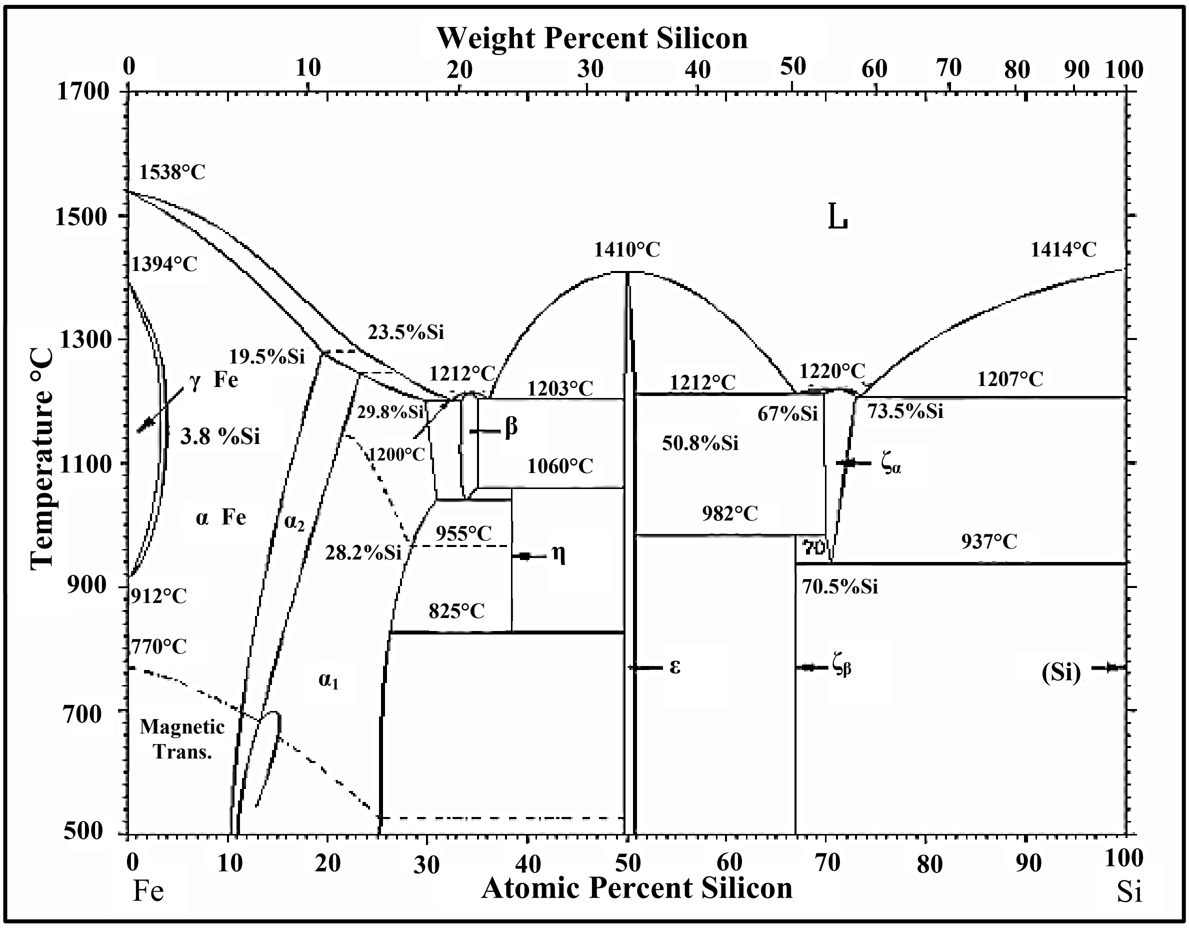

Figure 2.7: Iron-silicon phase diagram [16]

2.6 Magnetic Properties and Microstructural Factors

Power loss and permeability are the most important magnetic properties for electrical steels, although magnetostriction, coercivity, remanence and anisotropy can be very important in some applications. All these properties are structure sensitive and hence they are expected to depend on several metallurgical factors namely chemistry, cleanliness of the steel, grain size, crystallographic texture and stresses; other factors such as saturation magnetization and resistivity are mainly affected by composition and temperature [23-28].

It is not the intention of the author to extensively review these properties (excellent reviews) can be found elsewhere [25] but it is intended to highlight the gradual improvement in the magnetic properties of electrical steels with time shown in Fig. 2.8. Specially emphasize will the place on the role played, then and now, by microstructural control (in terms of chemical composition, grain size distribution and crystallographic texture) in achieving these improvements [16].

A clear improvement in the quality of the magnetic properties in electrical steel resulting in reduced the power losses, coercive force and increasing the permeability has been achieved by microstructural control driven by the microstructure dependent character of the magnetic properties.

It is generally accepted that parameters such as a large grain size, an optimum crystallographic texture (θ fiber (<001>||RD) in the case of NGO-steels and Goss component {110}<100> in the case of GO-steels) and the nature of second phase particle (size + distribution) define the magnetic quality of the steel. All of the component features of the microstructure are the result of the thermo-mechanical manufacturing processing. Depending on the deformation mode, the annealing treatment (temperature, time, and atmosphere) and the starting composition of the material a finished product is produced with a specific microstructure. Therefore, understanding of the mechanisms responsible for the microstructural evolution is key to tailoring steel properties to the specifications required by progressively stringent market demands [16, 29].

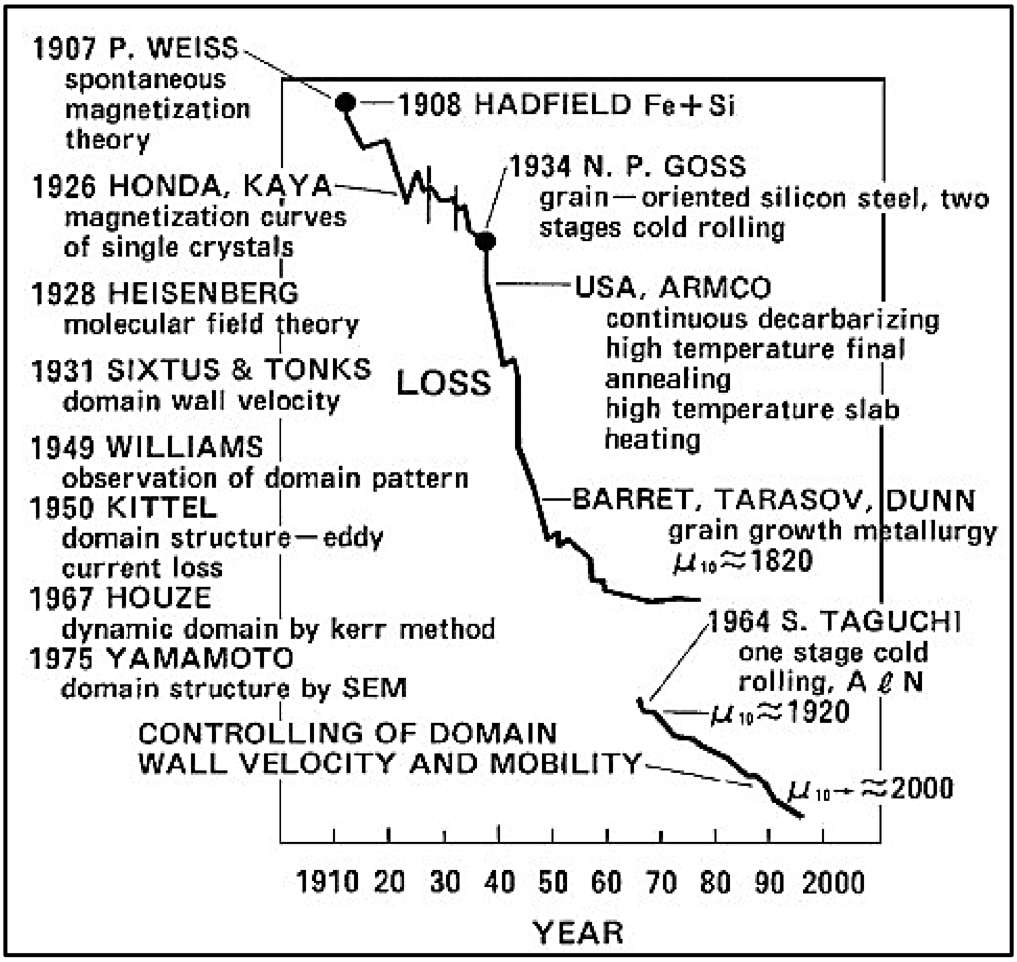

Figure 2.8: Historical development of core loss reduction in electrical steel [29]

2.7 Crystallographic Texture

A large number of polycrystalline materials, both manmade and natural, display preferred orientation of crystallites, called crystallographic texture or texture. It is an intrinsic feature of metals, ceramic, polymers and rocks and has an influence on properties such as strength, electrical conductivity and magnetic properties. The directional characteristics of many polycrystalline materials were first recognized not in metals but in rocks and were described as “Texture”. In the 20th texture was largely investigated by metallurgists and later in polymers, each science and ceramic [30]. The relation of the material properties to this preferred alignment of the crystallites in certain sample direction is one of the key problems in material science for the optimization of properties.

Texture characterization and measurement technology has been systematically performed by the texture analysis pioneer, Prof. H.J. Bunge, in his books or published paper [31][32]. The texture is represented as the orientation distribution of crystallites.

For a description of the orientation distribution two coordinate systems are introduced. The two different coordinate system are the crystal coordinate system K_B which consists of a three of selected crystallographic directions [100], [010], [001] and the sample coordinate system K_A consisting of three sample directions (RD) rolling direction, (TD) transverse direction and (ND) the normal direction to the sheet. The crystal orientation is then defined by the rotation g which transforms the coordinate system K_A into K_B as shown in Fig. 2.9.

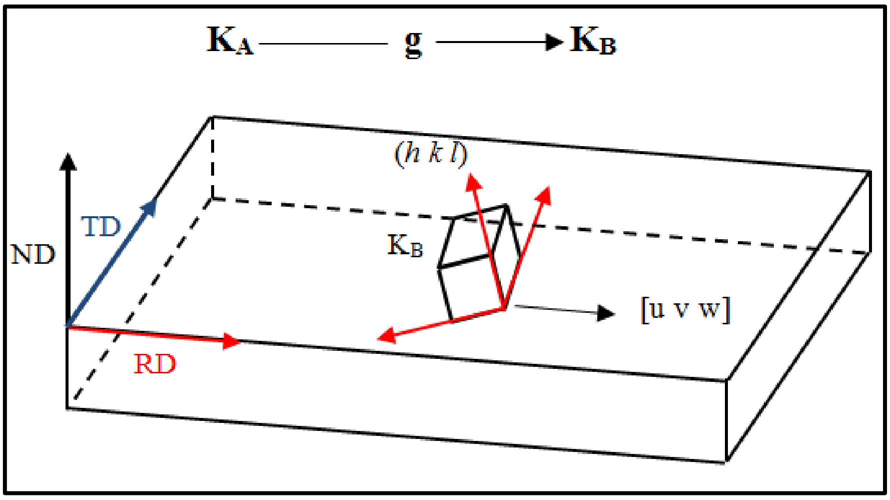

Figure 2.9: The orientation of a crystallite in polycrystalline material is defined by the rotation g which transforms the sample coordinate system K_A in to crystal coordinate system K_B [33]

$K_B = g. K_A$ ……………………………………………………………..………….. (1)

The rotation g can be specified in several ways by for example the transformation matrix g_{ik}, by the rotation axis r and the rotation angle ω, or by the Euler angle (φ_1 ,Φ, φ_2).

$g = [g_{ik}] = \{r_{\theta\psi}, \omega\} = \{\varphi_1, \Phi, \varphi_2\}$ ………………………………………………................ (2)

The texture of polycrystalline materials can then be define by the volume fraction of crystals having the orientation g within the angular limits dg

$$f(\mathrm{g}) = \frac{dV/V}{dg}$$ …………………………………………………………………….. (3)

It is possible to normalized the function *f* (g) in such a way that it is unity in the case of random orientation distribution f_r (g) =1. On the other hand in the case of a non-random distribution, the function *f*(g) is expressed in “Multiple of the random Density abbreviated as “ m.r.d ”. There are various descriptions of the orientation explained in [34, 35].

2.7.1 Pole figure

The pole figure is the method most often utilized to represent texture measurement by X-rays or neutron or synchrotron diffraction of polycrystalline materials. A pole figure is a stereographic projection of polycrystalline aggregate showing the distribution of poles, or plane normal, of a specific crystalline plane using the specimen axes as reference frame. Pole figures are utilized to characterize preferred orientation in polycrystalline materials [36, 38]. A pole figure is usually measured for a fixed set of lattice plane {*hkl*} as a function of the sample direction. Figure 2.10 shows a schematic drawing of the <100> pole from differently oriented crystals on the projection plane. The crystal satisfies the condition for <100> diffraction, when the sample is positioned on the marked points. As seen in Fig. 2.10, the poles are projected from the reference sphere onto a pole figure as follows. The position of a given pole on the sphere is commonly characterised in terms of angles. The angle α describes the azimuth of the pole, where α = 0° is the north pole of the unit sphere. The angle β characterises the rotation of the poles around the polar axis, starting from a specified reference condition [47].

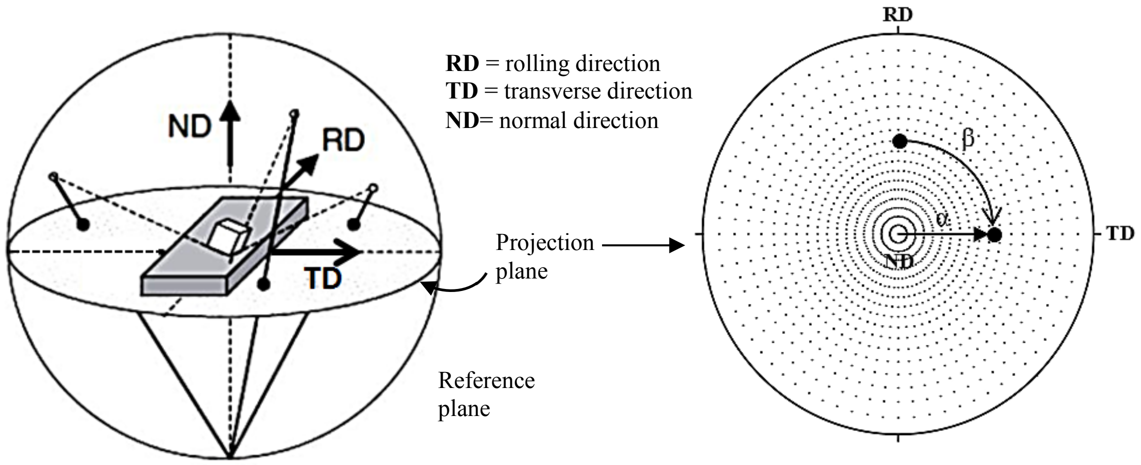

Figure 2.10: Definition of the (100) pole on the projection plane in the case of a single crystal. [50]

On the mathematical side, texture can be described by the orientation distribution function (ODF) f (g) with the orientation g (φ_1, Φ, φ_2). Since the diffracted intensity does not depend on the rotation angle around the scattering vector, two or more pole figures are required for calculation of the ODF, where the required number of pole figures and suitable choices of {*hkl*} depend on crystal symmetry and sample symmetry [39]. For the investigation of three dimensional orientation distributions of the grains within a polycrystalline aggregate the orientation distribution function, the ODF f (g) has to be reproduced from two-dimensional pole figures. For this reason two basic concepts have been evolved, namely, the series expansion methods [35, 39-42] and so called direct inversion methods [44-50].

2.7.2 Orientation Distribution Function (ODF)

The pole figure method has very many advantages. However, it is well known that the pole figures describe only the distribution of a specific crystallographic plane in a sample coordinate system, and thus principal orientations of the texture cannot be precisely determined from them. It has been well established that the orientation distribution in texture materials can be qualitatively as well as quantitatively evaluated using crystallite orientation distribution function analysis (ODF) developed by Bunge and Roe [31][51] using the series expansion method.

The ODF describes the frequency of occurrence of particular orientations in a three dimensional orientation space. This space is defined by three Euler angles according to Bunge (φ_1, Φ, φ_2) which are related to the macroscopic axis of the sample, defined as the rolling direction (RD) axis, transversal direction (TD) axis and normal direction (ND) axis through a set of three consecutive rotations that must be given to each crystallite in order to bring its crystallographic axes into alignment with the specimen axes.

a. The Ideal Orientation (Miller or Miller-Bravais Indices)

The ideal orientation notation is used to represent an orientation (g) as conventionally written in Eq. (4).

g = (hkl)[uvw] ……………………………………………………………………….. (4)

where {hkl} plane is parallel to the rolled sheet plane and <uvw> direction parallel to the rolling direction. If non-specific indices are quoted, the Millar indices family can be used (hkl)[uvw]. For example (001)[100] orientation which is called the cube orientation is illustrated in Fig. 2.11, [001] lies in the plane of the sheet with 0° rotation around normal direction of the sheet with respect to the rolling direction.

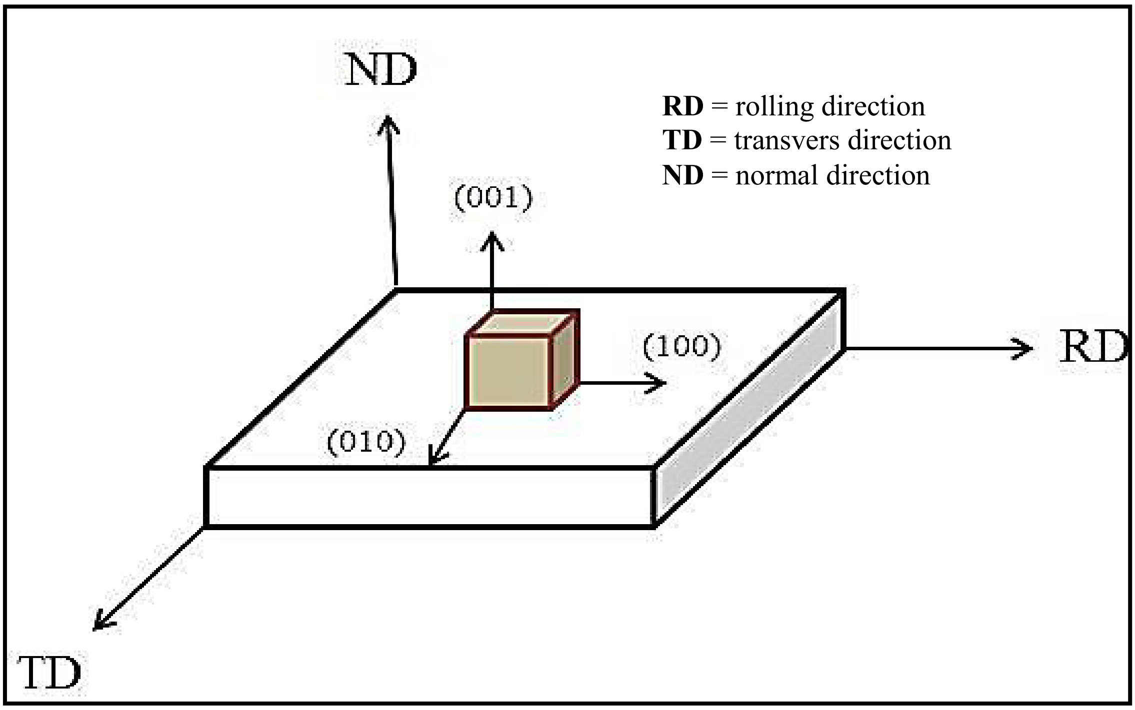

Figure 2.11: Schematic illustration of the relationship between the crystal and sample axes for (001)[100]

b. Euler Angles and Euler Space

Euler angles represent an orientation of the crystal coordinate system in which the axes are parallel to those of the sample coordinates system [34].The Euler angles are three angles transforming the sample system (x, y, z) on the crystal coordinate system (x', y', z') in order to specify the orientation as shown in Fig. 2.12.

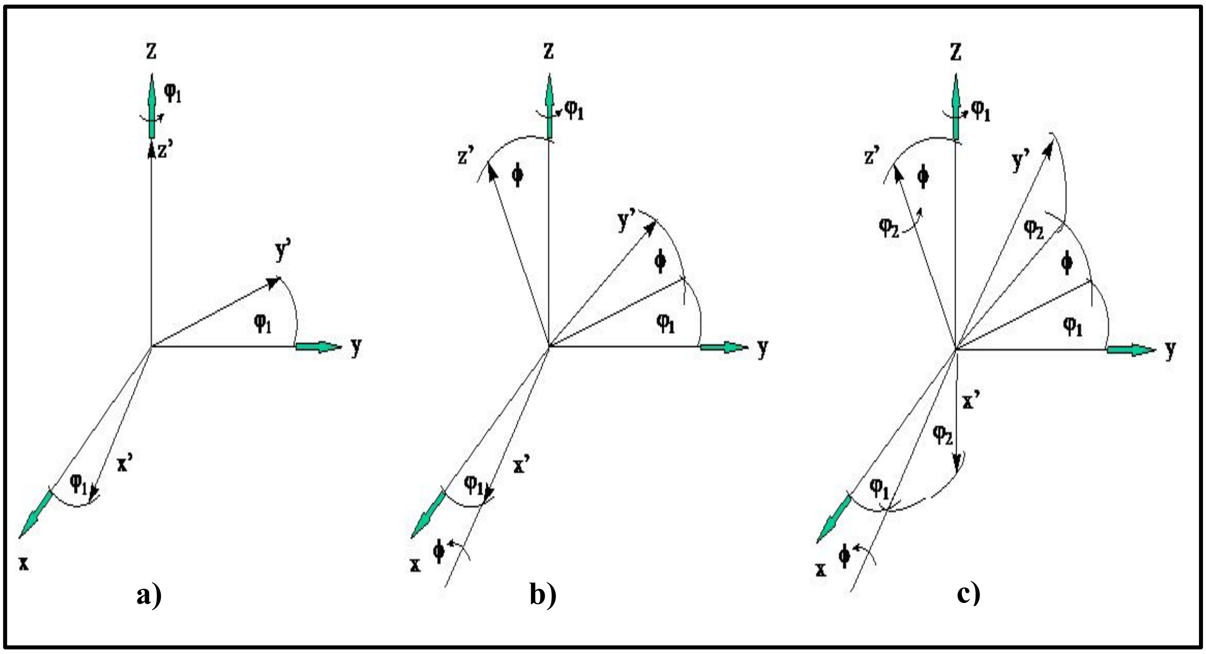

Figure 2.12: The Euler angles (φ_1,Φ, φ_2), samples coordinates system: (x, y, z), crystal coordinate system (x', y', z') [35]

There are several different conventions for the Euler angles. The most commonly used are those formulated by Bunge. The orientations are:

1. Rotation about the z' axis = [001] through the angle φ_1 (Fig. 2.13a)
2. Rotation about the x' axis = [010] through the angle Φ (Fig. 2.13b)
3. Rotation about the new z' (in its new orientation) = [001] through the angle φ_2 (Fig. 2.13c)

The rotation (g) is represented by the three Eulerian angles φ_1, Φ, φ_2

$g = \{ \varphi_1, \Phi, \varphi_2\}$…………………………………………………………………….. (5)

It is usually to represent the three parameters of the rotation (g) namely φ_1, Φ, φ_2 as Cartesian coordinates in a three dimensional space, the so-called orientation space or Euler space. Each point of Euler space then corresponds to a particular rotation and conversely each rotation or crystal orientation leads to a point in three dimensional space [35].

One can represent the ODF in a reduced Euler space, when crystal and sample symmetries are considered. The whole Euler space has angles in range of $0° \leq \varphi_1 \leq 360°$, $0° \leq \Phi \leq 180°$ and $0° \leq \varphi_2 \leq 360°$, without consideration of any symmetry. However, after consideration on the both the crystal symmetry and the specimen frame, results in a number of different, but equivalent, description of given orientation [34]. The ODF needs to be given only in the symmetric unit in Euler space. If the Euler angles (φ_1, Φ, φ_2) are represented as rectangular (Cartesians) coordinates one of specific orientations space can be obtained which is called the Euler space as shown in Fig. 2.13.

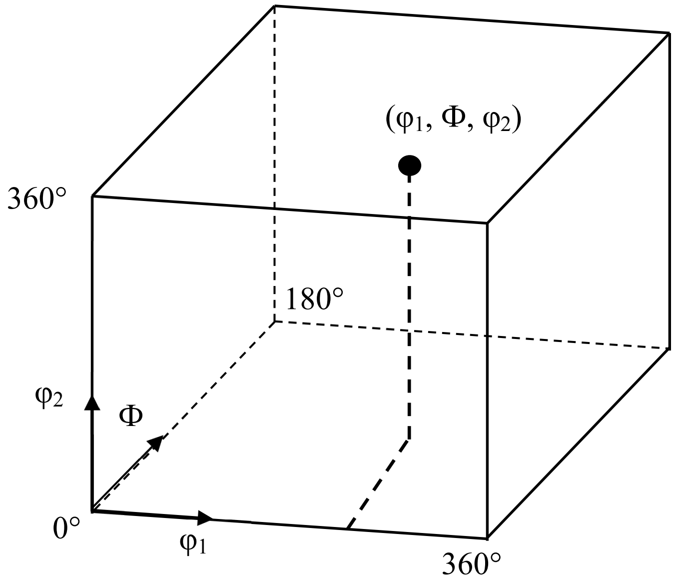

Figure 2.13: Euler space with maximum range of Euler angles (Asymmetric unit or triclinic crystal symmetry)[36]

The ODF is calculated from measured pole density distribution functions (P_{hkl} (α, β), pole figure) via a so-called pole figure inversion. A pole figure represents the probability of the orientation distribution of the crystal placed in an arbitrary specimen direction. The probability is contoured on a sphere, relative to specimen coordinate and projected on a plane, using equal area or stereographic projection.

Pole figures can be directly measured by various diffraction techniques, e.g. laboratory X-ray, neutron and synchrotron diffraction facilities. However, the coverage of such measurements is often incomplete and the measured pole figures have non-normalized intensities. More importantly, the pole figures provide the orientation distribution of crystallites in two dimensions so that some of different crystallite orientations appear on same domain. These are the reasons why ODF is preferred for quantitative representation and analysis.

In the present work the “The Orientation Distribution Function” (ODF) was calculated from such pole figures by ISEM (Iterative Series Expansion Method) [53]. In the present work the series of expansion method by Bunge is utilized. In Bunge’s formalism, a pole figure is expanded in series of spherical harmonic function:

$$P_{hkl}(\alpha,\beta)=\sum_{l=0}^{l\max}\sum_{v=l}^{N(l)}F_l^v(hkl).\dot{K}_l^v(\alpha,\beta)\ldots\ldots\ldots\ldots\ldots\ldots\ldots\ldots(6)$$

$$F_l^v=\int_{\alpha=0}^{\pi/2}\int_{\beta=0}^{2\pi}P_{hkl}(\alpha,\beta).\dot{K}_l^{*\mu}(\alpha,\beta)\sin\alpha d\alpha d\beta\ldots\ldots\ldots\ldots\ldots\ldots\ldots\ldots(7)$$

Where *l* is the degree of series expansion, *F* are the pole figure coefficients, and *k* are the symmetrized spherical harmonic functions. The *F* coefficient can be calculated by the integration of the experimentally achieved pole density distribution, and pole figure inversion, in this case the normalized pole figure intensities are utilized.

The equation above show how the unknown *C* coefficients of orientation distribution function can be calculated from the Known *f* coefficients. Once the *C* coefficients are known, the ODF expanded into a series of generalized spherical harmonics can be achieved.

$$f(g)=f(\varphi_1,\phi,\varphi_2)=\sum_{l=0}^{l\max}\sum_{\mu=l}^{M(l)}\sum_{v=l}^{N(l)}C_l^{\mu v}.\ddot{T}_l^{\mu v}(\varphi_1,\phi,\varphi_2)\ldots\ldots\ldots\ldots\ldots\ldots\ldots\ldots(8)$$

$$F_l^v(hkl)=\frac{4\pi}{2l+1}\sum_{\mu=1}^{M(l)}C_l^{\mu v}.\dot{k}_l^{*\mu}(hkl)\ldots\ldots\ldots\ldots\ldots\ldots\ldots\ldots(9)$$

In eq. (6) to (9) the symbol ′*′ denotes the complex conjugate, and dots over the harmonic function denote the symmetrisation of the functions. M(*l*) and N(*l*) are the number of independent values for each degree of expansion degree, *l*, after the sample and crystal symmetrisations, respectively.

ODF is a three dimensional description of crystallographic texture but a direct measurement of the ODF is not possible since conventional texture goniometry is only able to determine the distribution of crystal poles of diffracting planes normal, i.e., pole figures.

Mathematical models have been developed which allow the ODF to be calculated from the numerical data obtained from several pole figures. Therefore, in order to compute the orientation distribution function for a polycrystalline sample, pole figure measurements are required. The number of pole figures needed for an ODF calculation depends upon the crystal symmetry of the sample that is being measured. For bcc structure materials, as it is the case for silicon steel, three pole figures ((110), (200) and (211)), are needed.

2.8 Texture Measurement

2.8.1 X-ray

X-rays were discovered in 1895 by the German physicist Röntgen and were so named because their nature was unknown at that time. It was found that X-rays could affect photographic films in the same way as light but, unlike ordinary lights, these rays were invisible, but they traveled in straight lines and they were much more penetrating and could easily pass through the human body, wood, pieces of metal and other objects [63]. In 1912 the precise nature of X-ray was demonstrated, and in that year the physical process of X-ray diffraction by crystals was discovered, and this discovery simultaneously proved the wave nature of X-rays and provided a new method for investigating the fine structure of matter [63].

The principle of Bragg's diffraction is shown in Fig. 2.14. Diffraction occurring according to Bragg's law.

$2d_{hkl} \sin\theta = n\lambda$

d_{hkl}= distance between diffraction angle
λ = wavelength of the x-ray
n = is an integer determine by the order given
θ = is the scattering angle

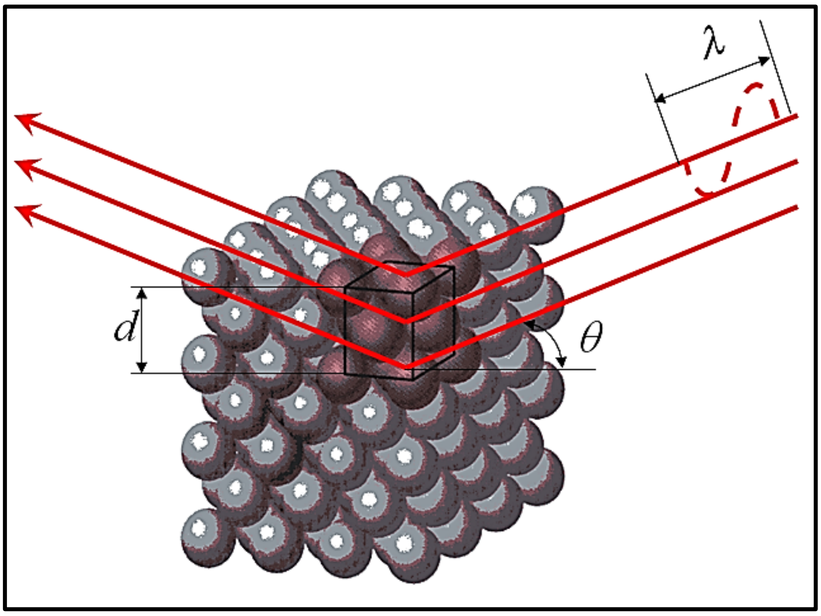

Figure 2.14: The principle of Bragg's diffraction [63]

X-ray diffraction was first employed by Wever [54] to investigate preferred orientations in metals, but only with the introduction of the pole figure goniometer by Schultz did it become a quantitative method [55]. For X-ray diffraction using a monochromatic beam, the wavelength (λ) is constant depending on the target material in the X-ray tube (see table 2.2). Bragg's Law for monochromatic radiation is applied. The principle of X-ray diffraction is simple: the order to determine the orientation of a given lattice plane {*hkl*} of a single crystallite, the detector is first set to the appropriate Bragg angle, 2θ for that particular diffraction peak, then the sample is rotated in a goniometer until the lattice plane {*hkl*} is in the reflection condition (i.e. the normal to the lattice plane or diffraction vector is the bisectrix between incident and diffracted beam), as shown in Fig. 2.15 used a nomenclature for the rotation axes θ, φ, χ and ω is standard symbol in single-crystal diffractometry and marked on most diffractometers [30].

In the case of a polycrystalline material, the intensity recoded at certain sample orientation is proportional to the volume fraction of the crystallites with their lattice planes in reflection geometry [50].

Determination of texture can be done on a sample of large thickness and a flat surface on which X-ray are reflected, or on a thin slab that can be penetrated by X-ray. Because of defocusing effects as the flat sample surface is inclined with respect to the beam, variations in the irradiated volume and absorption intensity corrections are necessary, particularly for the reflection geometry. In the reflection geometry only incomplete pole figures can be measured, usually to an angle of 80° from the samples surface normal [50].

Table 2.2: The type of target materials in X-ray tube [50]

Target material in x-ray tube	Wavelength (Å)
Cr	2.2909
Fe	1.9373
Co	1.7902
Cu	1.5418
Mo	0.7107
Ag	0.5603

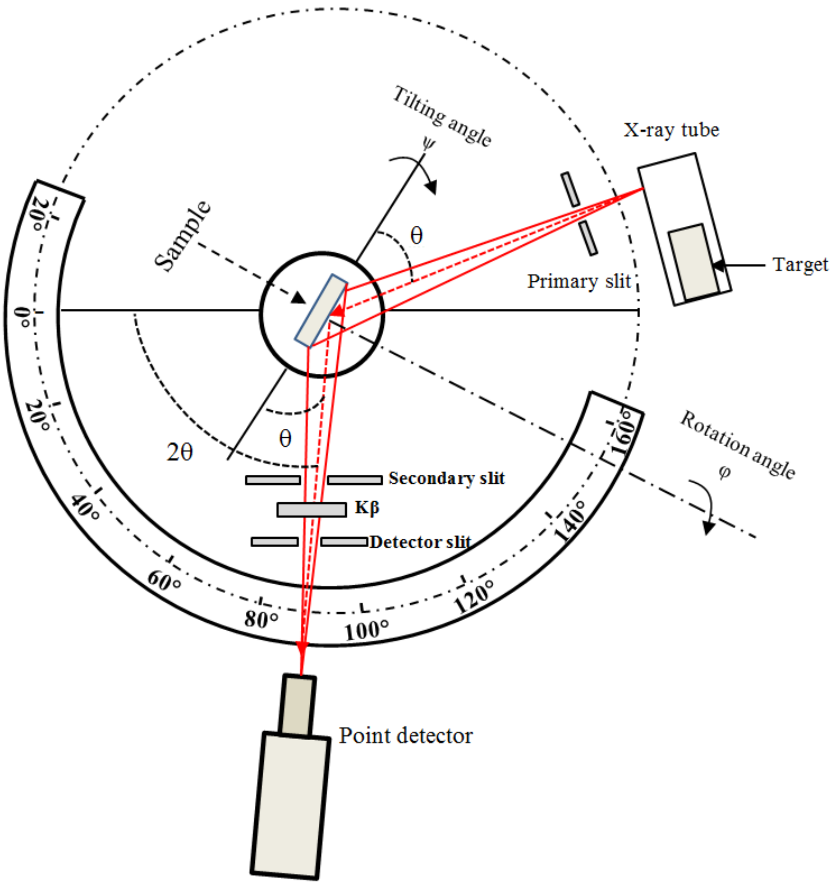

Figure 2.15: Pole figure measurement with a point detector. Bragg's law applies to lattice plane. The sample is rotate about an axis that is perpendicular to the surface

2.8.2 Neutron Diffraction

The first texture measurements by means of neutron diffraction were carried out in 1953 by Brockhouse at Chalk River National Labortatory in an attempt to determine magnetic structure in steel [56]. This technique was further developed by Tobisch [57], and the advantages of neutron diffraction for texture analysis were established by Szpunar [58], Welch [59], Bunge [33], Wenk [60][61] and Brokmeier [62][69][50].

The principles of pole figure analysis by neutron diffraction are equivalent to X-ray pole figure measurements. The neutron detector is set to a corresponding Bragg angle 2θ for the selected lattice planes {*hkl*}. The pole densities for that lattice plane in different sample directions are scanned with a goniometer by rotating the sample around two axes, φ and χ corresponding to the pole figure angles β and α. The main difference between neutron and X-ray diffraction is the much lower absorption of neutrons by matter. Therefore, large samples, usually several centimeters in size, can be in the analyzed in transmission geometry. In X-ray experiments the X-ray beam must not leave the sample surface. Also, for neutron diffraction experiments the whole sample must be in the neutron beam. Then, no intensity corrections are necessary and complete pole figures (up to α = 90°) can be obtained in one scan. The number of grains encountered is much larger using neutrons diffraction, usually, by four to five orders of magnitude, which means that grain statistics is much better. Because of the low absorption, environmental stages can be used for in situ investigations during heating, cooling, and straining of the samples [50].

The wavelength distribution of thermal neutrons is a broad spectrum with a peak at 1-2Ǻ, similar to X-ray. Non-destructive bulk texture analysis on nearly un-prepared materials is one of the greatest advantages of neutron diffraction [50].

Neutrons diffraction texture analysis is done either at rectors with constant flux of thermal neutrons, or with pulsed neutrons at spallation source. Traditional neutron texture equipment at a reactor utilized monochromatic radiation produced with a single crystal monochromator. A goniometer rotates the sample to cover the entire orientation range, analogous to an X-ray goniometer. To improve efficiency position sensitive detectors (PSD) have been used that can record 2θ spectra simultaneously [64-66].

Neutron diffraction is also an efficient tool for measuring multi-phased materials [64]. Due to the high transmission of neutrons through most materials, neutrons diffraction is an efficient tool for the analysis of bulk textures of polycrystalline materials. The main applications are pole figure measurement of coarse grained materials, non- destructive measurements of identical samples in different states, investigations of unprepared natural samples, analysis of rather weak textures and the measurements of multi-phase materials [69][70].

The main feature resulting from the high penetration is measurement of complete pole figure without special sample preparation needs. The measured pole figures can be utilized for ODF calculation after background intensity corrections. A disadvantage of neutron diffraction is that the interaction with material is low, and long counting times are required. The weak interaction can also have greater advantages: it provides high penetration and low absorption, thus making neutrons suitable for bulk texture investigations of large sample volumes [64-66].

Because of their low absorption of texture evolution, neutrons are also sensitive to measure the orientation of magnetic dipoles. Although this was the original incentive of Brockhouse, until today no satisfactory magnetic pole figures have been measured [43][64-66].

Figure 2.16 shows the lay-out of the Neuron instrument at Heinz Maier-Leibnitz Zentrum (MLZ) at (Garching, Germany).

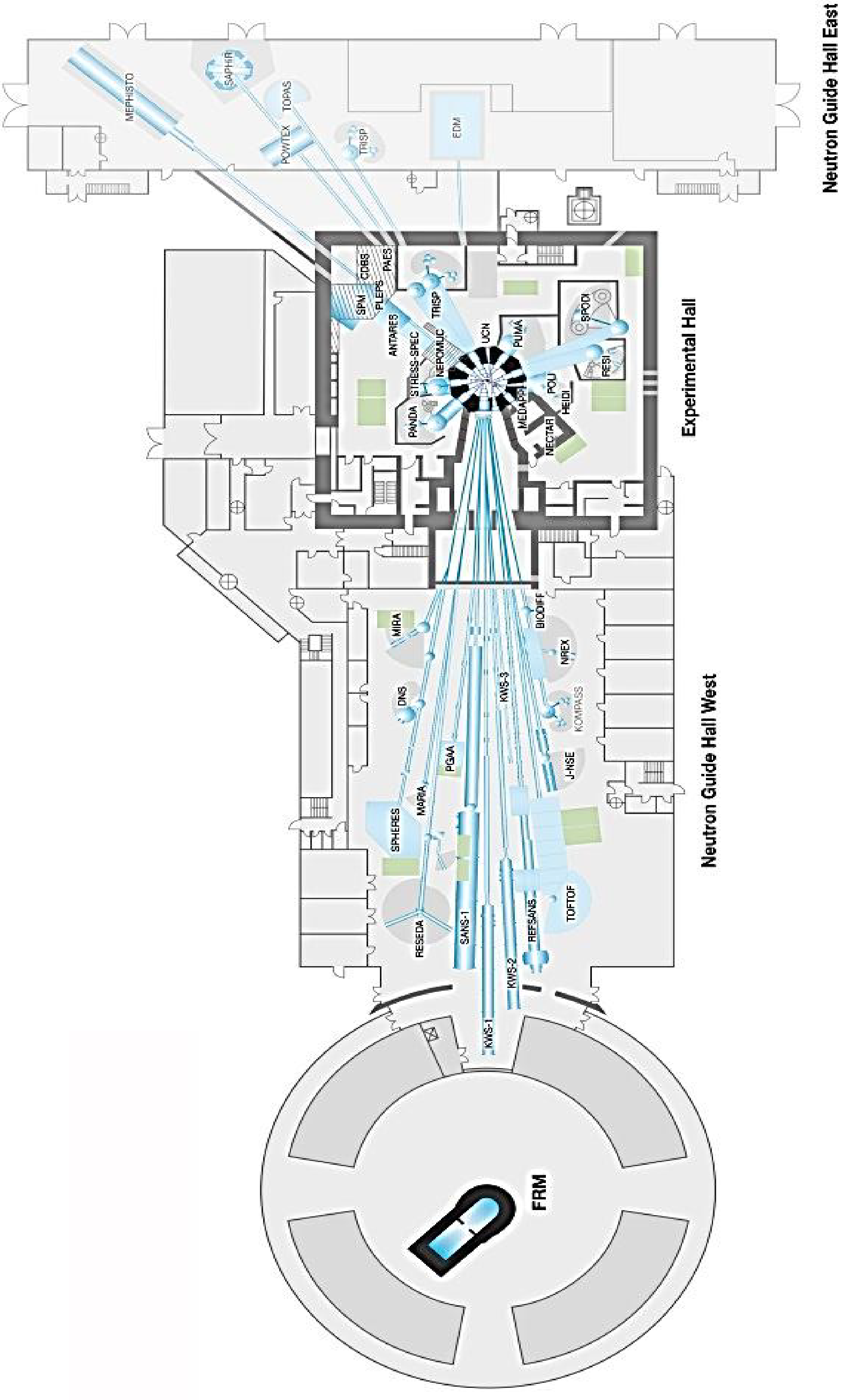

Figure 2.16: Lay- Out of the instrument at MLZ [71]

2.8.3 Synchrotron Diffraction

A synchrotron beam is source of X-ray that can be used for many scientific research and technological investigations. There are many facilities for synchrotron radiation experiments including several international laboratories in the world. In such facilities electro-charged particles, usually electrons or positrons are forced into a circle orbit (in a storage ring with a circumference of more than one kilometer), when the particles move at velocities close to the speed of light, their change in direction induced by the magnetic field, results in a centripetal acceleration force which causes them to emit electromagnetic radiation (X-rays) in a direction tangential to their path. The electrons in such storage rings have energies of about $7 \text{ x}10^9$ eV and the electrons current is about 100mA. This kind of radiation was first found in 1947 from electrons orbiting in a synchro-cyclotron called and was thus called synchrotron radiation (SR) [72][73].

Expression it was broad energy distribution, ranging from the infrared to the hard X-ray regime, synchrotron radiation was considered as a unique source of radiation that can be advantageously used for spectroscopic investigations [74]. By the late 1950, synchrotron radiation itself was being used for experiments, but until the 1970 work was carried out in a parasitic mode with respect to high-energy physics experiments [74]. Although not optimized for the production of synchrotron radiation, the first generation synchrotron rings, such as DORIS at the Hamburger Synchrotronstrahlungslabor (HASYLAB), CESR at the Cornell High Energy Synchrotron Source (CHESS), and SPEAR at the Stanford Synchrotron Radiation Laboratory (SSRL), delivered photon densities (brilliances) around six to seven orders of magnitude higher than conventional laboratory X-ray sources [74], combined with minimum angular divergence of less than 2 mrad (millradin). This unique combination of high photon flux, small beam size, high penetration depth through materials and free choice of wavelength opens a wide range of possibilities for texture analysis [37][50].

For texture analysis in fine grained polycrystalline samples usingthe Debye-Scherrer method and synchrotron radiation, a tight beam of monochromatic X-rays is required. To achieve monochromatic radiation, the beam first passes through a cooled copper plate that absorbs radiation with long wavelengths, and then a monochromator crystal selects the desired wavelength in the range of 0.01-0.1 nm [75]. Finally, the monochromatic beam is collimated to the desired size and then passes penetration through the sample. The diffraction from a powder sample with random texture gives a set of homogeneous intensity concentric Debye-Scherrer rings that are related to reflecting lattice planes {*hkl*} by the Bragg angle. If the sample has a texture, the rings display inhomogeneous intensity around the circumference of the Debye-Scherrer rings that are characteristic of the crystallographic texture in the samples[54].

The sample needs to be rotated by an angle ω as shown in Fig. 2.17 and at each setting a pattern has to be recorded. Geometric expressions for the transformation of the angles φ, θ, and ω into the pole figure coordinates α and β have been given by Bunge [76-79], Poulsen [80] and Heidelbach [81].

Synchrotron diffraction images recorded by (charge coupled device) CCD detectors almost instantaneously display the presence of texture expressed in systematic intensity variations along the Debeye-Scherrer rings. Synchrotron analysis is useful for compounds with weak scattering (e.g. polymers and biomaterials) and for investigating local texture gradient. Other applications are in-situ observation of textures evolution during deformation, heat treatment and other experimental conditions [82].

Figure 2.18 shows the lay-out of the Synchrotron instrument at the High Energy Materials Science HEMS@ (Positron Electron Tandem Ring Accelerator) Petra III at Desy-Hamburg, Germany

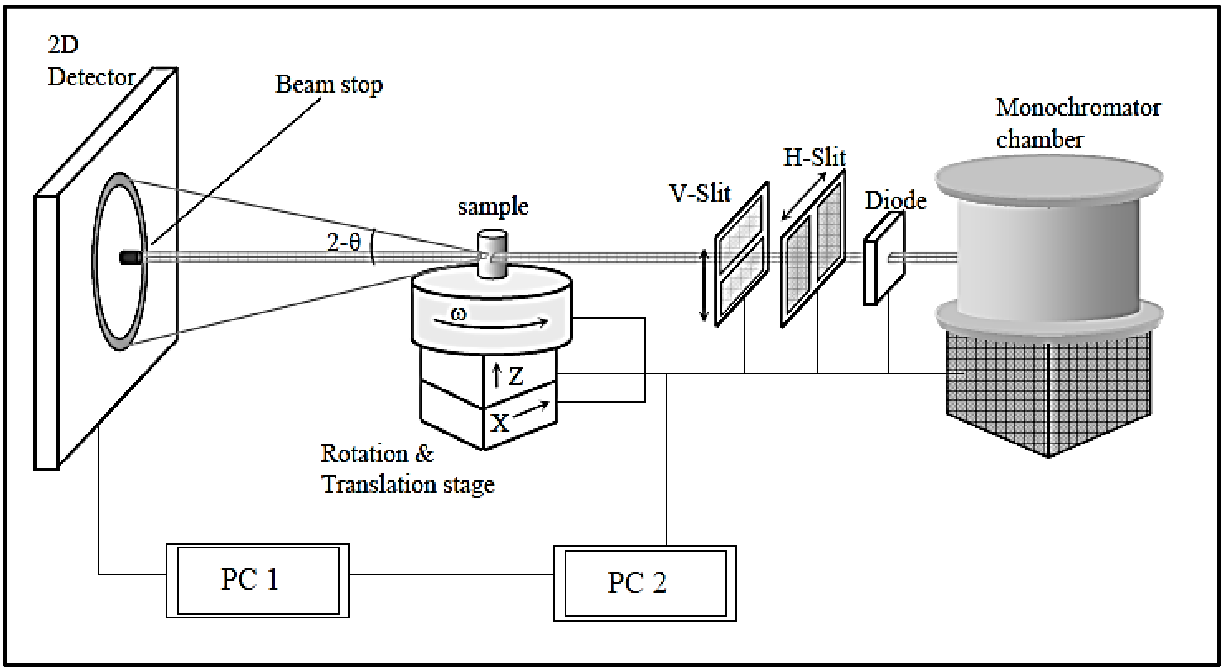

Figure 2.17: Beam line set-up for texture measurement at Petra III in HasyLab. PC 1 is responsible for reading data from the area detector, PC 2 is connected to all motors and controls them. X and Z are perpendicular to the direction of the incident beam [39]

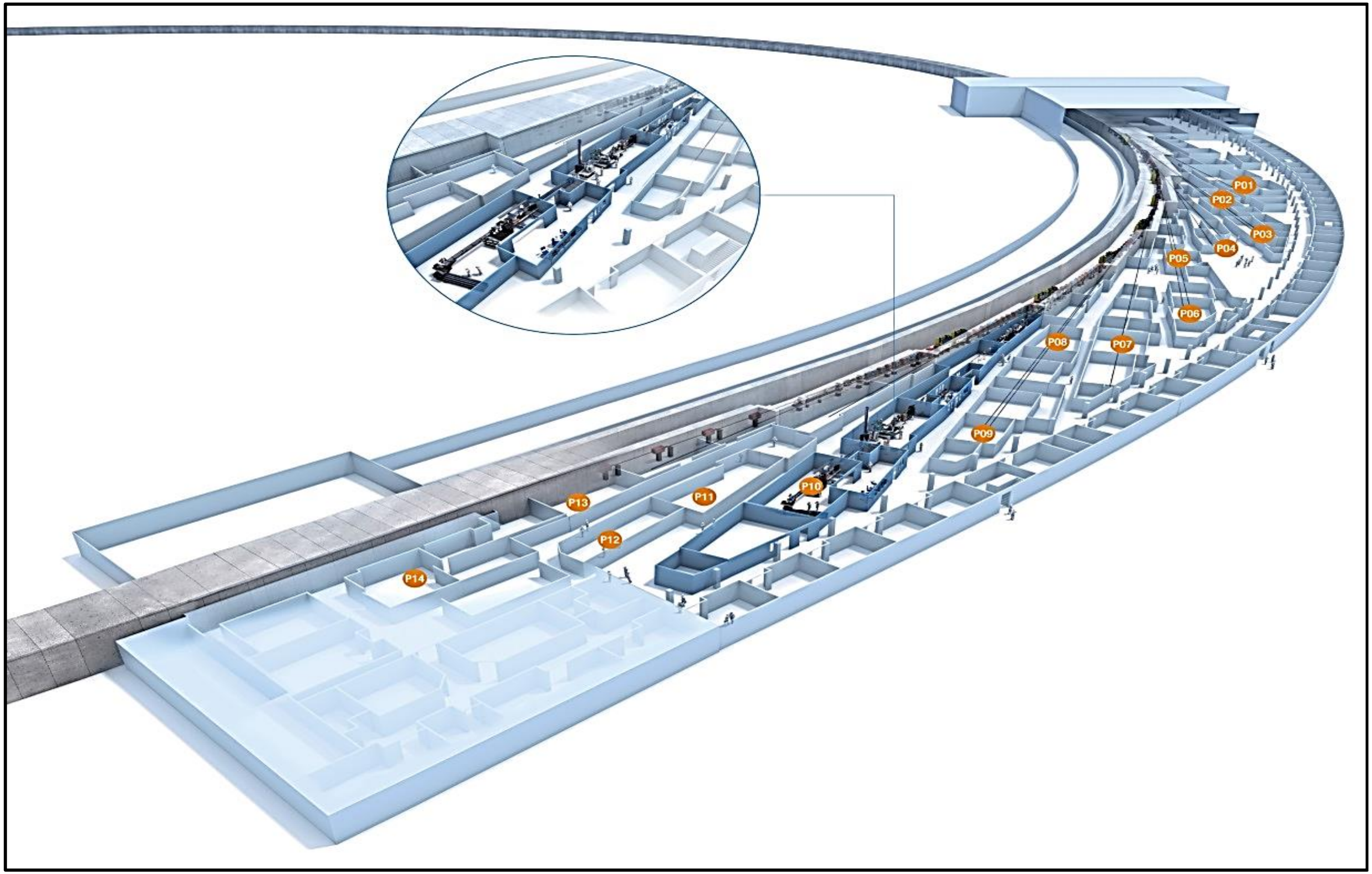

Figure 2.18: Layout of the installations inside the PETRA III experimental hall “Max von Laue” including the ring tunnel, the optics and experiment hutches as well as control cabins [81]

2.9 Crystallographic Texture in Iron Silicon Alloy

The magnetic properties of electric steels are anisotropic and dependent on crystallographic texture [35]. However, it is quite normal for the crystals in such materials to have a random distribution due to the multiple processing steps that the polycrystalline materials are normally submitted to, such as solidification from melting, hot rolling, cold rolling in one step and cold rolling in two steps with an intermediate annealing process. A non-random distribution or preferred orientation of crystals is called texture. Since some of the properties of the crystals are strongly directionally dependent, the crystallographic orientation of the crystallites within the polycrystalline aggregate i.e. the texture plays a very important role [43][83-100].

Texture is represented using the Miller indices in the form: (hkl)[uvw] where (hkl) corresponds to the family of crystallographic planes parallel to the surface of the sample. Thus in the or in case of cubic materials, the (hkl) corresponds to the family of crystallographic directions parallel to the normal direction of the sample (ND) and [uvw] corresponds to the family of crystallographic directions parallel to the rolling direction of the sample (RD). Figure 2.19 shows a schematic representation of the {011}<001> Goss orientation, texture in a sheet.

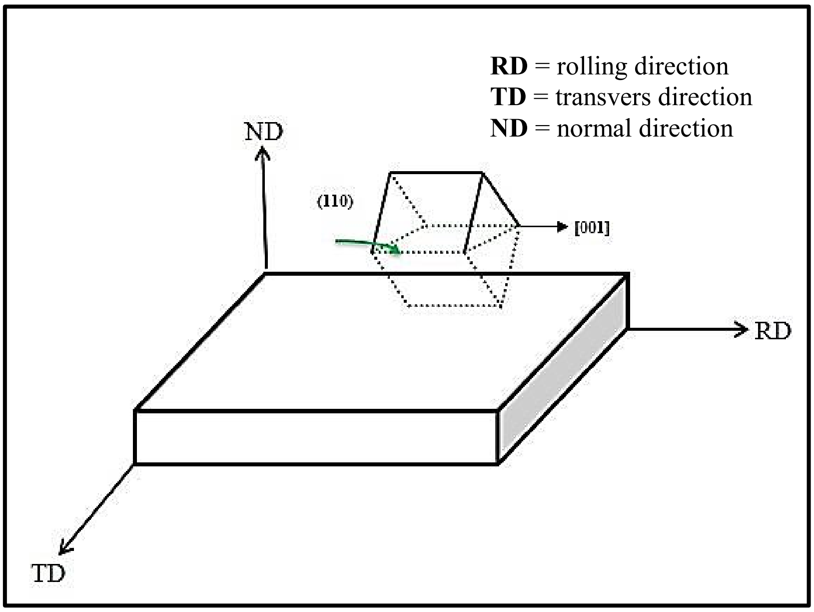

Figure 2.19: Schematic representation of the {011}<001> texture in a sheet [34]

The most common texture components and orientation fibers in steel after rolling and recrystallization are presented in the ODF sections φ_2= 0°and φ_2= 45°, as shown in Fig. 2.20. However, in many cases the important information can be described by a single section φ_2= 45°, because the φ_2= 45° section contains typical fibres textures which are developed during rolling and recrystallization process.

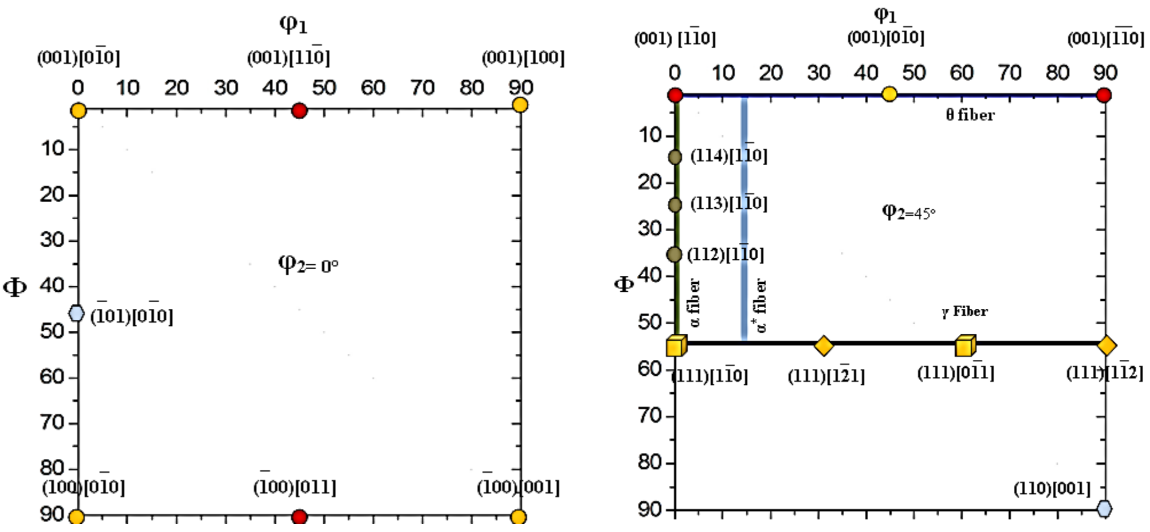

(a) (b)

Figure 2.20: a) $\varphi_{2=}$ 0°, **b)** φ_2= 45° ODF sections in Euler space showing the main texture components in rolled and recrystallized steel.

The rolling and recrystallization textures of bcc materials tend to develop characteristic orientation fibers which consists of: [103-115]

1. The **α** fiber, {hkl}<110>, is characterized by the family of <110> crystal direction being aligned parallel to the rolling direction (RD) of the sheet. The intensity spread from φ_1 = 0°, Φ = 0° to 55° and φ_2 = 45° and describes rotations with <110>||RD. It contains the orientation {001}<110>, {112}<110> and {111}<110> (see Fig. 2.20 (a and b)). The symmetrically equivalent position of this fiber starts at φ_1= 45°, Φ = 90°, φ_2 = 90° and spread through Euler space till φ_1 = 60°, Φ =55°, φ_2 = 45°.

2. The **γ** fiber, {111}<uvw> is characterized by the family of {111} crystal planes lying parallel to the plane of the sheet, or in other words, by the family of the normal directions to the {111}crystal planes being parallel to the normal direction (ND) of the sheet. The intensity spread ranges from the section along φ_1 from 0° to 90°, Φ = 55° and φ_2 =45° and describes all rotations with <111>||ND (see Fig. 2.20 (a and b)). It contains the orientations {111} <110> at φ_1 = 0° and {111}<112> at φ_1=30°. Because of the three-fold symmetry of the <111> axis the parts φ_1=0° to 30°, 60° to 30° and 60° to 90° are symmetrically equivalent.

3. The **η** fiber is characterized by the family of <100> crystal directions being aligned parallel to the rolling direction (RD) of the sheet. The intensity spread ranges from φ_1, φ_2= 0° along Φ= 90° and describes all rotations around <100>||RD. It contains two important texture component, namely the Cube component {001}<100> and the Goss component {011}<100> which influence the magnetic properties for iron silicon materials.

4. In certain cases the **ζ** and **ε** fiber textures with the <011> crystal directions being parallel to ND and TD, respectively, are of interest.

The rolling texture of iron and low carbon steel is largely independent of composition and processing variables and even such major microstructural inhomogeneities such as shear bands have been little influence. Table 2.3 gives the Miller indices and Euler angles of the important bcc rolling texture components [83].

Table 2.3: Texture components in rolled bcc metals [83].

{hkl}	**<uvw>**	**φ_1**	**Φ**	**φ_2**
001	110	45	0	0
211	011	51	66	63
111	011	60	55	45
111	112	90	55	45
11, 11, 8	4, 4, 11	90	63	45
110	110	0	90	45

The typical crystallographic textures of cold rolling bcc structure show two common features: Firstly, the formation of a strong intensity spread along the α fiber <110>||RD between {001}<110> and {111}<110>. And, secondly, an increase of the intensity spread along the γ <111>||ND fiber. The most characteristic features in the development of recrystallization textures in bcc materials is a decrease of the intensity spread along the α fiber <110>||RD and a strengthening of the intensity spread along the γ fiber <111>||ND, particularly an increase of the (111)[112] texture component. The η fiber <100>||RD developed during recrystallization, is an important indicator for predicting the magnetic quality of silicon steel in terms of texture development. The η fiber <100>||RD contains two very important crystallographic orientations for electrical steels, the cube (100)[001] and the Goss {110}<001> orientations. There are many factors are influenced on recrystallization texture such as grain size, impurities, composition, defect density, and processing parameters at each of the several production stages.

Improvement of texture in non-oriented electrical steels during thermo-mechanical processing can be attained by reducing the intensity of undesirable components such as (α fiber (<110>||RD), γ fiber (<111>||ND), α* fiber {h h l} <h/l + 1 h/l + 2 h/l> and increasing the fraction of spread along the η fiber (<100>||RD) and θ fiber (<100>||ND). These fibers are related to the macroscopic axes of the sample, define as the rolling direction (RD), transverse direction (TD) and normal direction (ND) [52][136][158].

As for silicon steel, it is well know that texture plays a very important role due to the pronounced magnetocrystalline anisotropy exhibited by such ferromagnetic materials. In silicon steel, the <100> direction is the easy axis of magnetization, the <111> direction is the hardest axis of magnetization and the <110> direction is an intermediate magnetization axis [2][90-115]. Figure 2.21 shows the magnetization curves along these three directions in a single crystal. Due to its large application in electrical motors, where the magnetic field is in the plane of the sheet, the ideal texture for NGO silicon steel would be the (100)[0vw], i.e., all crystals with their {100} planes parallel to the sheet's surface and all possible rotational positions about this normal. The sheet would then be isotropic in its own plane [16]. The Goss texture, {110}<001>, is also a very attractive texture, since it has the {110} planes parallel to the plane of the sheet and the <001> directions parallel to the RD. In contrast, the gamma fiber, represented by (111)[uvw], is a very detrimental texture for silicon steel. This is because the lowest permeability axis, the <111> direction, is then parallel to the normal direction of the sheet. This fiber should therefore be avoided [116-120].

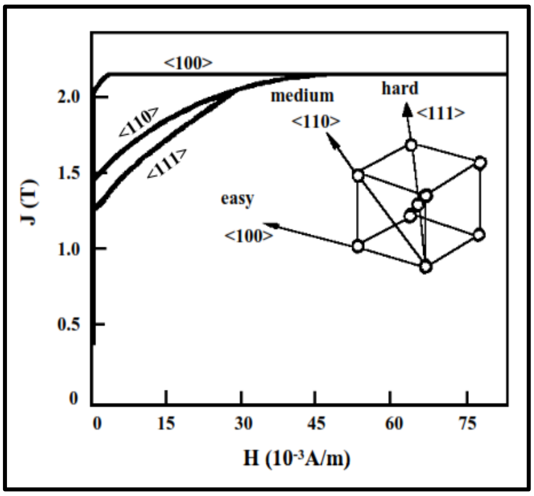

Figure 2.21: Magnetization curve for iron [2]

There are several ways to determine the crystallographic texture for polycrystalline materials by using X-ray diffraction, Neutrons diffraction and electron diffraction by using Transmission Electron Microscopy (TEM) or Scanning Electron Microscopy (SEM). X-ray diffraction is the most commonly applied technique for measured crystallographic texture. Due to coarseness of the grains after annealing treatments, a diffraction method with high penetration and large beam cross section is required. Texture analysis by neutron diffraction fulfills these criteria and has become a method to investigate the bulk texture of different types of material with high precision [69][70].

2.10 Magnetic Materials and Loop Hysteresis Loops

In the beginning the enchantment with electricity and magnetism was started in ancient Greece, however it was not until the nineteenth century when the first experiments of electricity produced in the progress of theory that develop the future of electrical applications. In 1800 by Alessandro Volta, who produce an electric current firstly, in 1820 Hans Christian Oserted he discovered changeable magnetic fields produced electric currents to discoveries by Michael Faraday in 1831, which connected magnetism and electricity in the experiments. Although the list of names of theoretical contributes to electrical engineering is long, the least three names emerge with the first being James Clerk Maxwell, who combined electric and magnetic phenomena to modern electromagnetic wave as described in search on electricity and magnetism in 1873 [1][2][16][121-125]. The second was Olivier Heaviside who greatly advanced the practical understanding of electrical engineering concepts and finally Charles Proteus Steinmetz, who introduce alternating circuit analysis techniques that are now taken for granted in early years of electrical engineering education [1][2][16][121-125].

Magnetism and electricity are closely linked to each other. Electric fields associated only with the existence of an electric charge, and this is the fundamental priority of the material. Electric charges are consisting of electrons (elementary negative electric charge), protons (elementary positive electric charge) and ions flowing in a field. Properties of electric field depend on the distribution of positive and negative charges. An electric field (E), expressed in voltage per meter Vm^{-1}, can exert physically force on the electric charge. It can also produce magnetic fields in the vicinity of the magnetic bodies, but in the end all magnetism results from the physical movement of electric charge that forms electric current. Magnetic charges do not exit, but are often used visualizing magnetic field phenomena using a concept of magnetic dipole [1][2][16][121-125]. Electric and magnetic field are represented as vectors. The vectors are described by both magnitude and direction. A magnetic field can be characterized by using magnetic field density or magnetic induction (*B*), expressed in Tesla (T) or by magnetic field strength *H*, expressed in ampere per meter (Am^{-1}) [1][2][16][121-125].

The magnetic field strength, *H*, in a free space (vacuum) produces magnetic flux density B, where B is defined by the following equation:

$$B = \mu_o H \quad (10)$$

The constant μ_o is called the permeability of free space where $\mu_o = 4\pi \times 10^{-7}$ Tm/A. If the space in which *H* is acting contains any material substance in addition to the free space component of Eq. (10), there will also a component due to the substance itself called the magnetization.

$$B = \mu_o(H+M) \quad (11)$$

The magnitude of M is proportional to the applied field a follow:

$$M = \chi\ H \quad (12)$$

After introducing a parameter that links the magnetization and the magnetic field strength, the material's magnetic susceptibility χ, an equation is obtained:

$$\chi = \mu_r - 1 \quad (13)$$

$$B = \mu_o\ \mu_r\ H \quad (14)$$

Where μ_r is the relative permeability of the material, i.e. the permeability of a material is related to the permeability of free space and μ is the absolute permeability of a material in Tm/A. The relative permeability can be less than unity for diamagnetic materials and much greater than unity for ferromagnetic materials.

When pieces of unmagnetized iron is subjected to the magnetic field of an electric current, the magnetization induced in the pieces of iron by the field is characterized by a magnetization curve obtained by drawing the flux density (*B*) varies as a function of magnetic field strength (*H*) as shown in Fig. 2.22. The curve begins at the origin, and as magnetic field strength (*H*) is increased, the flux density (*B*) field begins to increase slowly, then more rapidly, finally falls off and becoming independent of *H*. The maximum value of the flux density (*B*) reach the saturation point called the saturation flux density and represented in symbol (B_s).

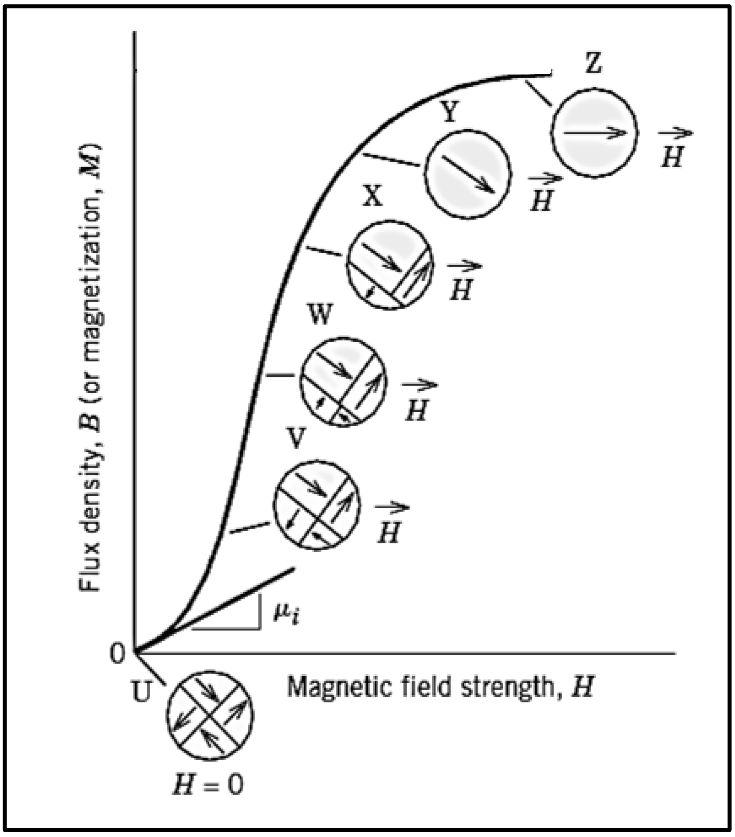

Figure 2.22: The *B*-versus-*H* behavior for a ferromagnetic that was initially unmagnetized. Domain configurations during several stages of magnetization are represented. Saturation flux density B_s, magnetization M_s, and initial permeability μ_i are also indicated [126]

When the magnetic field strength (*H*) is first increased from zero to a high value then decreased again, it is observed that the original curve is not return in the same starting point, and then make a closed curve against the magnetic flux density (*B*). This physical process was named hysteresis and the characteristic curve is called a hysteresis loop as shown in Fig. 2.23. When the magnetic field strength become zero (see figure 2.23), there exists a residual flux density (*B*) that is called the remanence or remnant flux density, B_r, the material remains magnetized in the absence of an external field (*H*). Also, when reduce the flux density (*B*) to zero (see figure 2.23), magnetic field strength (*H*) of magnitude ($-H_c$) must be applied in direction apposite to that of the original field; (H_c) is called coercivity or coercive force.

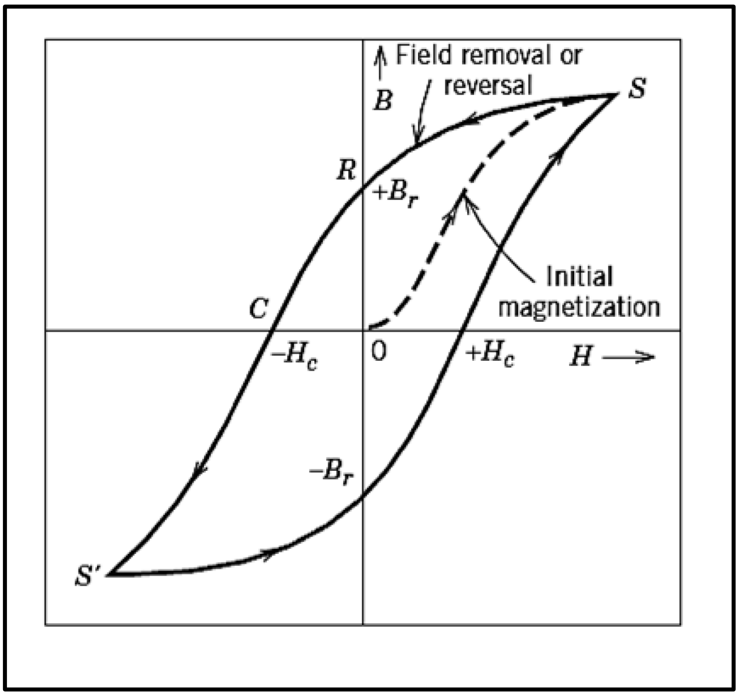

Figure 2.23: Magnetic flux density versus the magnetic field strength for a ferromagnetic material. The hysteresis loop is represented by the solid curve; the dashed curve indicates the initial magnetization. The remanence B_r and the coercive force H_c are also shown [126].

The power losses are just given by the area of the hysteresis curves. Thus, it is only a simple numerical integration of polarization and field strength curves. Due to the definition of power losses as the area of the hysteresis curves, it contains all kinds of losses, which appear in the specimen. Normally total power losses P_T can be subdivided into:

1. Static loss or hysteresis losses P_h is determined from the area of the static or direct current hysteresis loops as usually determined using flux meter and it is not dependent on magnetizing frequency.
2. Dynamic loss or eddy current losses P_{ec} is dependent on magnetizing frequency, Also, the dynamic losses are subdivided into:
   2.1. Classical losses P_{cl},
   2.2. Anomalous losses P_{an}.

The classical eddy current power loss P_{ec} per unit volume of sheet can be calculated by integration $I^2\rho$, where I is the current density over the volume of the sheet and the length of a cycle. The result is

$$P_{ec} = \frac{10^{-9}\pi d^2 B_0^2 f^2}{6\rho} \quad \text{……………………………………………………} (15)$$

where d is the thickness of the sheet in cm, B_0 is the flux amplitude at the surface in gauss, the frequency f in Hz, the resistivity ρ in ohms-cm and P_{ec} in W/kg[16][2].

There is also a substantial variance between the measured eddy current loss and the value calculated classical. The difference between them is called anomalous loss and it will be more than the calculated of eddy current loss. The anomalous loss appears because of the classical calculation of eddy current loss is neglected appearance of domains and domain wall motion. When the domain structure of the material is taken into account for the eddy current loss, and when the calculation of eddy-current loss exceeds the classical loss and the difference between them is larger, the larger is means the domain size and domain structure are affected. It is very complex that the specifics of the domain structure and the domain wall motion are not known in an actual specimen, so that calculations can only be made for assumed and simplified models [16][2].

2.11 Magnetic Annealing

The expression magnetic annealing is utilized regularly to indicate the application of a magnetic field while a material is being heat treated. In 1913, Pender and Jones observed a prominent improvement in magnetic permeability of a Fe-4%Si as a result of the application of an alternating magnetic field during cooling of the alloy from 800°C to room temperature [1]. The primary benefit of magnetic annealing, however, was not been fully recognized until Kelsall, in 1934, reported in detail the significant changes in magnetization behavior of Permalloys (55-80% Ni-Fe) caused by magnetic annealing. Finally, many researchers succeeded in applying magnetic field during annealing of different alloys such as Co-Ni, Fe-Co, Fe-Al, Fe-Si and Fe-Ni. Magnetic annealing has shown to have a significant effect on crystallographic texture and microstructure development in ferric alloys [1][127-130] as well as in non-ferric alloys [131][132].

The effect of magnetic annealing on the crystallographic texture, microstructure and magnetic properties such as permeability, power loss and coercive force remains an interesting study in science and industry, obtaining a full understanding of the mechanisms during the process is remains a challenge [128, 130, 133-135].

As far as the effect of magnetic field on crystallographic texture and microstructure evolution are concerned, iron-based alloys are not the only types of materials that are interesting to the scientific community. Magnetic field effects on non-ferromagnetic materials such as bismuth, zinc, copper-zirconium and some super-conductive materials have also been investigated [132-135]. On the theoretical side, Mullins [131], was the first to consider the origin of the driving force p for domain boundary motion in a magnetically anisotropic material. The aim of his work was to utilize a magnetic field as an artificial method of exerting a known force on grain boundaries. Identification of the factors responsible for the boundaries motion resulting from this artificial driving force would allow the determination of grain boundary properties. Figure 2.24 shows two crystallites of artificially shape and various magnetic free energies. Consider two crystal in such a material that is anisotropic in magnetic susceptibility, where the magnetic contribution to the free energy per unit volume (f /v) induced by a constant external field H for crystallite 1 is lower than that for crystallite 2 ($f_1 > f_2$).

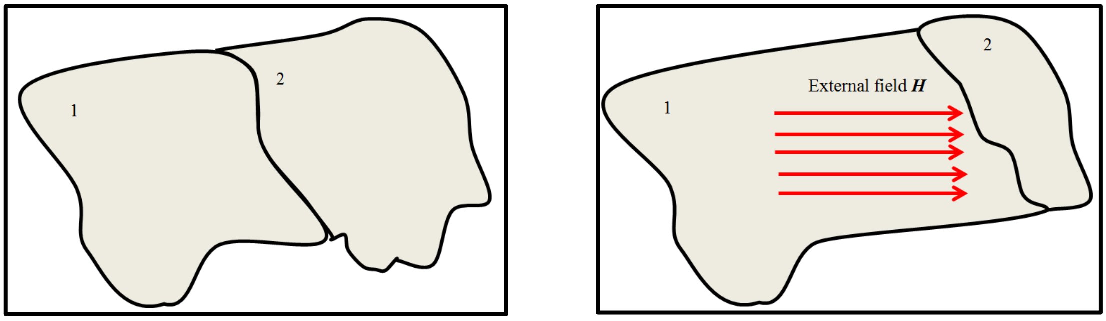

(a) **(b)**

Figure 2.24 Two crystallites within a shape and various magnetic free energies f before (a) and after (b) application of a magnetic external field H where the grain boundary is forced into crystal 2. ($f_1 > f_2$) [131].

If f_1 and f_2 are independent of the boundary shape and size (the condition for this is that $\chi \ll 1$) the reversible change of free energy resulting from the boundary displacement df/dv gives the true pressure acting at any point normal to the boundary:

$$df = \mathrm{p}\, dv$$

$$pdv = (f_2 - f_1) = 1/2\ \mathrm{H}^2 (\chi_1 - \chi_2) \quad \text{(16)}$$

where χ_1 and χ_1 are the susceptibilities of crystallites 1 and 2, respectively, along the magnetic field ***H***. Thus we can see that when $\chi \ll 1$, the boundary pressure p will depend only on the strength of the extenal field and its orientation with respect to the two crystals. The dependence of p on the field through $\boldsymbol{H}^2$ gives strong effect especially for high fields [131].

2.12 The Dislocation Density Evaluated by Hard X-ray Diffraction

X-ray diffraction peak profile analysis is a powerful tool for the characterization of crystalline materials. Diffraction peaks broaden when crystallites are smaller than 500 nm or the material contains lattice defects [145]. The two effects can be separated on the basics of the different diffraction order dependence of peak broadening. Two classical methods have evolved during the past five decades [145]: the Williamson-Hall [141] and the Warren-Averbach [142, 143] methods. The first is based on the full width at half-maximum (FWHM) values and the integral breadths, while the second is based on the Fourier coefficients of the profiles. Williamson and Hall suggested that the FWHM of the line profile can be written as [141]:
$\Delta K = 0.9/D + \Delta K^{D}$..(17)

where ΔK^{D} is the strain contribution to line broadening and D is the volume average grain size or particle size. $K = 2\sin\theta/\lambda$, $\Delta K = 2\cos\theta\ (\Delta\theta)/\lambda$, θ and λ are the diffraction angle and X-ray wavelength of respectively, and $g = K$ at exact Bragg position. When strain is caused by dislocation ΔK^{D} has the following form [145]:
$\Delta K^{D} = A\ (\rho^{*})^{1/2} + A'\ (Q^{*})^{1/2}$ ....(18)

where A and A' are parameters determined by the effective, R_e, and the auxiliary parameters R_1 and R_2, respectively, $\rho^{*} = \rho\ (\pi g^2 b^2 C)/2$ and $Q^{*} = Q(\pi g^2 b^2 C)/4$, eq. (18) will be:
$\Delta K = 0.9/D + (\pi A^2 b^2/2)^{1/2}\ \rho^{1/2}(KC^{1/2}) + (\pi\ A'b^2/2)\ Q^{1/2}(K^2 C)$... (19)

Equation (19) shows that if dislocations are the primary source of strain in a crystal, the proper scaling factor of the (FWHM) of the line profile is $(KC^{1/2})$ instead of merely K [145], Eq. (19) has been called the modified Williamson-Hall plot.where $A = \ln R_e$ and $A' = \ln(R_1)\ln(R_2)$ are parameters determined by the effective, R_e, and the auxiliary parameters R_1 and R_2, respectively, $\rho^{*} = \rho\ (\pi g^2 b^2 C)/2$ and $Q^{*} = Q(\pi g^2 b^2 C)/4$.
According to eq. (20) below that the {*hkl*} and *L* dependence of (ε_g, L^2) can be separated into the contrast factors of dislocation, C, and the strain function $f(\eta)$. The contrast factors of dislocations depend on the relative orientations of the diffraction vector, the line and Burger vectors of the dislocations and the elastic constant of the crystal, in a similar way as in transmission electron microscopy. The value of C can be obtained by numerical methods that take into account the elastic constants of the material [144, 145, 172].
$\langle \varepsilon_g, L^2 \rangle = -(b/2\pi)^2\ \pi\ \rho\ C\, f(\eta)$ ……………………………………..................................(20)
$C = A- ((B\ (h^2k^2 + h^2k^2 + h^2k^2)/\ (h^2 + k^2 + l^2))$ ………………....…………………………......(21)
where A and B are constants depending on the elastic constant of the crystal.

3. Material and Methods

3.1 Introduction

This chapter introduces the material processing hot rolling, cold rolling and cold rolling with intermediate annealing processes, heat treatments, magnetic annealing and magnetic properties. Furthermore, the methods have been used for evaluating crystallographic texture, magnetic properties, dislocation density, hardness measurement and the microstructure.

3.2 Material

3.2.1 Hot Rolling

As starting material an iron silicon alloy with 2.6wt% silicon was obtained from the company VACUUMSCHMELZE, Hanau, Germany. The first hot rolled step at 1100°C was done at the VACUUMSCHMELZE with a thickness reduction from about 330-380mm to a thickness of 10mm which corresponds to a reduction of approximately 97%.

The chemical composition of the material was determined by electric discharge spectroscopy (Spectro Analytical Instrument, GmbH) after hot rolling and it is shown in table. 3.1.

Table 3.1 Chemical composition of the used ironsilicon samples

Material	%Si	%C	%Mn	%S	%N	%Al
Fe-Si	2.6	0.0079	0.1135	0.0033	0.0065	0.001

3.2.3 Cold Rolling at One Stage

Samples of 25mm x 55mm x 10mm were cut from the hot rolled band and then cold rolled on a laboratory mill (BÜHLER, Germany) to a final thickness of 1mm. The rolling direction of the cold rolling process was perpendicular to the previous hot rolling direction (CRD ⊥ HRD). Reduction steps in the cold rolling processes were 0.1mm/step. Total reduction related to starting thickness of 10mm is 90% corresponding to a logarithmic true strain of ϕ =2.3, respectively. After 90% cold rolling the samples were annealed for (20 and 60) minutes at different temperatures of 600°C, 700°C, 900°C and 1100°C and cooled down to room temperature.

3.2.3 Cold Rolling with an Intermediate Annealing processes

Samples were cut from hot rolled band and then cold rolled on a laboratory mill (BÜHLER, Germany). Samples were entirely cold rolled along a direction perpendicular to the previous hot rolling direction (CRD ⊥ HRD). The initial thickness of the sample was 10mm and final thickness after two stages cold rolling was 1mm and reduction steps were 0.1mm/step.

The cold rolling process at two stages 75% and 60% reduction with intermediate annealing process. After 75% cold rolling the sample was inserted in a furnace at 200°C normal furnace. The temperature was increased continuously up to 600°C with heating rate 6°C /min, hold for 1h at 600°C and finally cooling down to 200°C about 6h. After the heat treatment process, the second stage was after 60% cold rolling then the sample inserted in a furnace at 200°, the temperature was increased continuously up to 800°C with heating rate 4°C /min., hold for 1h at 800°C and finally cooling down to 200°C about 8h as shown in Fig. 3.1.

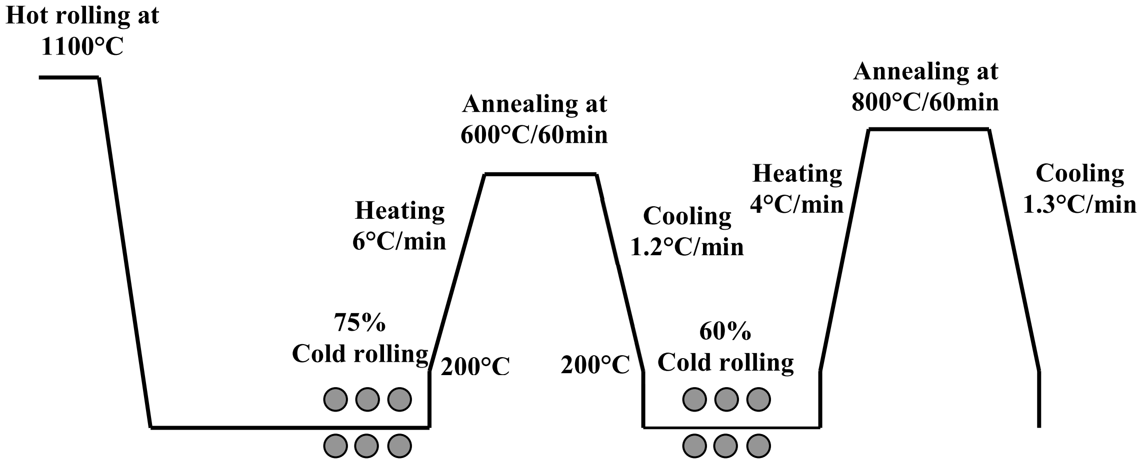

Figure 3.1: the schematically presentation of the processing parameters two stages cold rolling process

3.3 Magnetic Annealing Measurement

The magnetic annealing was carried out at a Dresden High Magnetic Field Laboratory (HZDR), a cylindrical furnace that was inserted into a superconductive magnet which is capable of producing a maximum field of μ_0 = 14 Tesla, bore diameter (B) 6.33mm, coil thickness (T) 1.78 mm, coil spacing (S) 7.11 mm, coil inner diameter (ID) 7.73mm, coil outer diameter (OD) 13.7 mm and height above puck surface (H) 40.1 mm as shown in Fig. 3.2. This furnace is part of a commercial vibration-sample magnetometer (Quantum design Inc., San Diego, USA). A copper sample holder, containing the samples, was inserted into the furnace and placed at the center of the magnetic field with the Fe-Si samples oriented with their rolling direction (RD) parallel to the direction of the field (H) (see Fig. 3.2c)

The furnace was turned on and its temperature was raised to the annealing temperature at 600°C with heating and cooling rate in vacuum as shown in Fig. 3.3 followed by raising the magnetic field. The magnetic field strength was kept constant during the whole annealing process. After cooling the sample inside the furnace to the room temperature then the magnet was turned off and the samples were removed. Figure 3.4 shows the magnetic annealing during external field at 14 Tesla.

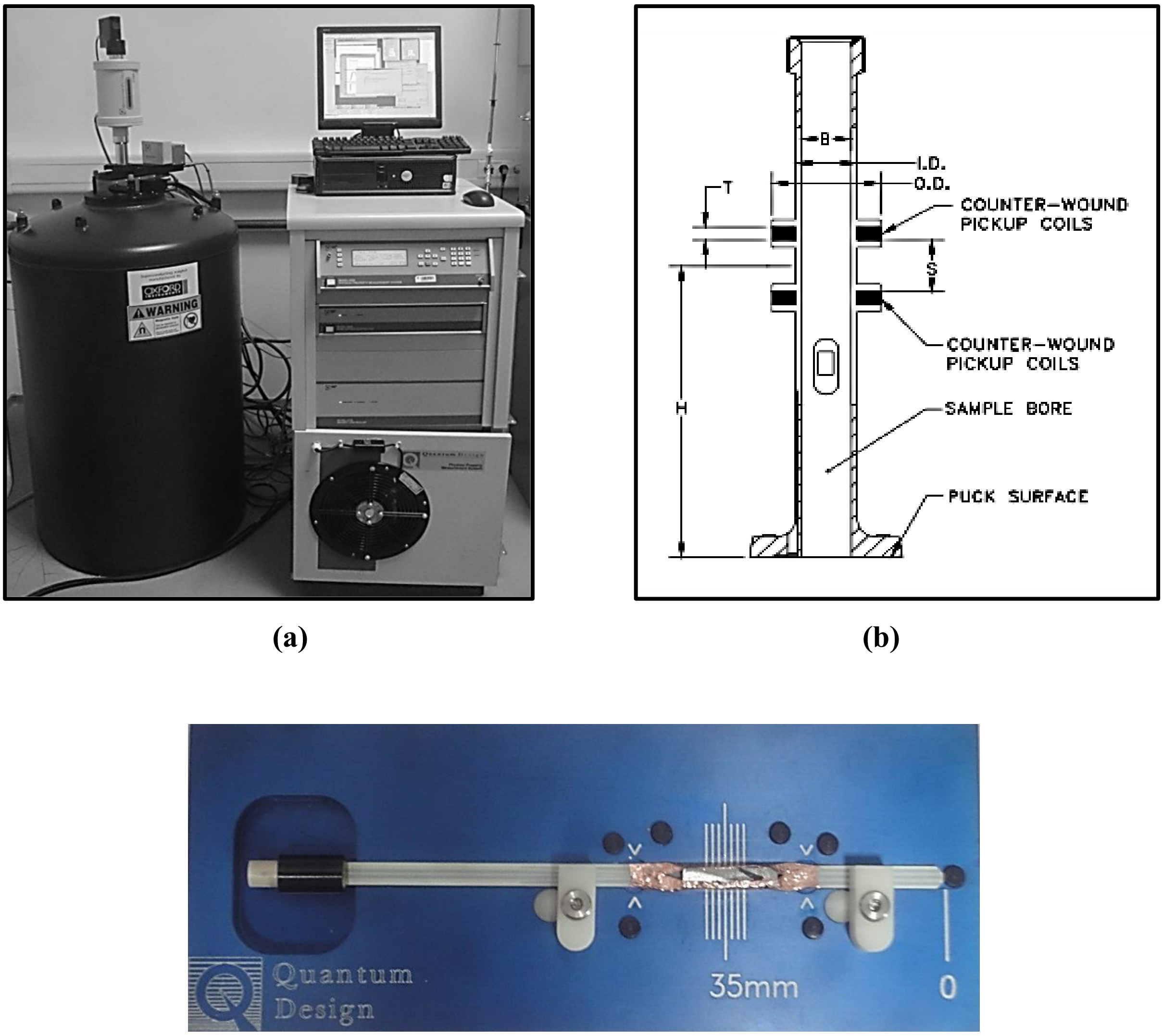

(a) **(b)**

(c)

Figure 3.2: **a)** The magnetic annealing device with the furnace **b)** The internal dimensions of a standard coil set puck **c)** Sample holder containing the samples, thermocouple, and a heater wrapped into copper foil to ensure a good thermal equilibrium

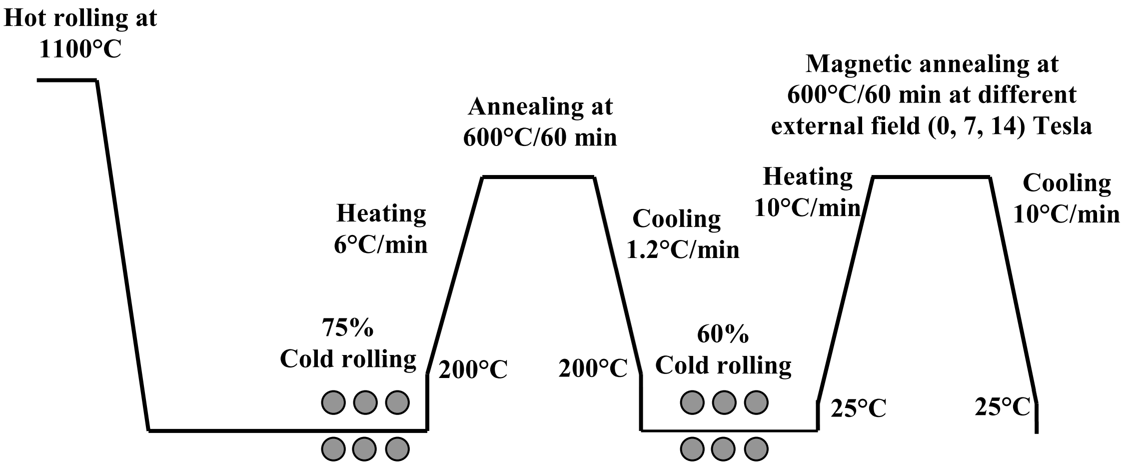

Figure 3.3: The schematically presentation of the processing parameters

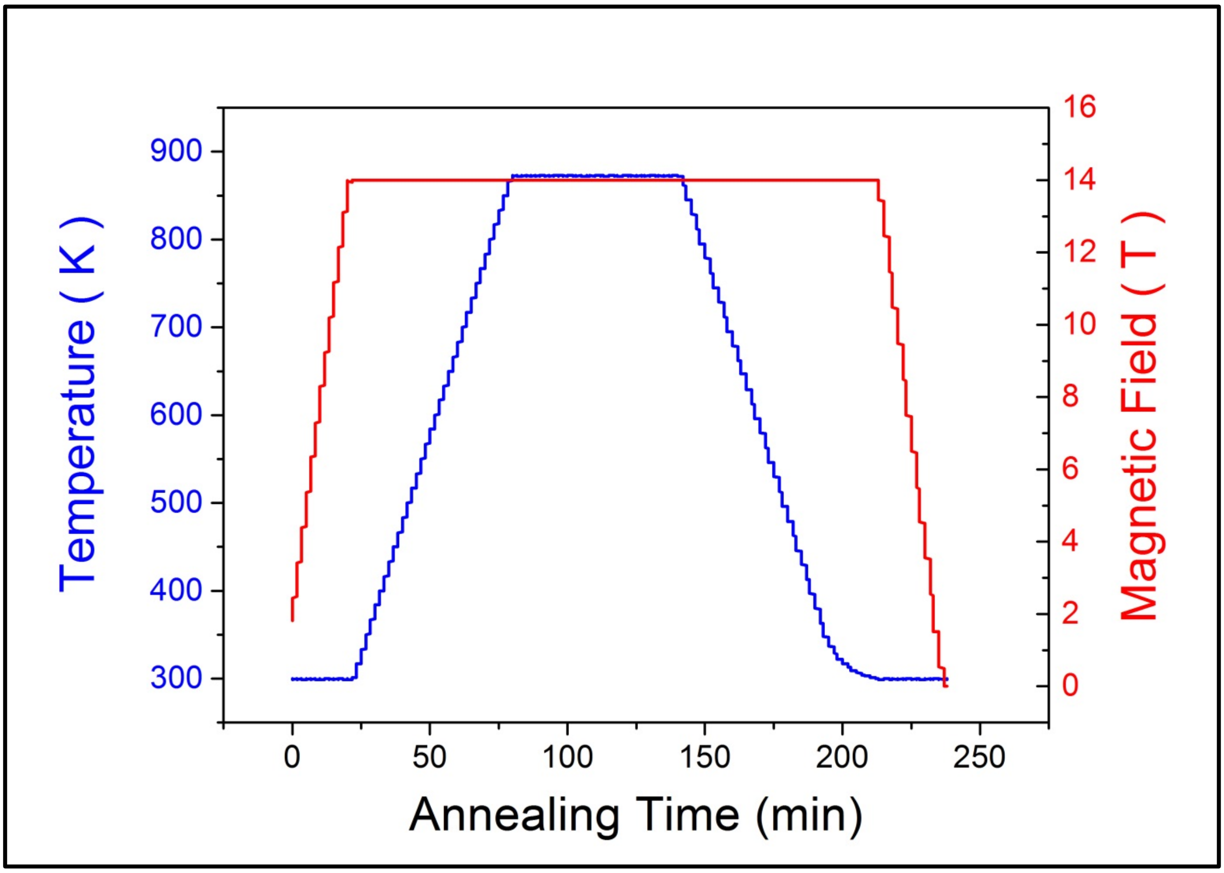

Figure 3.4: The schematically presentations of the magnetic annealing steps in the curves are artifacts due to infrequent data sampling

3.4 TEM Measurement

The specimens were investigated using a Phillips (now FEI) CM200 transmission electron microscope operated at an accelerating voltage of 200 kV. Dislocation structures were pictured using bright field conditions but no analysis of burger's vectors of single dislocations or dislocation arrangements was performed.

3.5 Metallographic Sample Preparation

For the metallographic sample preparation the specimens were cold mounted in phenolic resin. Procedure involved initial grinding using silicon carbide paper 500, 800, 1200 and 4000 at 150 rpm followed by polishing, using (6, 3 and 1) respectively micron diamond paste at a speed of 150 rpm for 10 minutes. The machine used for both grinding and polishing was a Struers, model RotoPol-21. Before microstructure measurements, an oxide polishing, using a solution of OPA (colloidal silica with grain size of approximately 0.04 mm and a PH of about 9.8) and distillate water was performed on all samples in order to eliminate any deformed or stressed layer formed during the grinding and polishing operations.

For the TEM sample preparation is to section the material in to thin wafers, approximately 500 µm (or less) in thickness and then cut 3 mm discs from the thin wafer. Affix the sample material to the glass mounting slid, after cut sample at 3 mm discs, Bulk samples should be dimpled from both side to reduce the sample thickness to approximately 100 µm using 1200 silicon carbide paper.

3.6 Chemical Etching

Etching was performed before optical microscopy measurements using 3% Nital for 3 to 5 seconds.
For TEM measurement used electro Etching, 10% perchloric (75mml) and 90% Methanol (675mml) at -35°C at 10V for 3 min.

3.7 Bulk Crystallographic Texture by using Neutron Diffraction

The pole figures measurements using neutrons were carried out at the materials science diffractometer (STRESS-SPEC) at the FRM2@MLZ (Garching, Germany) [147][148].
Figure 3.5 shows the layout of STRESS-SPEC with the sample mounted on the robot arm using a continuous scanning mode for intensity collection of complete pole figures. Continuous scanning is much faster than step scan modes and allows in parallel to optimize pole figure resolution to finer grids.

Figure 3.5: Stäubli RX160 robot with mounted sample

The sample dimensions for neutron measurements were 10 x 10 x 10 mm^3 to increase the gauge volume and to improve grain statistics needed for the annealed coarse grained material.
Therefore, ten slices were cut from the 1mm thick sheet with marked RD and glued together, using the spherical sample method of Tobisch and Bunge [149] the average texture of the whole sample can be obtained by a large enough beam cross section, in our case 25mm, see Fig. 3.6a.
The measurement was carried out with a pyrolitic graphite monochromator (PG) and a monochromator take off angle which allows working with PG $_{(004)}$ and PG $_{(006)}$. The main advantage in using two wavelengths is to save counting time getting all needed pole figures with one detector set up. The used area detector of 300x300mm^2 gave the Fe (110) reflection with PG $_{(004)}$ and Fe (200) and Fe (211) with PG $_{(006)}$ (see Fig. 3.6b).

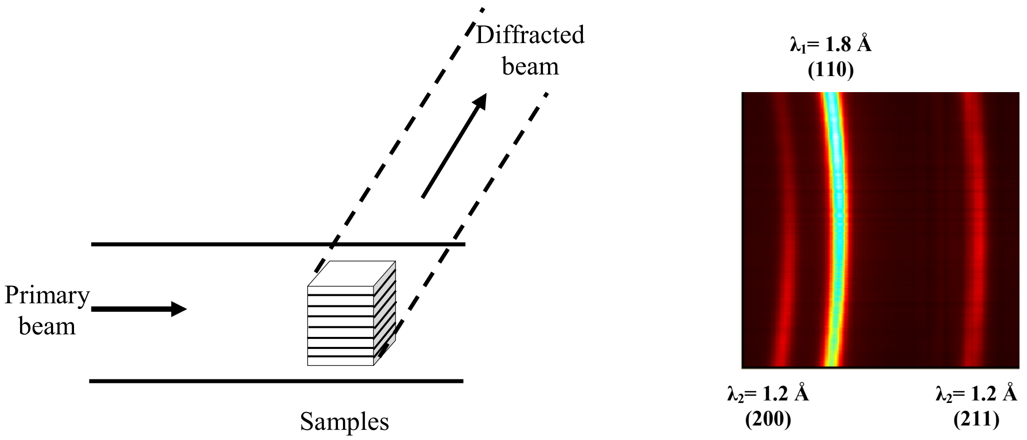

a **b**

Figure 3.6: a) Schematic view of set up, **b)** diffraction image with two wavelengths

Stress-Spec is equipped with a sample magazine which can be handled by the robot automatically and that's all sample of each cycle can be measured without manual sample changing. Pole figure collection for one sample was done in about 1.2h to get 72 readouts during continuous rotation and 6 tilt angles due to the detector size.

A software package StressTextureCalculator (STeCa) [150] has been used to extract pole figure data from area detector using the mathematical formulation of Bunge and Klein [151]. The Orientation Distribution Function (ODF) was calculated from three complete pole figures (110), (200) and (211) by ISEM (Iterative Series Expansion Method) up to a degree of series expansion Lmax = 22 [53]. The parameters of the Neutron diffractometer are listed in table 3.2.

Table 3.2: Neutron diffractometer parameters

Wavelength Å	1.8 and 1.2 (Beamtime No. 1)
Wavelength Å	1.72 and 1.42 (Beamtime No. 2)
Monochromator	PG $_{(004)}$ and PG $_{(006)}$
Detector	area detector, 300x300mm^2
Slit size (mm)	Primary slit 25x 25 mm^2
Detector distance (mm)	850
2-Theta angle (°) (hkl)	54.8(110), 54.6(200) and 55.4(211)

3.8 Dislocation Density Evaluation by using Monochromatic Synchrotron Radiation

During cold rolling and annealing, crystallographic texture and microstructure will change heavily. The influence of thermo-mechanical treatment on the defect evolutions is the main goal. The experiment has been performed at the **H**igh **E**nergy **M**aterials **S**cience Beamline HEMS@ Petra III using energy of 87.8keV (wavelength of 0.1423 Å). A beam size of 500µm x 500µm was used to get sufficient grain statistics. The sample to detector distance was 1100 mm. An area detector type **P**erkin **E**lmar (PE) with a resolution of 200µmx200µm was used with an exposure time of 4 seconds. To analyses the instrumental line broadening and to make adjustment corrections an Al2O3 NIST standard plate was measured. The typical line broadening of the Al2O3 standard is 0.021°. Due to the high brilliance of the synchrotron beam and the low line broadening the penetrated sample thickness plays an important role which is given in table 3.3 for the investigated samples and also Fig. 3.7 show the diffraction pattern of two steps cold rolling with intermediate annealing at 600°C. The Fe2.6%Si sheet plates were oriented with the rolling plane perpendicular to the beam direction and with the rolling direction (RD) as shown in Fig. 3.8 [152].

Table 3.3: Measured samples and thickness

Sample treatment	Thickness
90% cold rolling	1.0mm
75% cold rolling	2.5mm
75% cold rolling + 600°C/60min	2.5mm
75% cold rolling + 600°C/60min + 60% cold rolling	1.0mm
Al2O3 standard	1.5mm

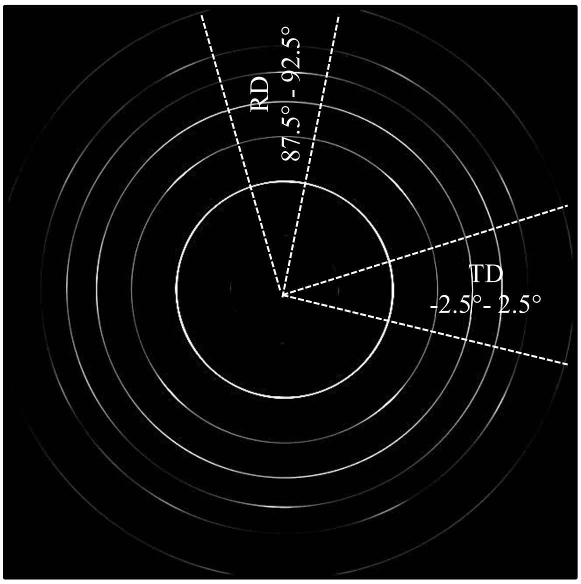

Figure 3.7: Example of a diffraction pattern

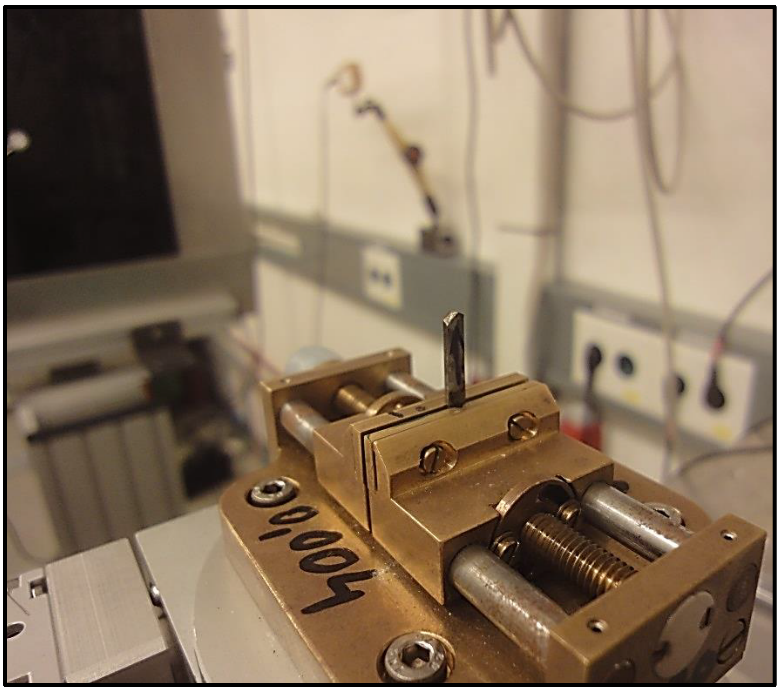

Figure 3.8: Fe-2.6%Si Sample fixed on sample stage at HEMS@ Petra III PO7B (HEMS-side station)

3.9 Hardness

The hardness was determined by hardness test method using a carbide ball with 2.5 mm diameter in a Brinell tester, a normal force of 1839 and a loading time of 15 seconds. The hardness tester conforms to the N according to the DIN ISO (6206). The average of three measurements was taken at each depth to construct the hardness depth profile.

Microhardness for the magnetic annealing samples was determined by means of a Struers Duramin tester using a square base pyramid shaped indenter for testing in a Vickers tester, a nominal force of 2 kgf (HV2) and loading time of 10s. The hardness tester conforms to the N according to the DIN ISO (6507). The average of three measurements was taken at each depth to construct the hardness depth profile.

3.10 Measurement of Magnetic Properties

Samples for magnetic measurement were rectangular bars 1 x 1 x 25 mm^3 and 1 x 1x 15 mm^3 for the magnetic annealing samples. Measurements were done with a digital hysteresis recorder as shown in Fig. 3.9. Recorder is described in details elsewhere [153]. For purposes of comparability of magnetic sample's properties measurement has been made at identical polarizations and magnetizing frequencies by varying the magnetic field strength.

The magnetic properties of Fe-2.6%Si samples measured at a magnetizing frequencies of 10Hz and 50Hz except the magnetic annealing samples measured at 10Hz only and a maximum polarization of J_0=1.8T. The saturation polarization was estimated to be J_s=2.04T which corresponds to the values found in literature for Fe2.6%Si [2].

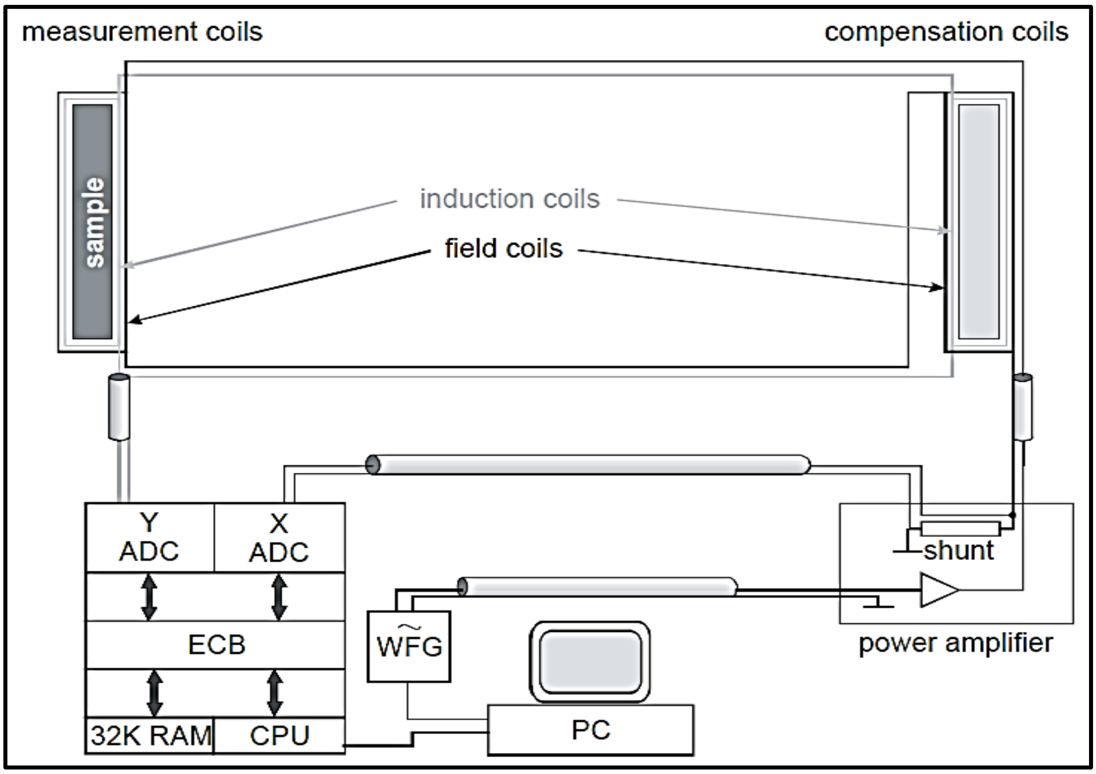

Figure 3.9: Schematic drawing of the used hysteresis measurement system device

4. Results and Discussions

4.1 Introduction

This chapter will present the results of crystallographic texture, microstructure, magnetic properties and dislocation density obtained through neutron diffraction, optical microscopy; digital hysteresis recorder and synchrotron measurement for deformed and annealed Fe-2.6 % Si samples.

This chapter will be presented the results obtained after 97% hot rolling, one stage 90% cold rolling annealed the samples at different annealing temperatures at (600°C, 700°C, 900°C and 1100°C) for (20 and 60) minute, two stages cold rolling (at 75% and 60% reduction) with intermediate annealing process at 600°C/60 min and after second stage cold rolling (at 60 % reduction) annealed the sample at 800°C/ 60 min. The heat treatments of Fe-2.6% Si samples, magnetic annealing, was annealed at 600°C/60 min at different external fields at (0, 7 and 14 Tesla) after thermo-mechanical process (two stages cold rolling with intermediate annealing processes), The dislocation density are evaluated by using modified Williams method after each cold rolling processes and the magnetic properties such as power loss, permeability and coercive force are measured for each samples at (10 and 50) Hz.

The most interesting fiber texture for silicon steel are the (α fiber (<110> ||RD) fiber, (h k l) [h/l + 1 h/l + 2 h/l], θ fiber <100>||ND, η fiber <100>||RD and γ fiber <111>||ND) and the development of these fibers as well as the variation in their volume fraction with different (rolling process, rolling reduction, annealing temperature, annealing time, external field).

The results will be shown in the form of pictures, graphics and tables that will be commented and briefly discussed.

4.2 Texture and Microstructure Evolution

4.2.1 As-Received (Hot rolling)

The microstructures of 97% Fe-2.6%Si at rolling, transversal and normal planes are shown in Fig. 4.1 a, b and c. The micrograph of the hot rolled band shows a mixture between smooth type and grooved type of microstructure.

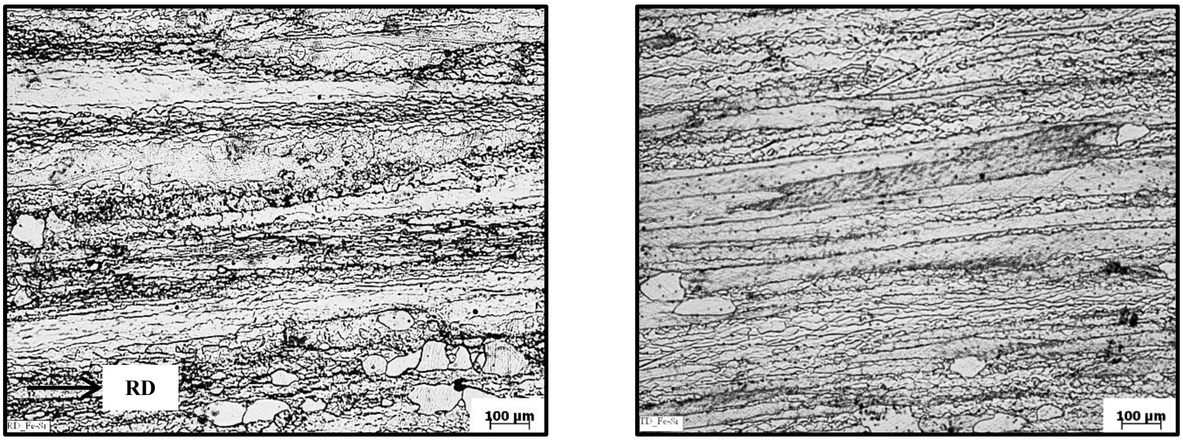

a) RD-TD Plane **b)** TD-ND plane

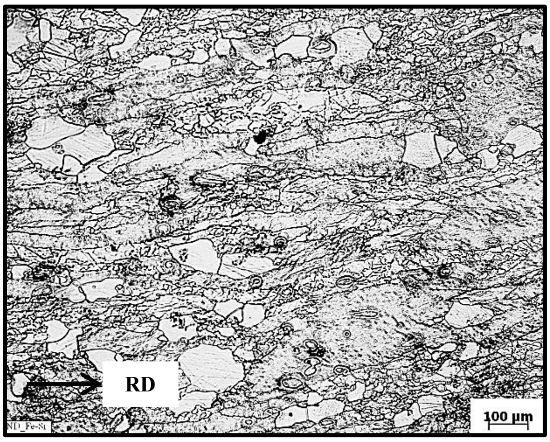

c) RD-ND Plane

Figure 4.1: Microstructure of Fe 2.6 % (HR) **a)** Rolling Direction (RD), **b)** Transvers Direction (TD), **c)** Normal Direction (ND)

The “smooth” microstructure containing orientations between (001)[110] and (112)[110] with continuous orientation changes between neighboring areas. Also in this type, a continuous spread of (001)[110] towards (001)[100]. A “grooved” microstructure, which are composed of orientations of the <111>||ND family, mainly the orientation (111)[211], the two symmetry various of which are alternating with no continuous transition between them. This structural type is thus in good agreement with a <111>||ND fiber texture component having a highest orientation density at (111)[112] [154][155].

The most common texture components and orientation fibers in steel after rolling and recrystallization are presented in the ODF sections $\varphi_2= 0°$ and $\varphi_2= 45°$, as shown in Fig. 4.2.

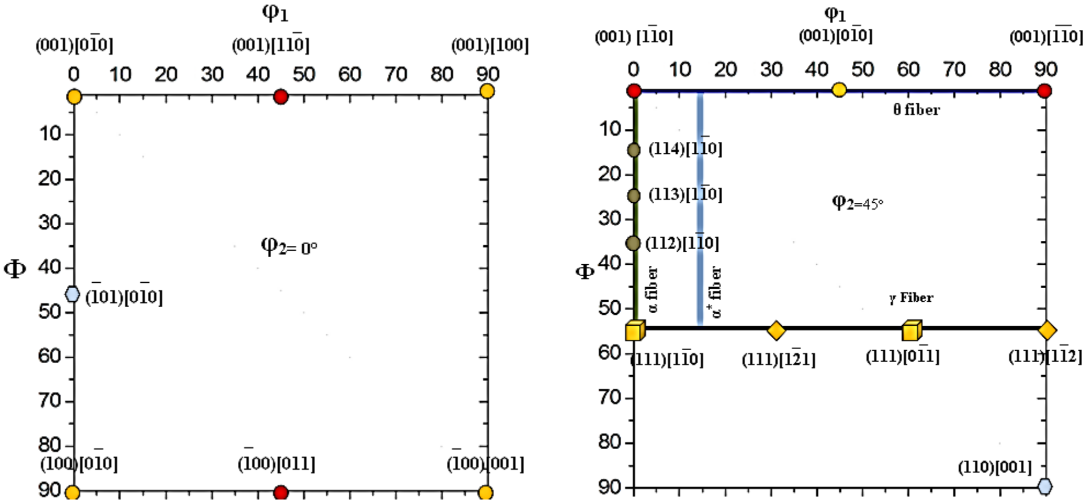

a) **b)**

Figure 4.2: a) $\varphi_{2=}$ 0°, **b)** φ_2= 45° ODF sections in Euler space showing the main texture components in steel

The global crystallographic texture of the 97% hot-rolled Fe-2.6%Si (HR) has been evaluated by using neutron diffraction in terms of the measured pole figures as shown in Fig. 4.3.

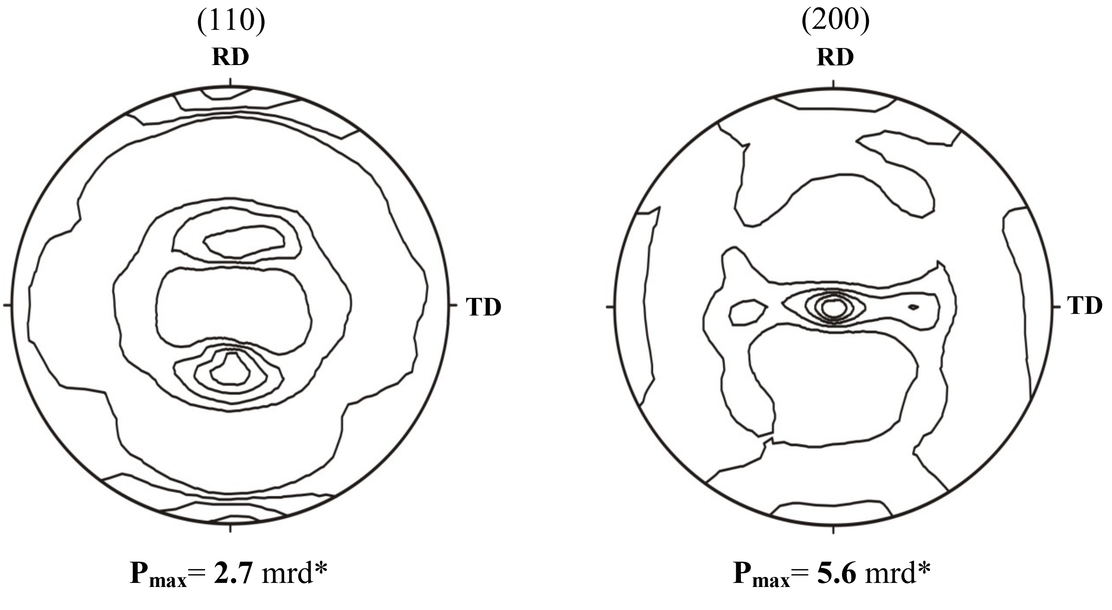

a) **b)**

Figure 4.3: a) 110 **b)** 200 pole figures of the 97% hot rolled of Fe-2.6%Si

*m.r.d = multiples of random distribution

The texture of the hot rolled sample shows a high intensity spread along the θ fiber <001>||ND between (001)[1-10] rotated cube component to the cube component (001)[0-10] and to (001)[-1-10] rotated cube, an α fiber <110>||RD and a γ fiber as shown in Fig. 4.5a. The Goss {110}<001> component of texture appeared due to the hot rolling at high temperature [156].

Due to the cutting the former RD becomes TD and consequently the starting texture for cold rolling changes as shown in Fig. 4.4 [177].

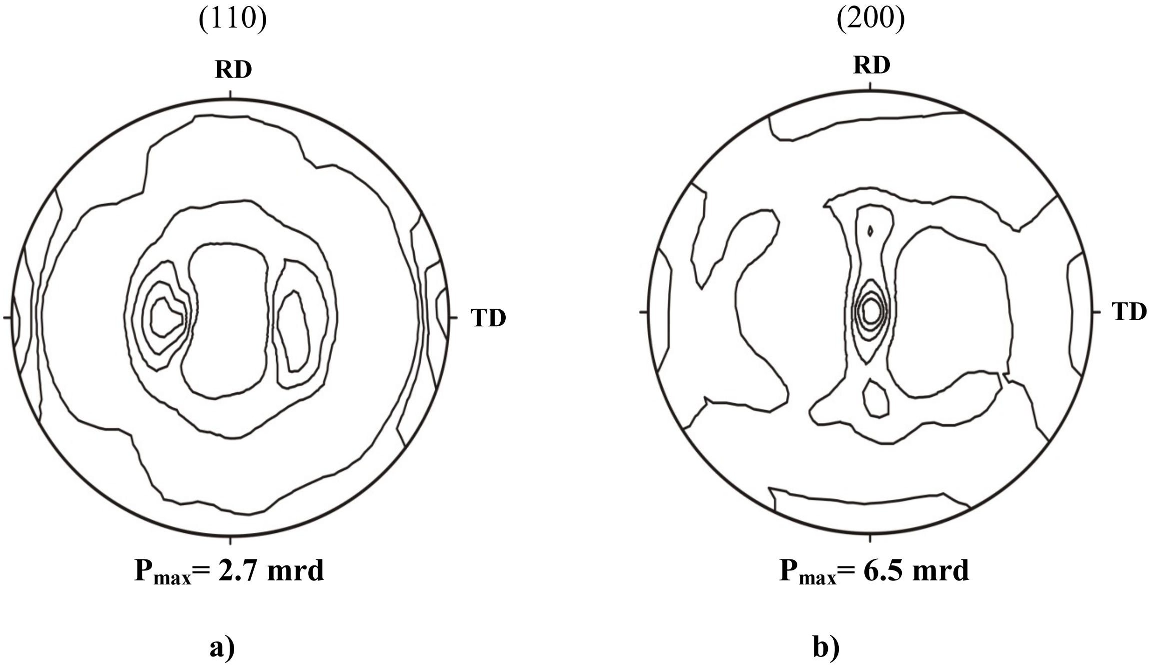

Figure 4.4: a) (110) **b)** (200) pole figures of the hot rolled Fe-2.6%Si after 90° rotated at ND

The Orientation Distribution function (ODF) was evaluated after rotated 90° around ND as shown in Fig. 4.5b.

As it is shown in Fig. 4.6, the **α** and **ε** fibers which is developed due to the rotation of 90° around ND. All <110> fibers parallel to the rolling direction are transferred into <110> fibers parallel to transversal direction of hot rolling [177].

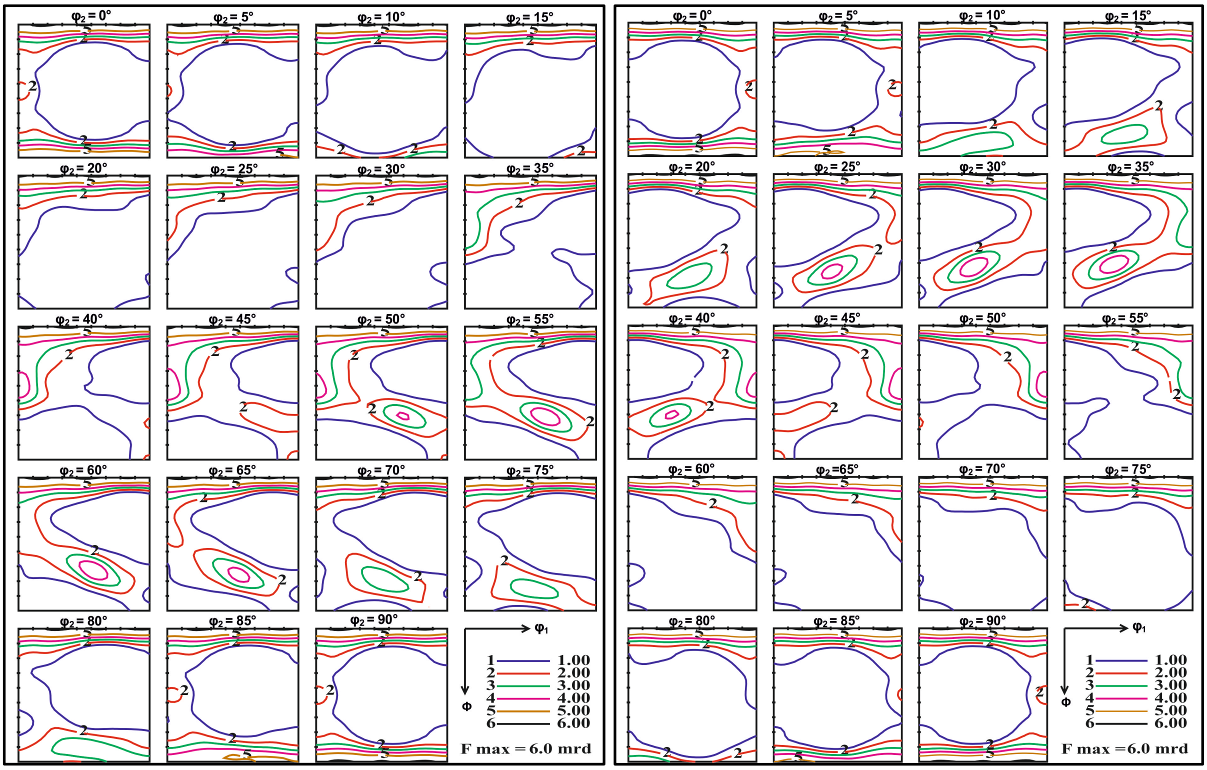

a) **b)**

Figure 4.5: a) ODF sections showing texture for as-received material (HR). **b)** ODF sections showing texture for as-received material after 90° rotated at ND (HR)

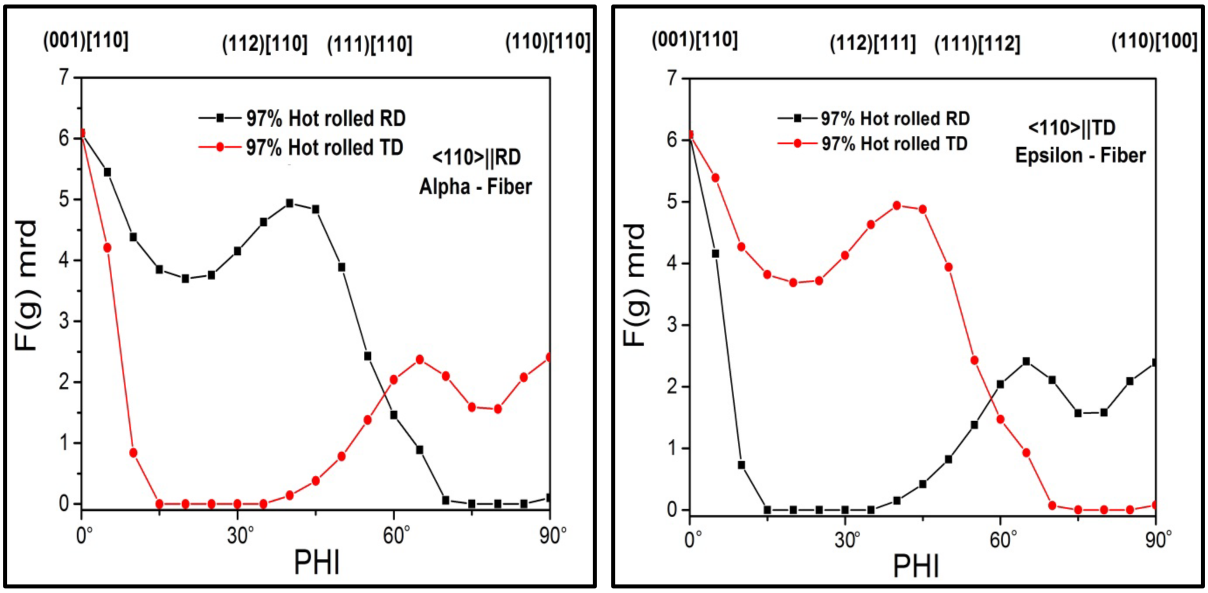

Figure 4.6: The **α** and **ε** fibers of 97 % hot rolled before and after rotation of 90° around ND

4.2.2 Cold Rolling at One Stage

In order to control the recrystallization texture, the starting texture has very important rules play during the annealing of cold rolled sheet a selection which have developed during the cold rolling process. Therefore, it should be attempted to form as few as possible unfavorable orientation of the α and γ fibers as a result of rolling strain these are the stable end orientations which appear after conventional rolling reduction of 60 to 80% [157][158].

The microstructures of 90% rolled of Fe-2.6%Si at rolling, transversal and normal planes are shown in Fig. 4.7 a, b and c. The micrograph of the cross cold rolling shows a smooth type of microstructure [177].

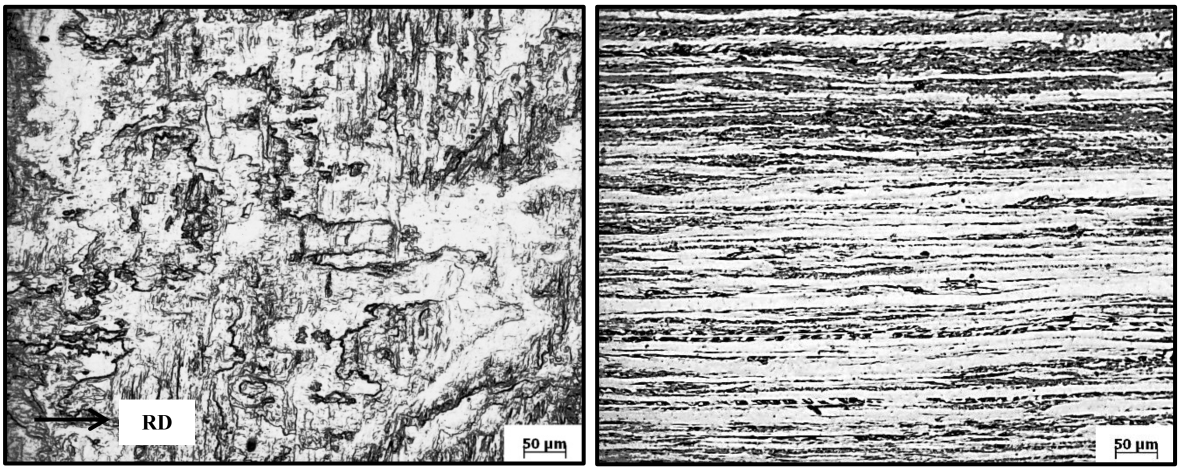

a) RD-TD Plane **b)** TD-ND Plane

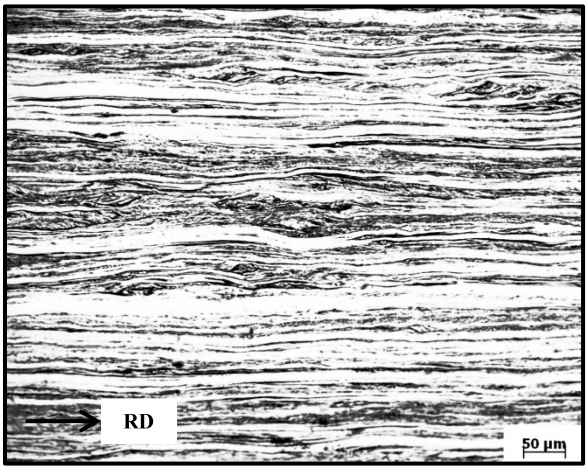

c) RD-ND plane

Figure 4.7: Microstructure of 90% cold rolled (CR) a) Rolling direction (RD), b) Transvers direction (TD) c) Normal direction (ND)

During cold rolling the crystallite orientations produced in hot rolling process rotate as expected [159]. Such a cross rolling produces a very strong {001}<110> texture, as it is shown in Fig. 4.8, which is developed due to the rotation of 90° around ND. All <110> fibers parallel to the rolling direction are transferred into [110] fibers parallel to transversal direction of hot rolling and the subsequent 90% cold rolling process finally converts them to a rotated cube component (001)[110] [177].

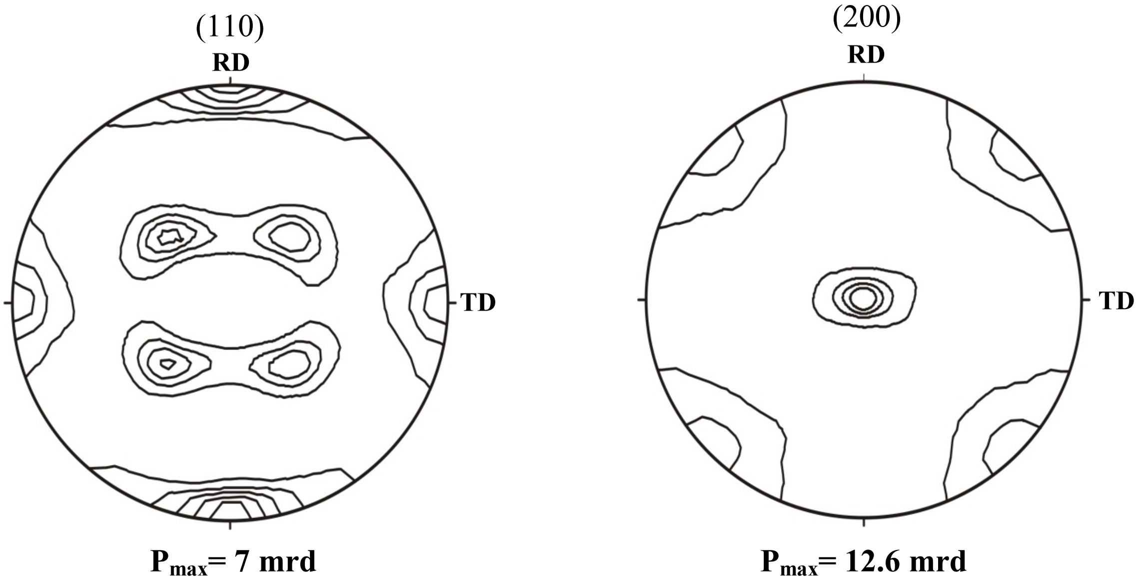

a) **b)**

Figure 4.8: a) (110) **b)** (200) Pole figures of the 90% cold rolled of Fe 2.6%Si

The Orientation Distribution function (ODF) was evaluated as shown in Fig. 4.9. The result observed a maximum intensity located at rotated cube components (001)[110], also the maximum intensity spread along α fiber and very weak intensity spread along the γ fiber [177].

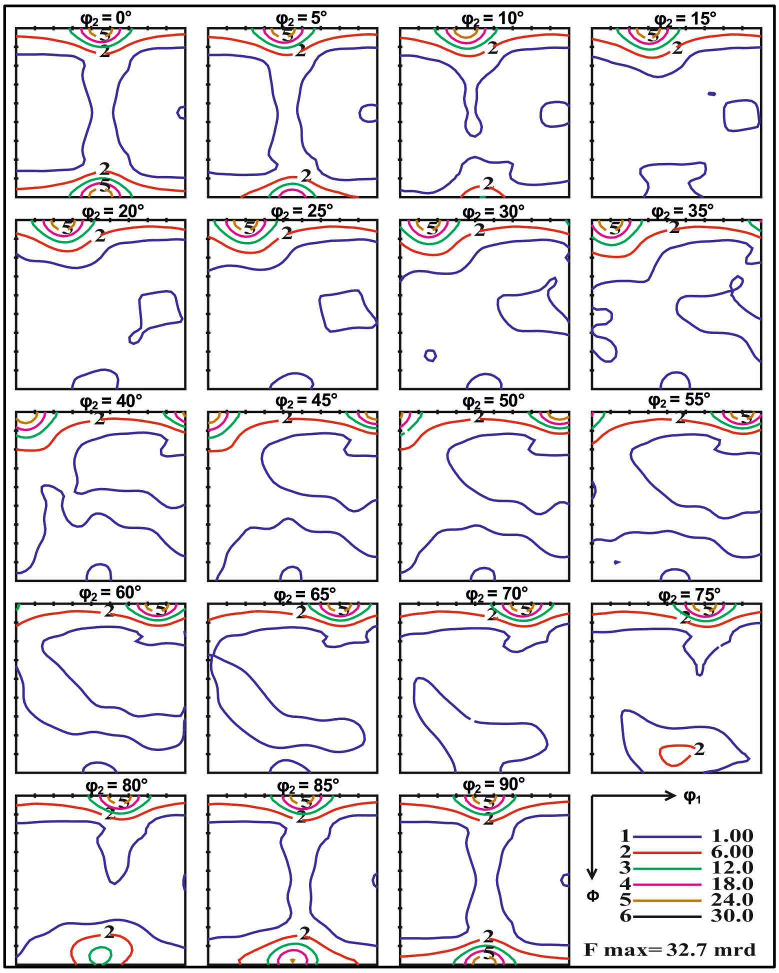

Figure 4.9: ODF sections showing texture for 90 % cold rolling (CR)

4.2.3 Cold Rolling Plus Different Annealing Temperatures for 20 min

The resulting of microstructure of the 90% cold rolling plus annealing at (600°C, 700°C, 900°C and 1100°C) for 20 minute and cooling by air are shown in Fig 4.10 from (a to m), the type of microstructure exhibits equiaxed grains.

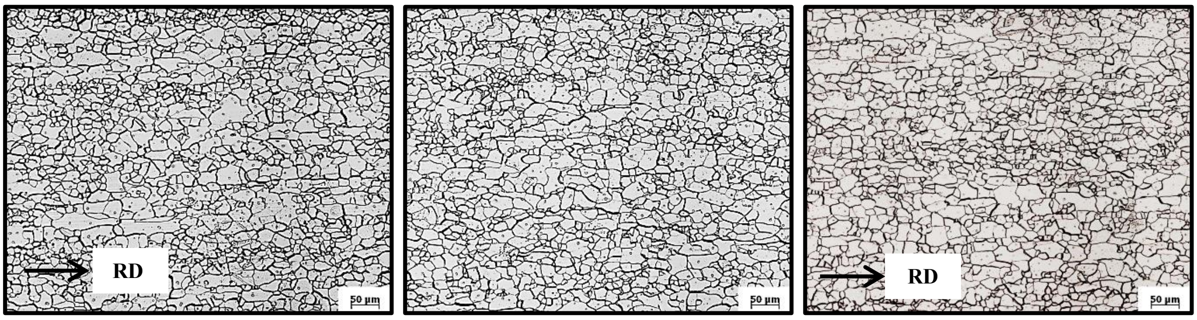

a) 600°C/ 20 min (RD-TD) **b)** 600°C/ 20 min (TD-ND) **c)** 600°C/ 20 min (RD-ND)

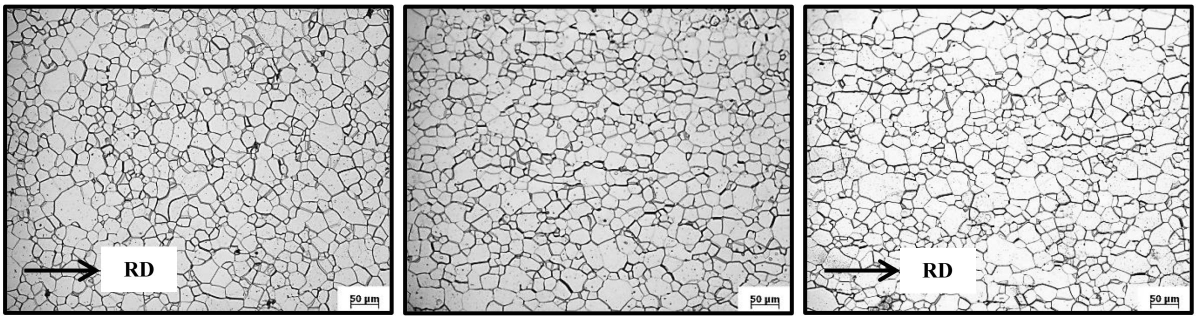

d) 700°C/ 20 min (RD-TD) **e)** 700°C/ 20 min (TD-ND) **f)** 700°C/ 20 min (RD-ND)

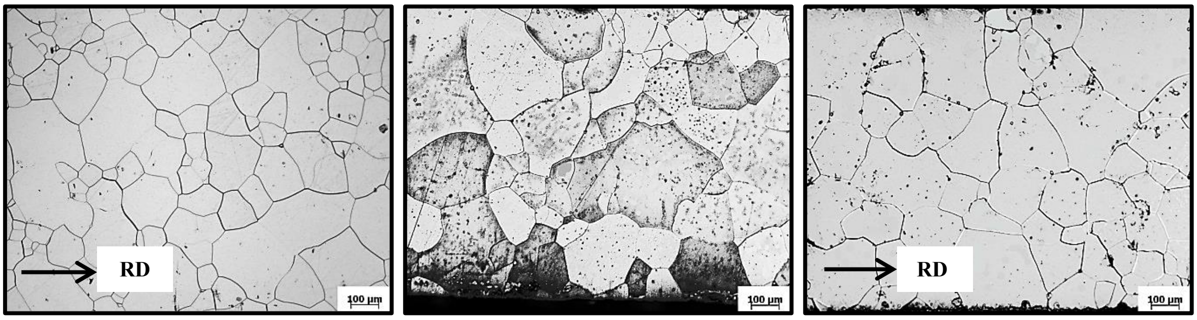

g) 900°C/ 20 min (RD-TD) **h)** 900°C/ 20 min (TD-ND) **i)** 900°C/ 20 min (RD-ND)

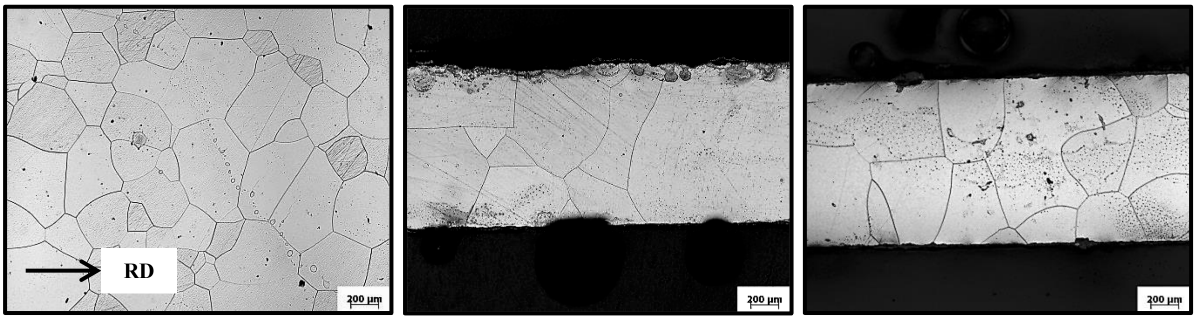

k) 1100°C/ 20 min (RD-TD) **l)** 1100°C/ 20 min (TD-ND) **m)** 1100°C/ 20 min (RD-ND)

Figure 4.10: Optical micrograph of 90% cold rolling plus different annealing temperatures for 20 minute

The magnetic properties of electrical steel are strongly depend on recrystallization and grain size morphology after hot and cold rolling process. The size of electrical steel and the absences of impurities like dislocation, grain boundaries or precipitations are the most important factors determining power loss.

The development of recrystallization textures is evaluated by nucleation and grain growth. Figure 4.11 shows the pole figures after 90% cold rolling annealed the sample at different temperature (600°C, 700°C, 900°C and 1100°C) for 20 minute. During the primary recrystallization annealing at 600°, the texture results observed that the homogeneous intensity spread along the α, α* fiber and the γ fiber as shown in fig. 4.12a [188].

After annealed the sample at 700°C as shown in Fig. 4.12b, the results observed more intensity spread along the α fiber than the γ fiber, particularly increasing at the Euler angles of the orientation (φ_1 ,Φ, φ_2) ≈ (15, 35, 45) which corresponds to the following approximate set of miller indicate (112) [7 -11 2][47]. This local maximum lies on a secondary fiber parallel to the α fiber (<110>||RD), running from the (111)[112] components to the cube fiber [188].

Figure 4.12c shows the crystallographic texture after annealing the sample at 900°C, the result observed a high intensity spread along the α fiber, particularly strongest intensity of the (112) [7 -11 2] and the γ fiber shows no any connection between (111)[110] and (111)[112] with slightly change in the intensity of (111)[112].

Figure 4.12d shows the crystallographic texture after annealing the sample at 1100°C, the results shows that the increasing of the intensity spread along the α fiber (<110>||RD) and θ fiber (<001>||ND) drastically also disappear the components of the γ fiber. The recrystallization textures in iron silicon depend on deformation texture and microstructure than on recrystallization temperature [161][162] itself, the recrystallization and gain growth results texture observed a high intensity spread along <110>||RD fiber than <111>||ND fiber [188].

To have still more quantitative information it is useful to plot the orientation densities *f* (g) along the fiber, i. e. as function of the angle of rotation around the fiber axis, A more details are given in Fig. 4.13 where beside the α fiber and the γ fiber also the η and the **ε** fibers. Exist this will be used as a standard way for presenting cold rolled and recrystallization textures for electric steels [188].

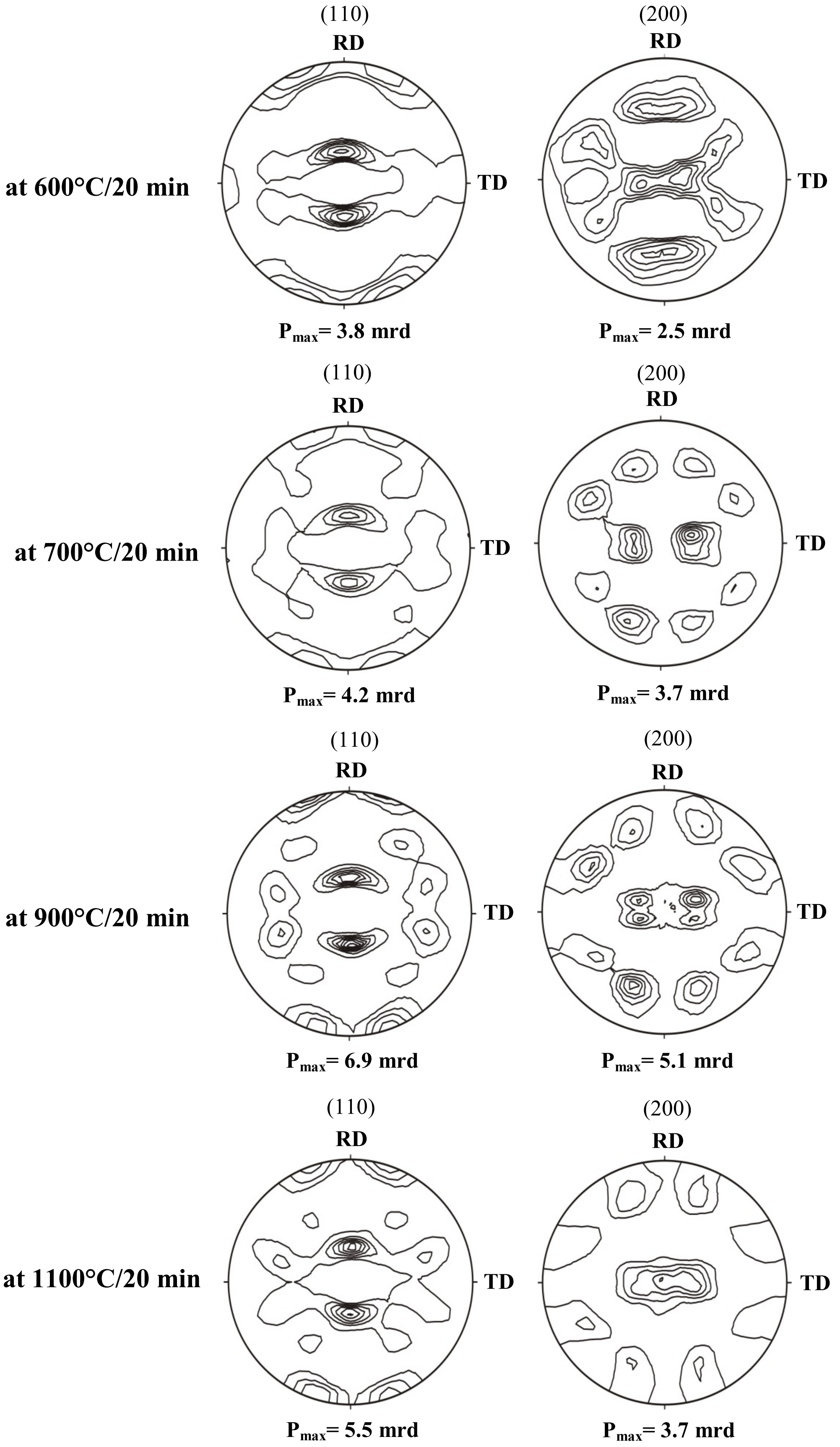

Figure 4.11: (**110**) and (**200**) pole figures of the 90% cold rolling plus different annealing temperatures for 20 min

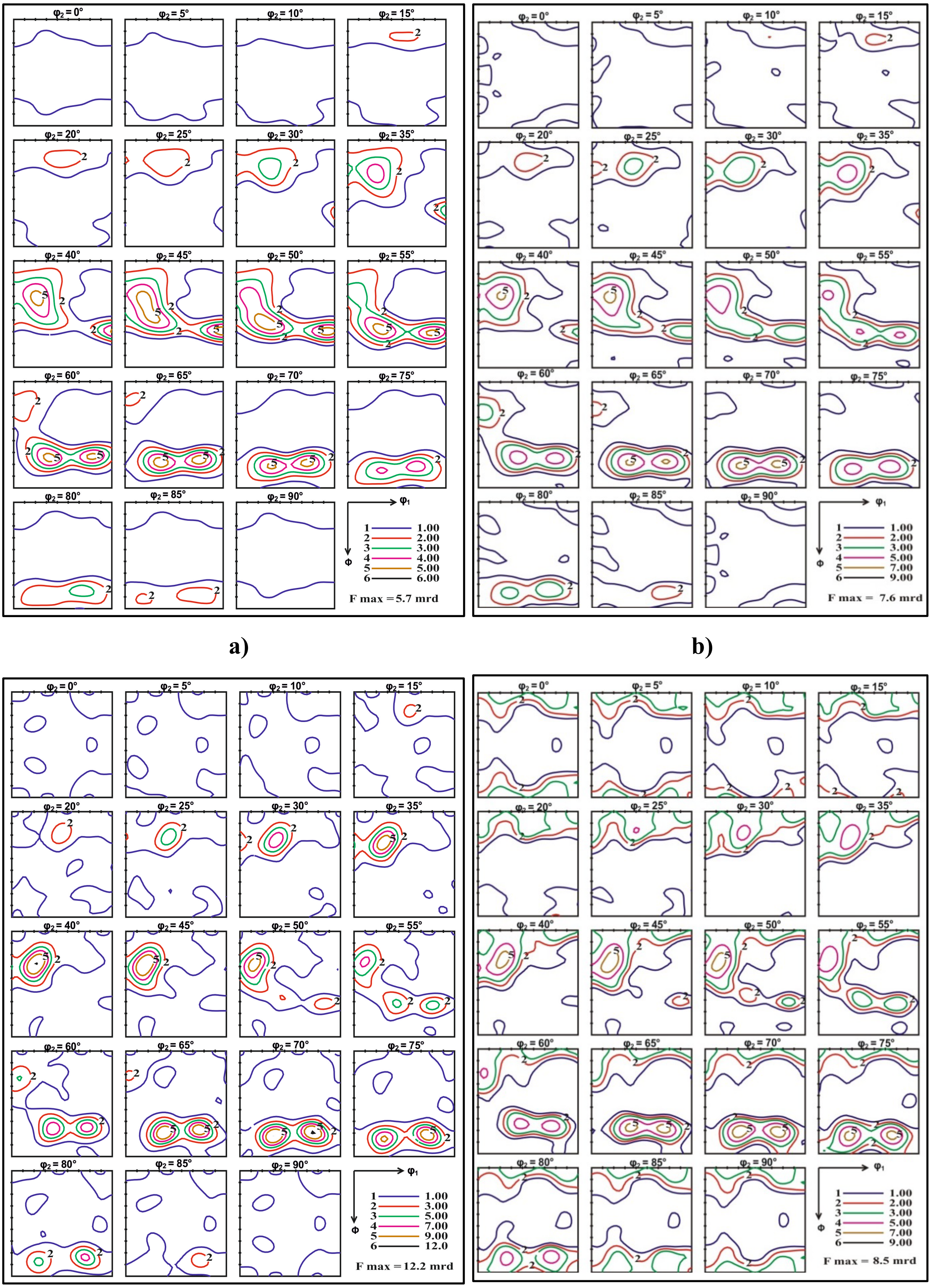

a) **b)**

c) **d)**

Figure 4.12: ODF sections showing texture for 90 % cold rolling plus different annealing temperatures for 20 min **a)** 600°C **b)** 700°C **c)** 900°C **d)** 1100°C

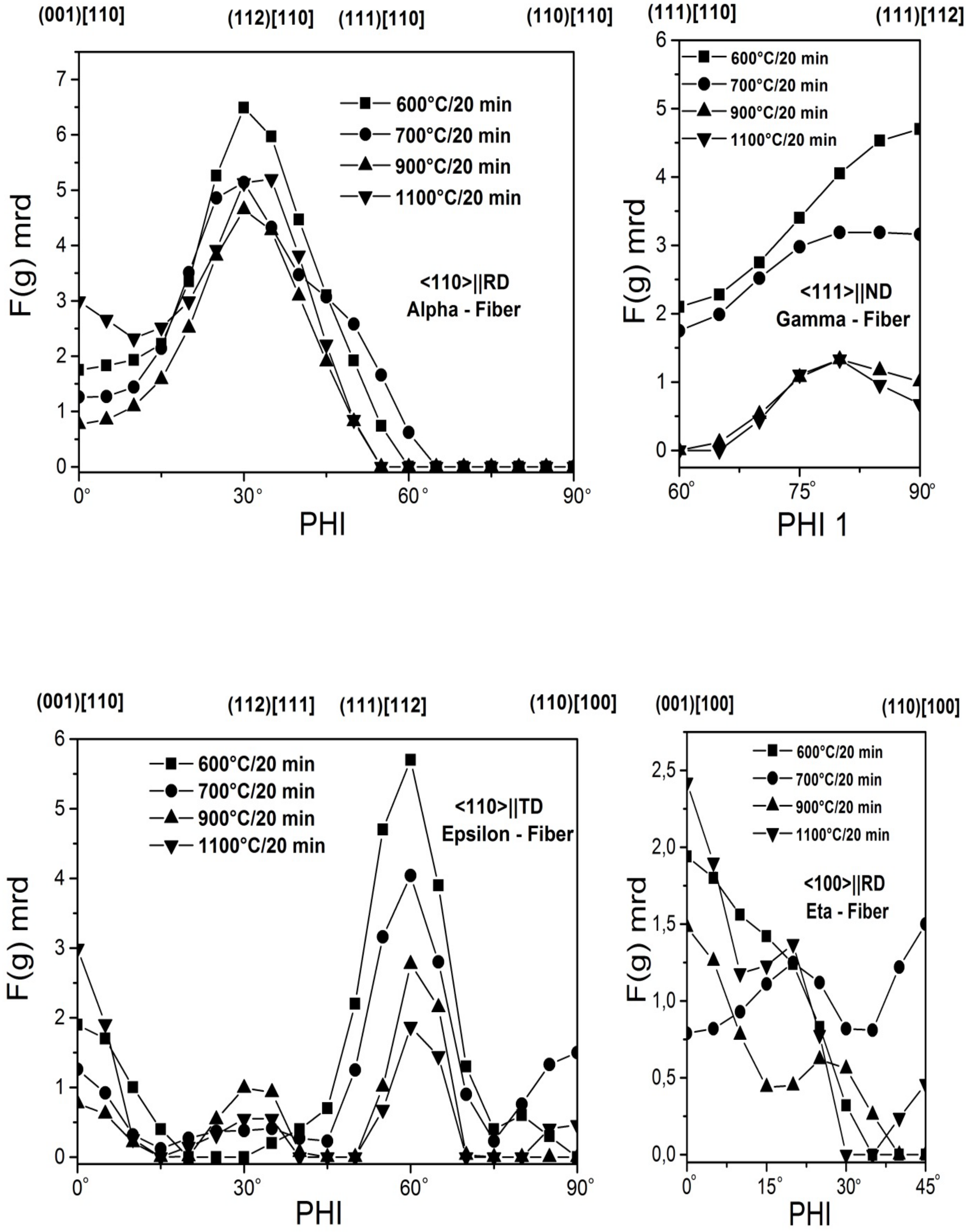

Figure 4.13: The **α, γ,** η and **ε** fibers of 90% cold rolling at annealing at 600°C, 700°C, 900°C and 1100°C for 20 min [188]

4.2.4 Cold Rolling Plus Different Annealing Temperatures for 60 min

The resulting of microstructure of the 90% cold rolling plus annealing at (600°C, 700°C, 900°C and 1100°C) for 60 minute and cooling by air are shown in Figure 4.14 from (a to m), the type of microstructure exhibits equiaxed grains.

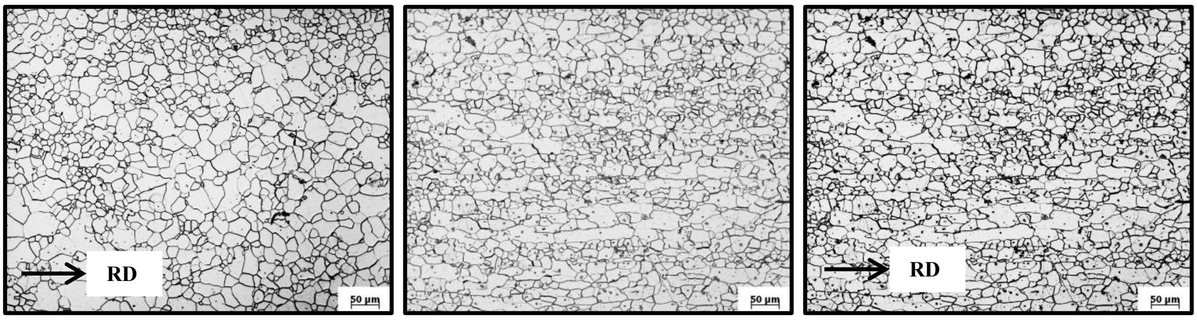

a) 600°C/ 60 min (RD-TD) **b)** 600°C/ 60 min (TD-ND) **c)** 600°C/ 60 min (RD-ND)

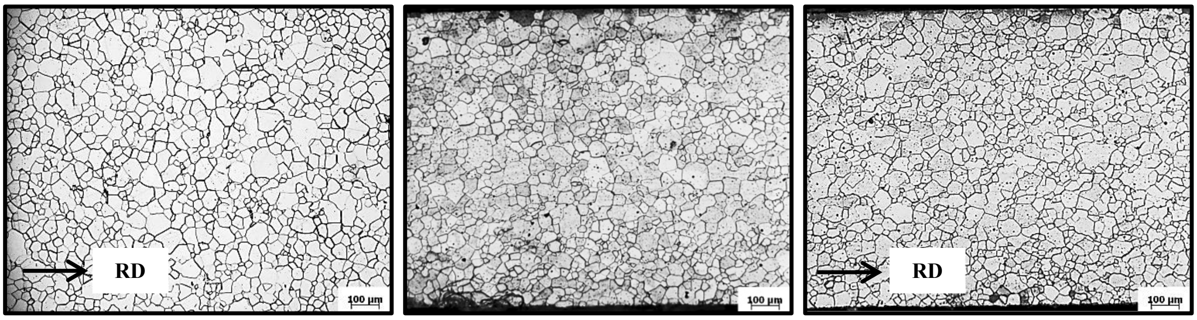

d) 700°C/ 60 min (RD-TD) **e)** 700°C/ 60 min (TD-ND) **f)** 700°C/ 60 min (RD-ND)

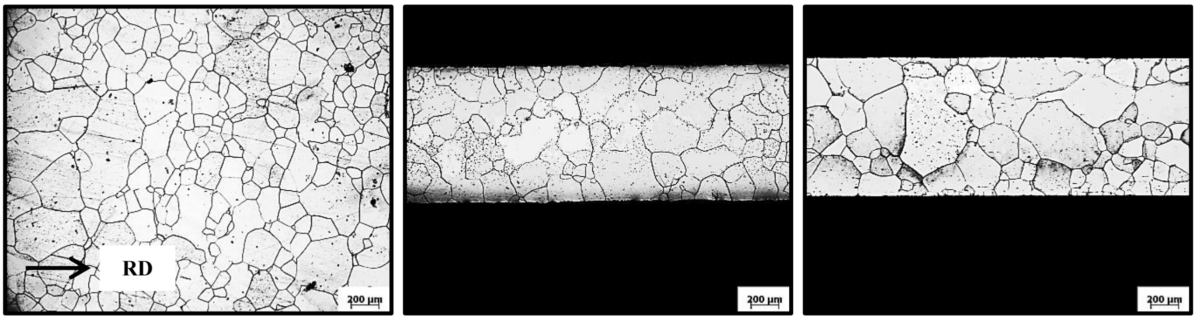

g) 900°C/ 60 min (RD-TD) **h)** 900°C/ 60 min (TD-ND) **i)** 900°C/ 60 min (RD-ND)

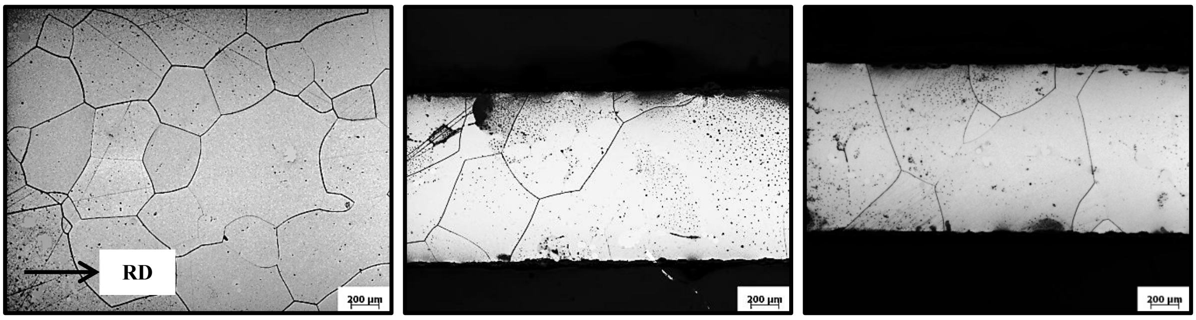

k) 1100°C/ 60 min (RD-TD) **l)** 1100°C/ 60 min (TD-ND) **m)** 1100°C/ 60 min (RD-ND)

Figure 4.14: Optical micrograph of 90% cold rolling plus different annealing temperatures for 60 minute

Figure 4.15 shows the pole figures after 90% cold rolling annealed the samples at different temperature (600°C, 700°C, 900°C and 1100°C) for full recrystallization for 60 minute.

The crystallographic texture after the primary recrystallization annealing (600°C/1h) a homogeneous intensity spread along the α fiber, the α * and the γ fiber can be observed and also the Goss {110}<001> component is initiated at primary recrystallization as it is shown in Fig. 4.16a. Depicts the texture after annealing at 700°C/1h, A higher intensity spread along α fiber than along the γ fiber, particularly increasing at the Euler angles of the orientation (φ_1, Φ, φ_2) ≈ [15, 35, 45] is observed. These angles correspond approximately to the (112)[7 -11 2] set of miller indices as shown in fig. 4.16b [47].

This local maximum in the intensity lies on a secondary fiber parallel to the α fiber <110>||RD which is running from the (111)[112] components to the cube fiber. An annealing of the sample at 900°C/1 hour lead to an increase of the intensity spread along the α fiber <110>||RD as shown in Fig.4.16c. Particularly the (112)[7 -11 2] component and a decreasing intensity spread along the γ fiber <111>||ND can be observed.

The crystallographic texture after annealing the sample at 1100°C/1h (112)[7 -11 2] is the dominating component as can be seen in Fig. 4.16d. The strength of the intensity spread along the θ fiber <001>||ND and the component of the γ fiber <111>||ND disappear. Regarding these results it can be stated that the recrystallization texture in the investigated iron silicon alloy is more dependent on the deformation texture and microstructure than on the recrystallization temperature [106][107] itself.

The recrystallization and the grain growth results in a texture for which a higher intensity spread along <110>||RD fiber than along the <111>||ND fiber can be observed in diffraction pattern [177].

To have still more quantitative information it is useful to plot the orientation densities f (g) along the fiber, i. e. as function of the angle of rotation around the fiber axis, as shown in Fig. 4.17 for the α, γ, η and ε fibers. This will be used as a standard way for presenting bcc cold rolled and recrystallization textures [177].

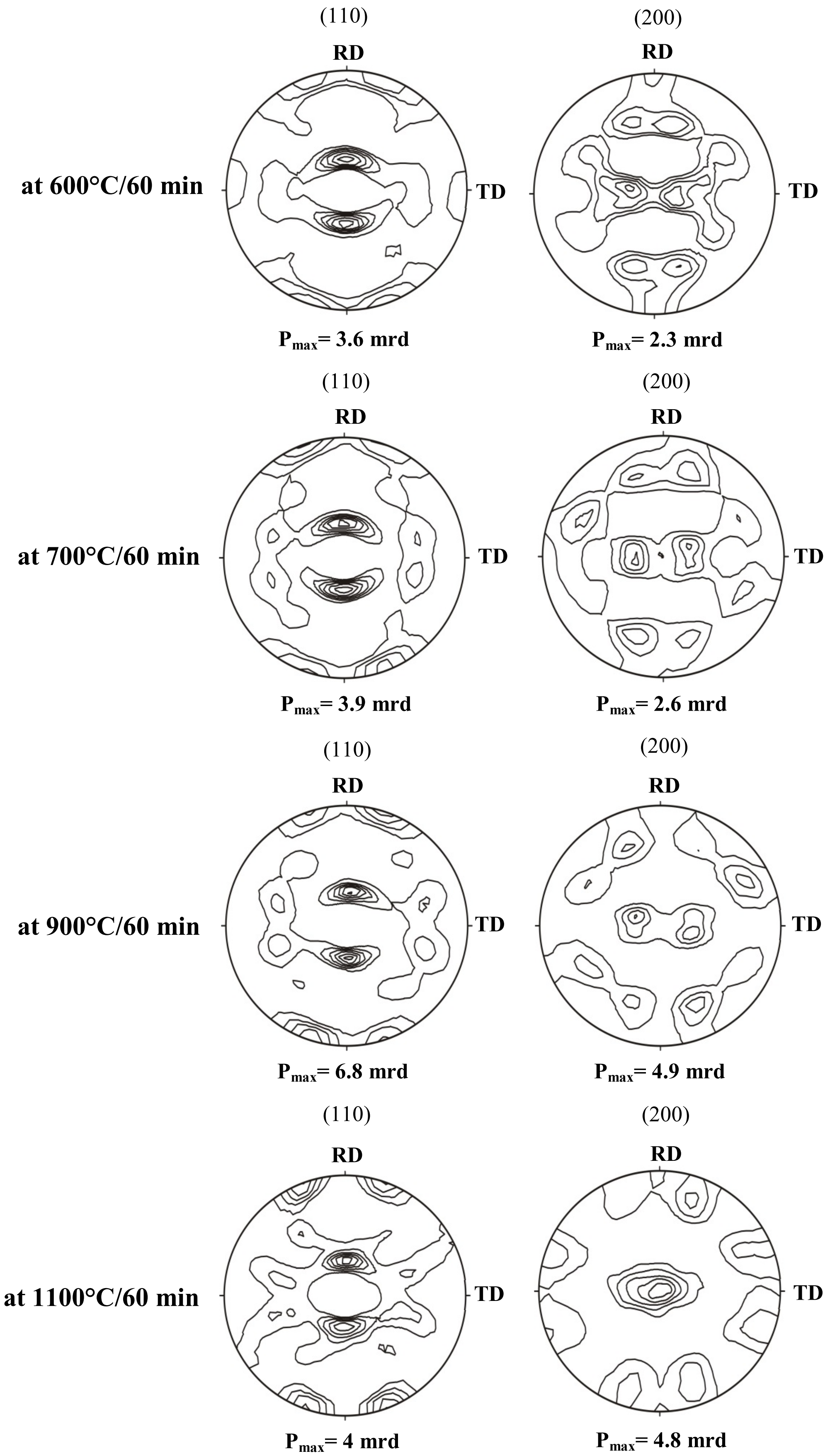

Figure 4.15: **(110)** and **(200)** pole figures of the 90% cold rolling plus different annealing temperatures for 60 min

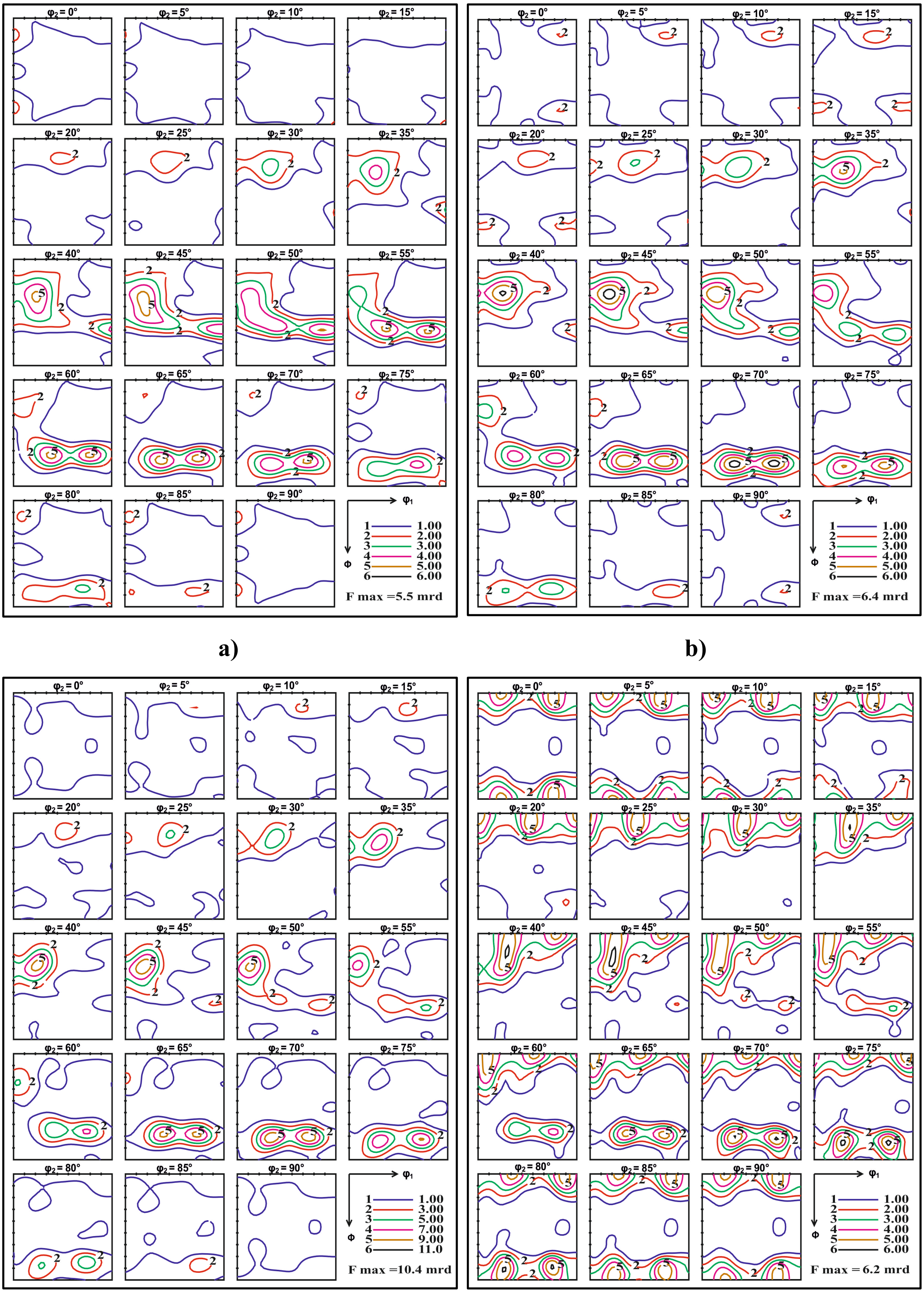

a) **b)**

c) **d)**

Figure 4.16: ODF sections showing texture for 90 % cold rolling plus different annealing temperatures for 60 min **a)** 600°C **b)** 700°C **c)** 900°C **d)** 1100°C

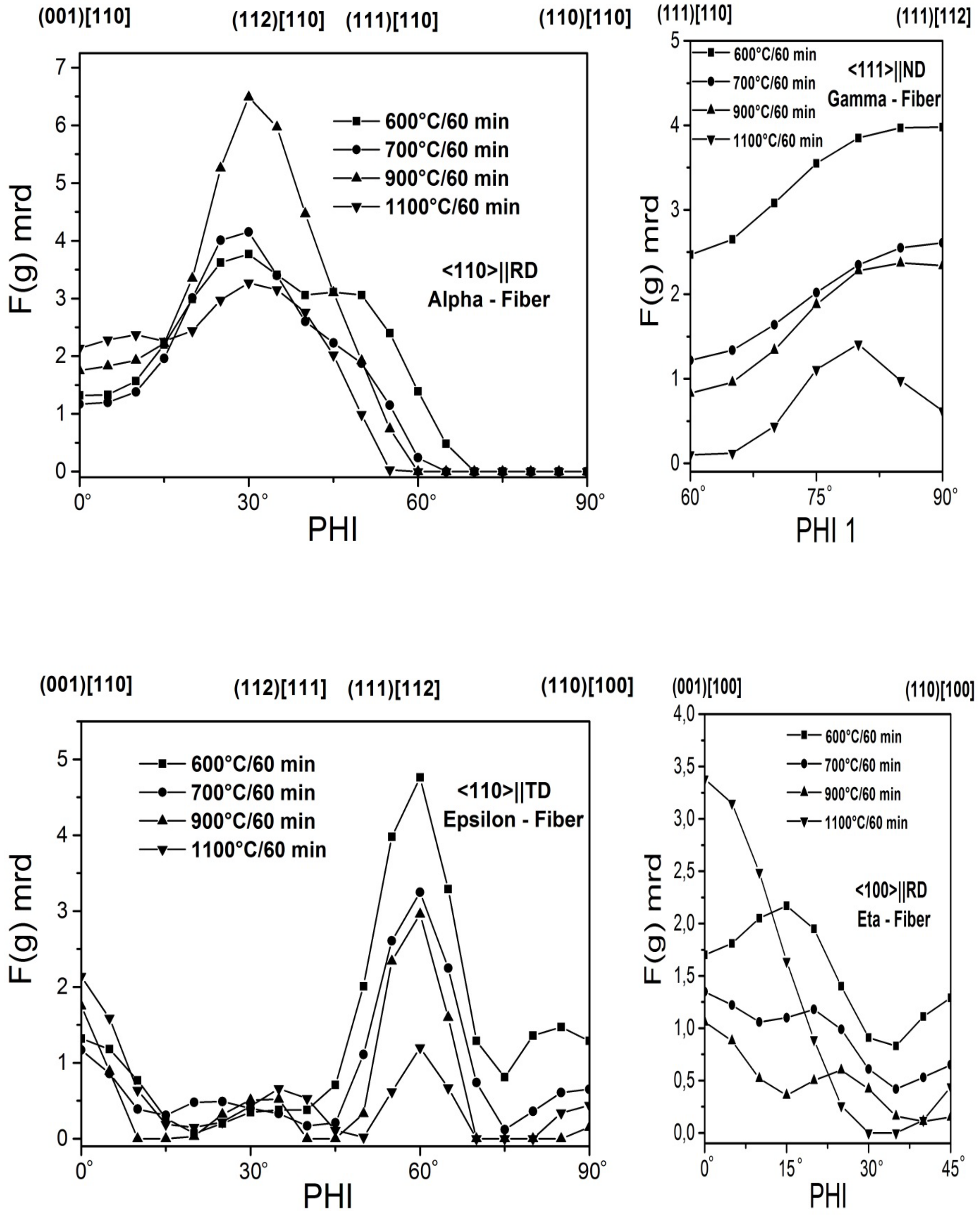

Figure 4.17: The **α, γ,** η and **ε** fibers of 90% cold rolling at annealing at 600°C, 700°C, 900°C and 1100°C for 60 min

4.2.5 Grain Size

Grain size has a great effect on magnetic losses [157-163], which is directly an effect on the performance of electrical machines making the control of grain size to be an important issue when efficiency is required. When the grain size diameter d increases, the hysteresis loss decreases in proportion to 1/d. The total core loss is minimized at an optimum grain diameter in the range of 150 and 200μm [164]. This optimum grain size is obtained after the final annealing. The average grain size at (rolling, transverse and normal) directions were evaluated by line intercept method for 90 % cold rolling plus different annealing temperature and different annealing time as shown in Fig. 4.18

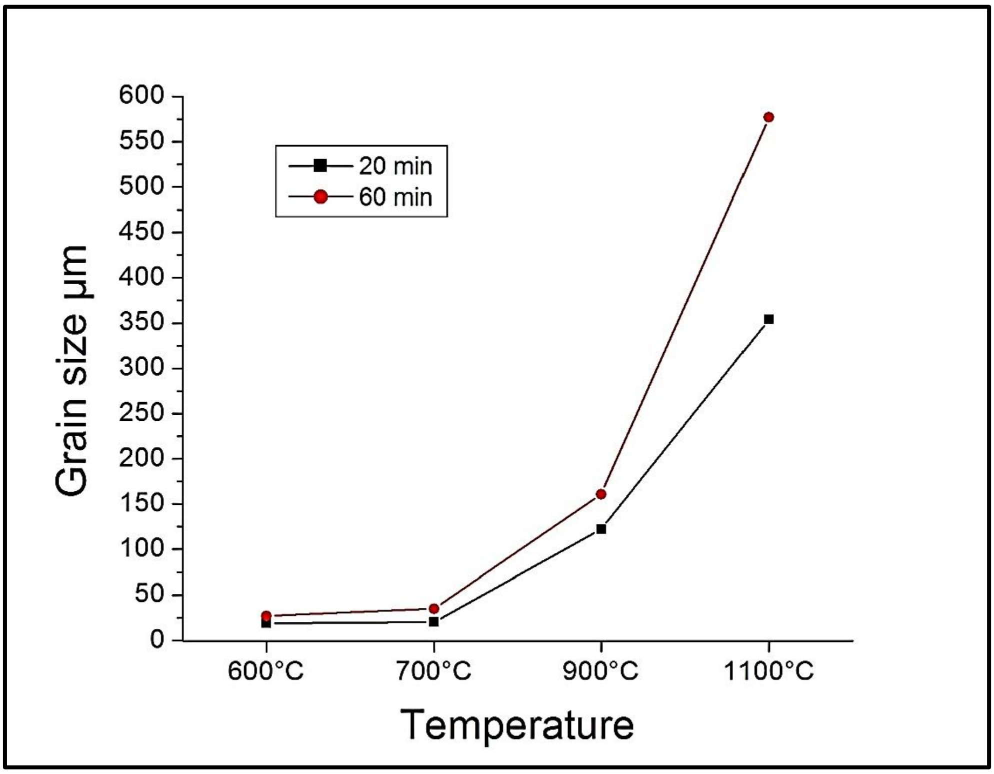

Figure 4.18: The average grain size for 90% cold rolling at different annealing temperatures and annealing times

4.2.6 Two Stages Cold Rolling with Intermediate Annealing

After 75 % cold rolling the type of microstructure in heavily deform material was smooth type [154][155]. The average grain size at (rolling, transverse and normal) directions were evaluated by line intercept method, the type of microstructure after recrystallization at 600°C was equiaxed grains and after 60% second cold rolling the grains elongated toward the rolling direction, the type of microstructure after annealing the sample at 800°C was polygonal shape as shown in Fig. 4.19 from (a-l).

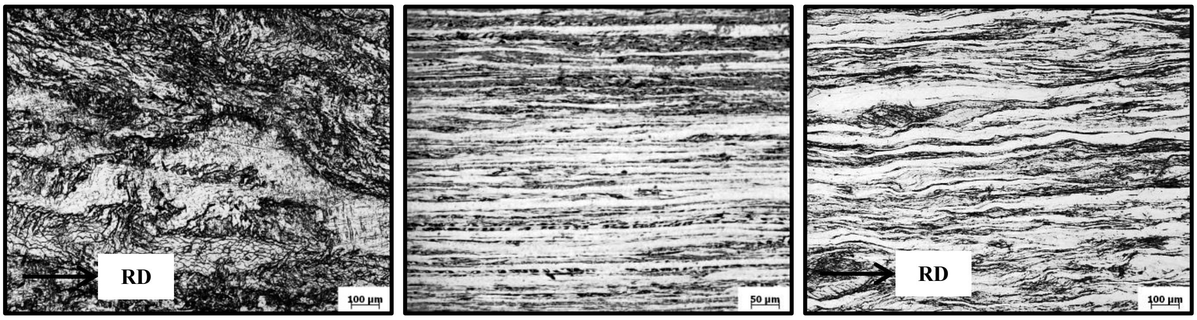

a) 75% cold rolling (RD-TD) **b)** 75% cold rolling (TD-ND) **c)** 75% cold rolling (RD-ND)

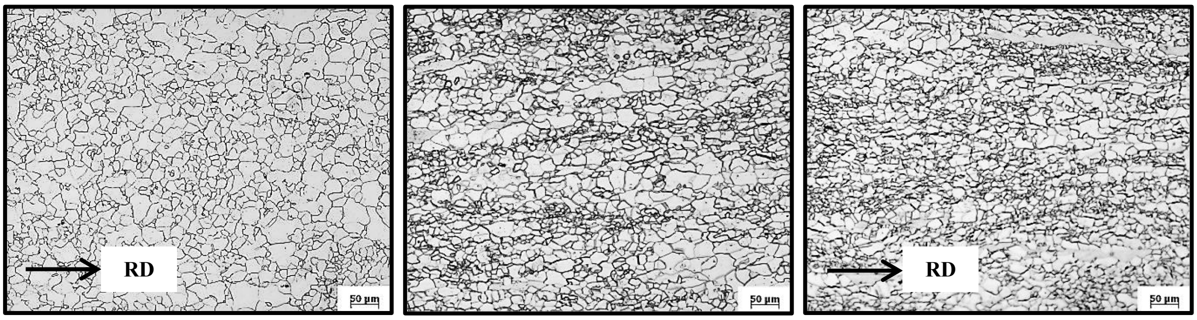

d) 600°C/60 min (RD-TD) **e)** 600°C/60 min (TD-ND) **f)** 600°C/60 min (RD-ND)

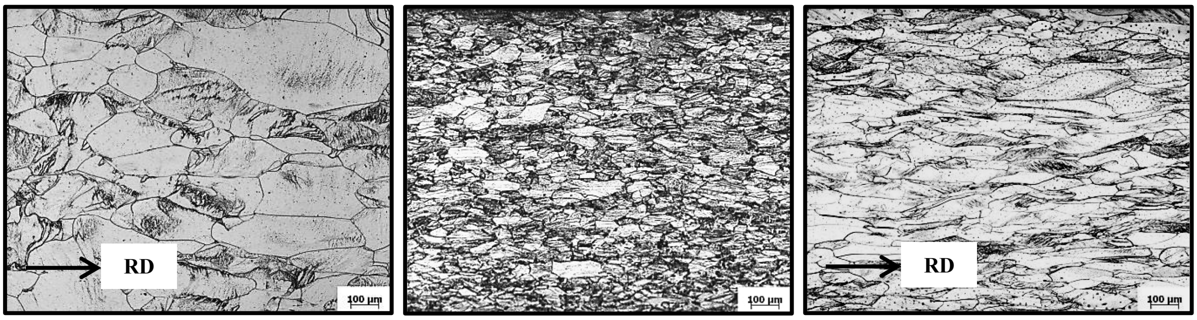

g) 60% cold rolling (RD-TD) **h)** 60% cold rolling (TD-ND) **i)** 60% cold rolling (RD-ND)

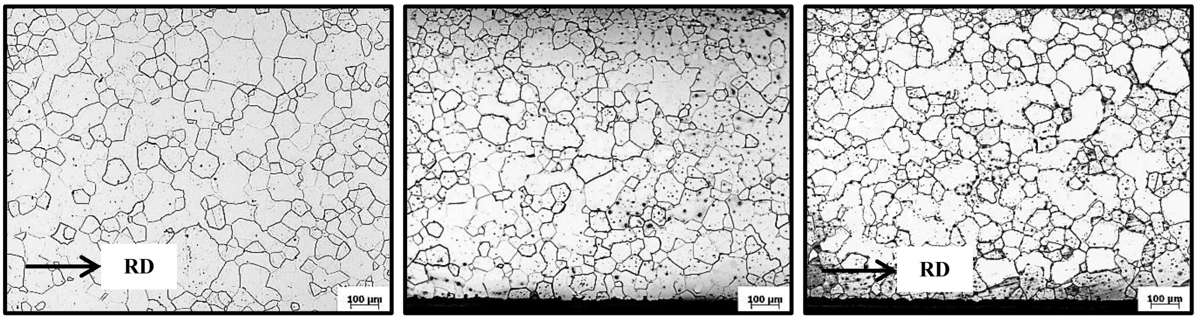

j) 800°C/60 min (RD-TD) **k)** 800°C/60 min (TD-ND) **l)** 800°C/60 min (RD-ND)

Figure 4.19: Optical micrograph of two stages cold rolling the average grain for 600 °C/60 min is 19 µm, 60% cold rolling is 133 µm and for 800 °C/600 min is size 75 µm

The pole figures of 75% cross cold rolling are shown in Fig. 4.20. The crystallographic texture after 75% cross cold rolling was preannounced a strong (001)[110] due to rotate 90° around ND for hot rolled sample before cold rolling caused transfer all <110>||RD fiber to <110>||TD as shown in Fig. 4.24 a, the hot rolling components rotate as expected [159]. However, the intensity spread along α fiber <110>||RD particularly for the rotation cube component (001)[110] was less than after 90% cold rolling [188].

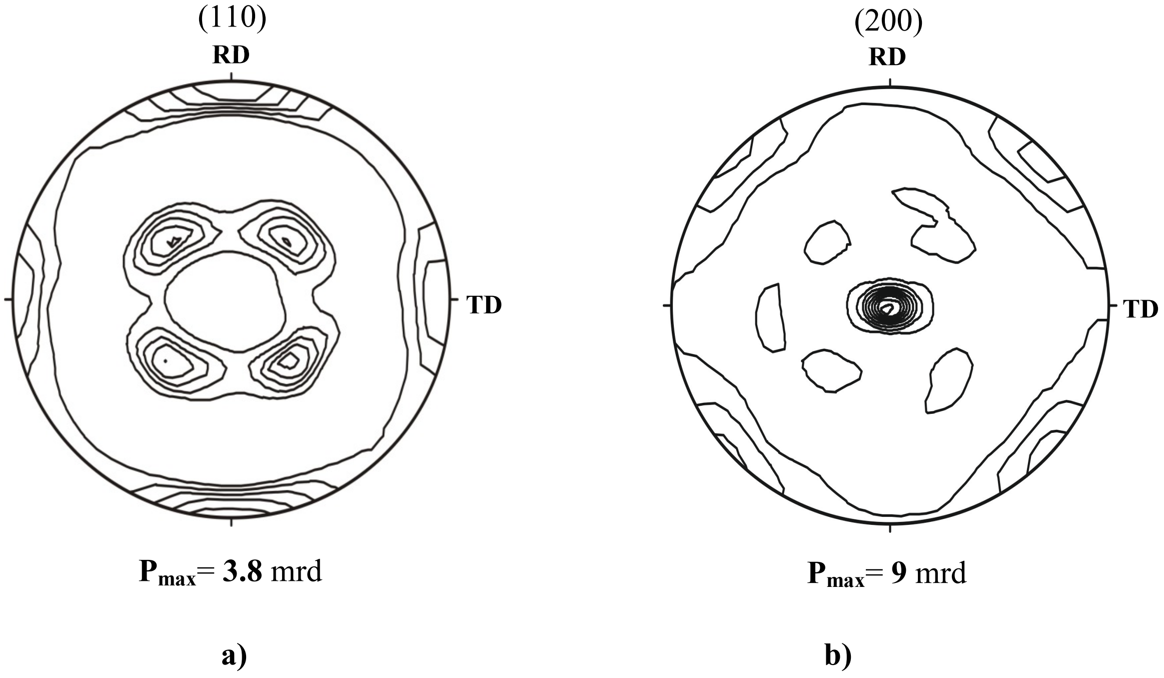

Figure 4.20: a) (110) **b)** (200) pole figure for 75 % cold rolling

Figure 4.21 shows the pole figures after conventional rolling reduction 75% annealed the sample at 600°C/60 min, the results observed decreasing in the α fiber <110>||RD particularly for the rotation cube component {001}<110> and increases the intensity spread along γ fiber (<111>||ND) particularly the two components (111)[110] and (111)[112]. The Goss component {110}<100> slightly increased after primary recrystallization as shown in Fig. 4.24 b [188].

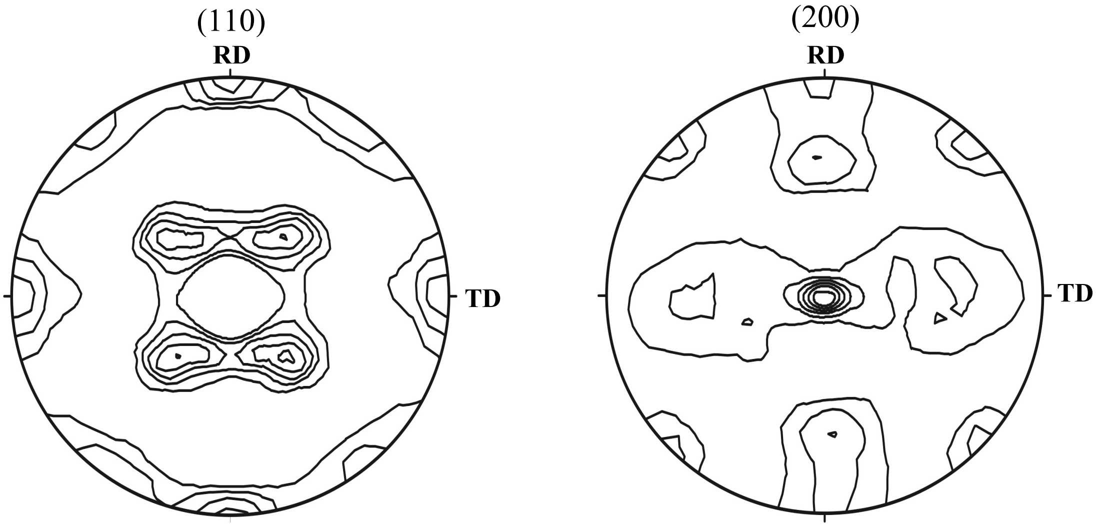

P$_{max}$= 2.3 mrd

P$_{max}$= 3.8 mrd

a)

b)

Figure 4.21: a) (110) **b)** (200) pole figures after 75% cold rolling plus 600°C/60 min

Figure 4.22 shows the pole figures for the second cold rolling 60% reduction, the results observed more homogeneous increasing in the intensity spread along the γ fiber (<111>||ND) particularly the two components (111)[110] and (111)[112] and decreasing the intensity spread along the α fiber (<110>||RD) as shown in Fig. 4.24 c [188].

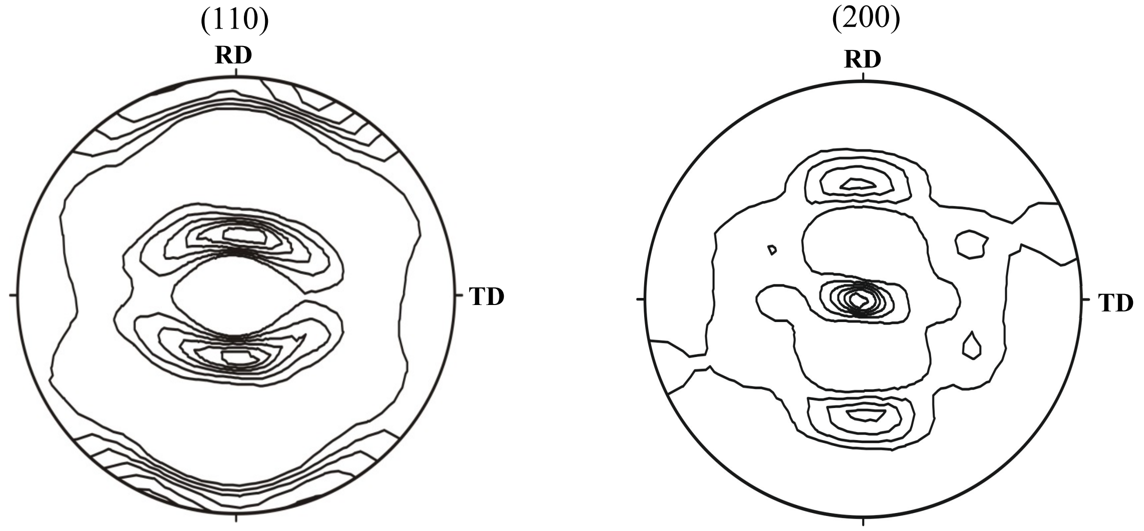

P$_{max}$= 2.8 mrd

P$_{max}$= 3.9 mrd

a)

b)

Figure 4.22: a) (110) **b)** (200) pole figures after 60% cold rolling

Figure 4.23 shows the pole figure after two stages cold rolling with intermediate annealing at 600°C/60 min, annealed the sample at 800°C/60 min the results observed increasing of the intensity spread along the ε fiber (<100>||RD) particularly the tow components the Cube components (001)[100] and the Goss components {110}<100> and more homogeneous intensity spread along γ fiber (<111>||ND) as shown in Fig. 4.24 d [188].

To have still more quantitative information it is useful to plot the orientation densities *f* (g) along the fiber, i. e. as function of the angle of rotation around the fiber axis, as shown in Fig. 4.25 for the α, γ, η and ε fibers. [188]

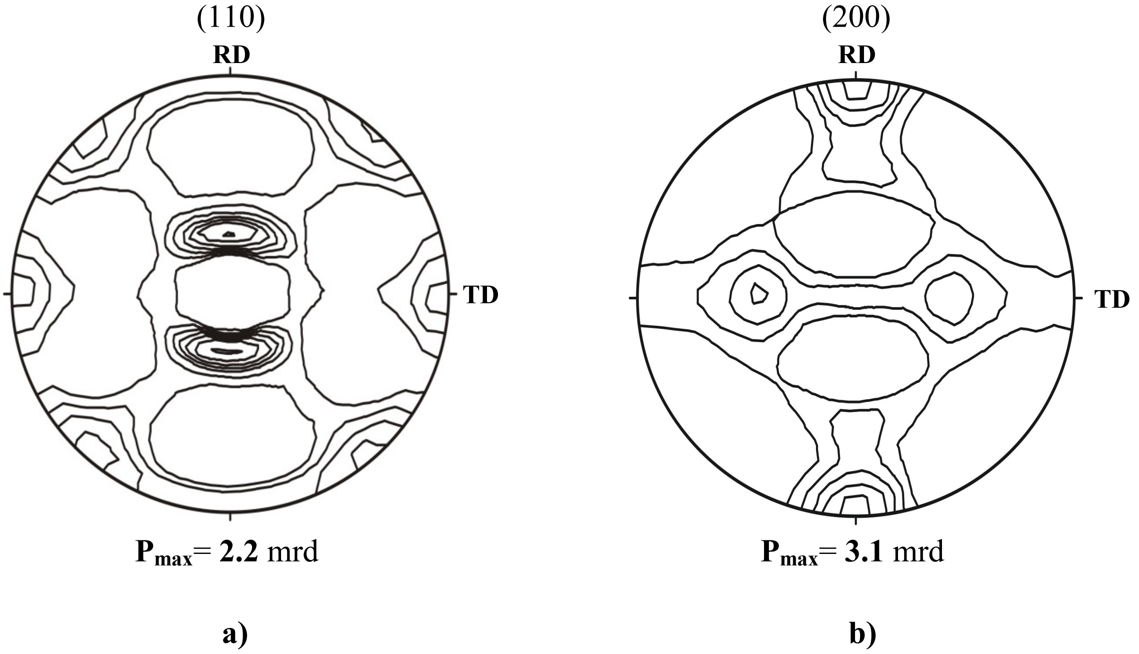

a) **b)**

Figure 4.23: **a)** (110) **b)** (200) pole figures after 60% cold rolling plus 800°C/60 min

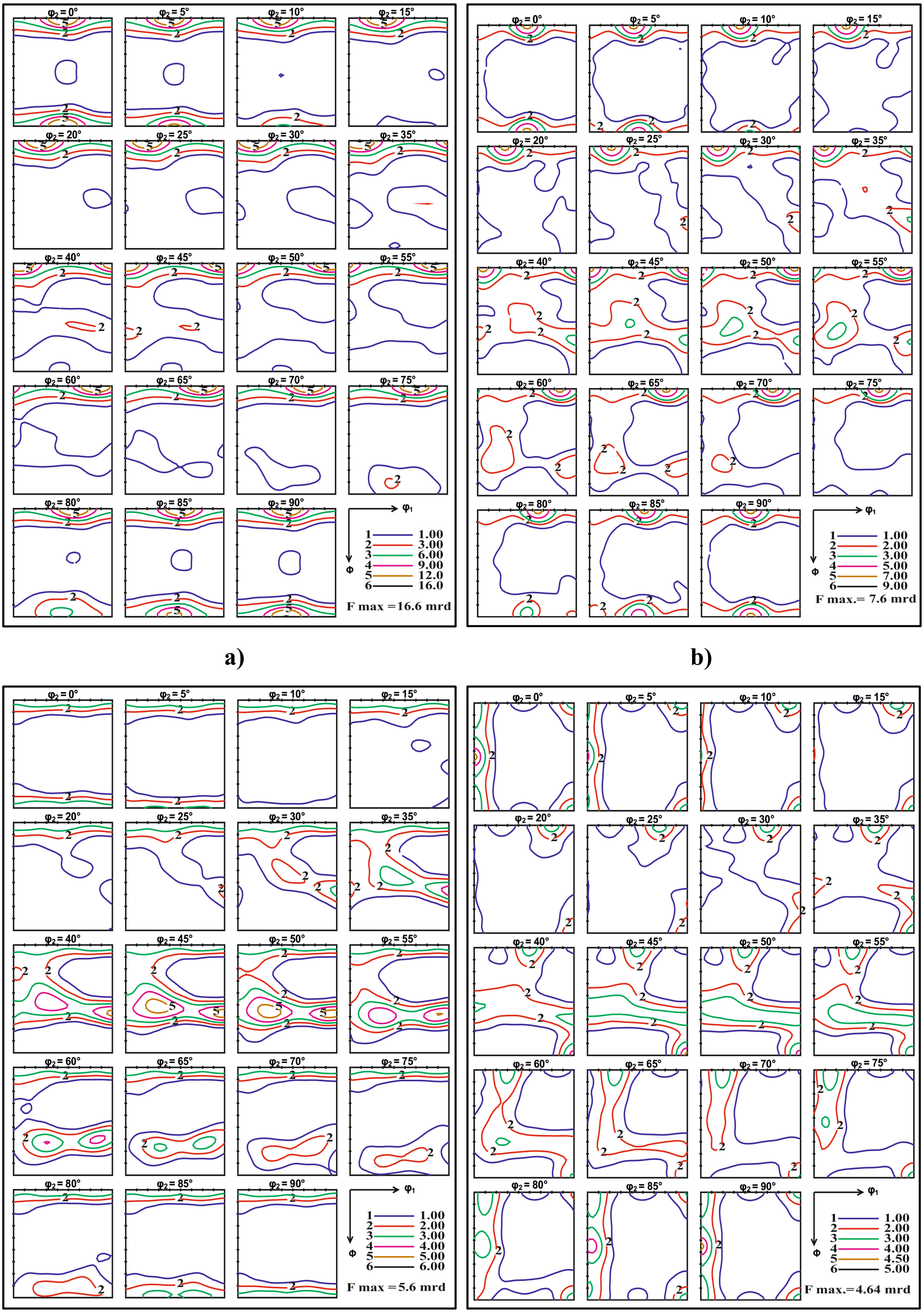

a) b) c) d)

Figure 4.24: ODF sections showing texture for **a)** 75% cold rolling **b)** 75% cold rolling plus 600°C/60 min **c)** 60% cold rolling **d)** 60% cold rolling plus 800°C/60 min

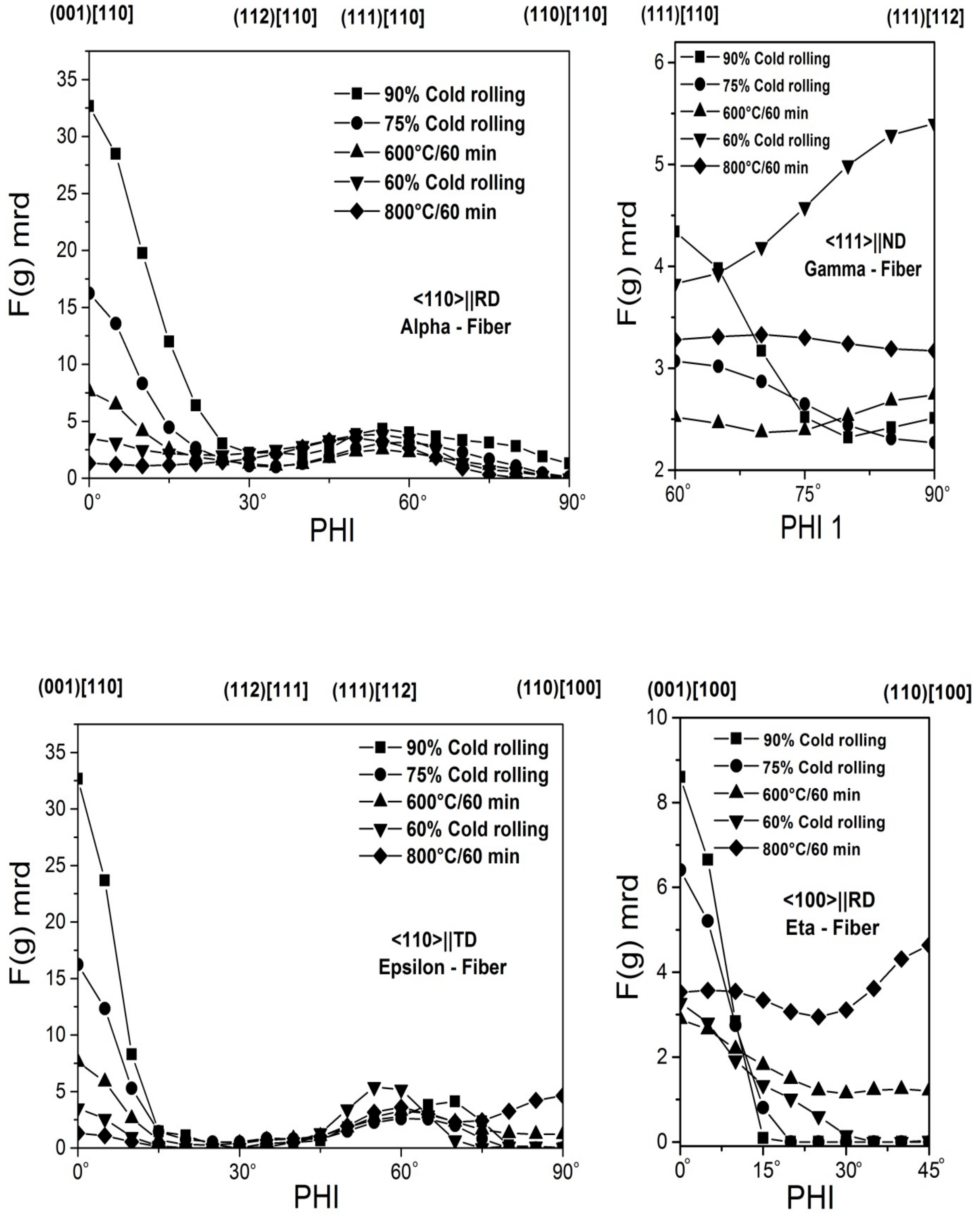

Figure 4.25: The α, γ, η and ε fibers of two stages cold rolling process [188]

4.2.7 Magnetic Annealing at Different External Field (0, 7, 14) Tesla

The variations of crystallographic texture are occurred during the recrystallization annealing. However, it can be easily related to the behavior of the individual microstructural components such as impurities, defect density and dislocation are observed during plastic deformation [168]. The rolling texture of steel is commonly inter preferred in terms of fiber texture [176], the intermediate cold rolling process well developed <111>||ND fiber texture, as an important of external field, it has been evidence experimentally that the magnetic field can be affected after development of recrystallization and crystallographic texture in plastic deformed metallic material [127][128][178-184].

The most significant features of cold-rolling texture in electrical steels are the following: Firstly, a development of a strong complete fiber near <111>||ND and of a partial fiber along <110>||RD. Secondly, the energy storage during deformation is orientation dependent and increasing in the sequence <100>, <112>, <111> and <110> orientations. The stored energy of <110> orientation is increase continuously with increases the deformation reduction [169]. An example, when the bcc single crystal iron is magnetized to saturation, therefore the energy of the crystalline structure is improved by the amount of the magnetic free energy which depends on the relation of the grain orientation with respect to the magnetic field direction. The magnetic energy of the crystalline structure is being the lowest in the <100> direction and the highest in the <111> direction and medial in the <110> direction parallel to the magnetic field direction [185]. The energy of the grains with <100> orientation parallel to the magnetic field is the lowest and they have the largest driving force for recrystallization, then the <110> oriented grains and the <111> oriented grain. The angle between <111> direction and nearest <100> direction is about 54.7° and the angle between <110> and <100> is 45°. Hence, it is possible that the magnetic free energy of the texture increases according to the angle between the crystallographic direction and the nearest <100> direction.

After two stages cold rolling (at 75% and 60% reduction) with intermediate annealing process the samples was annealed at 600°C/60 min at different external field 0, 7 and 14 Tesla. The results pronounced variance on the type of the microstructure caused by the effect of the external field on the grain orientation. The results observed after annealing the sample at 600°C during external field at (μH= 0 and 7) Tesla equiaxed grains. Also, the results observed elongation on the grain toward the direction of the external field at μH= 14 Tesla. Figure 4.26 from (a to i) shows the microstructure of Fe2.6 % Si after magnetic annealing process.

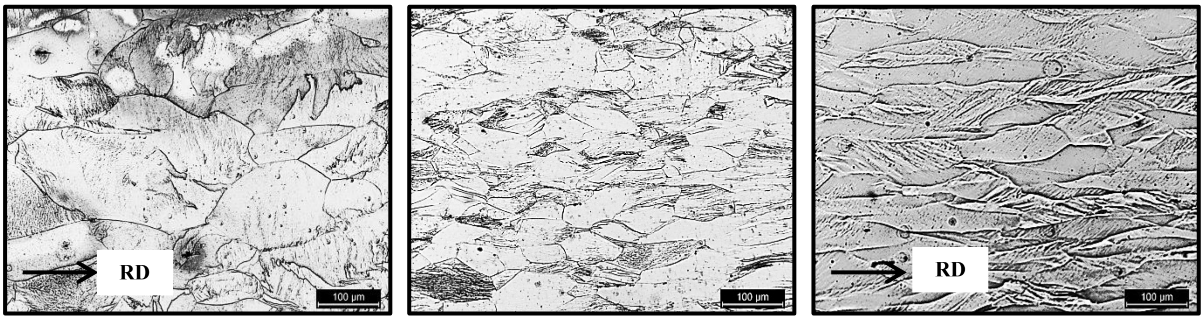

a) Annealing at 0T (RD-TD) **b)** Annealing at 0T (TD-ND) **c)** Annealing at 0T (RD-ND)

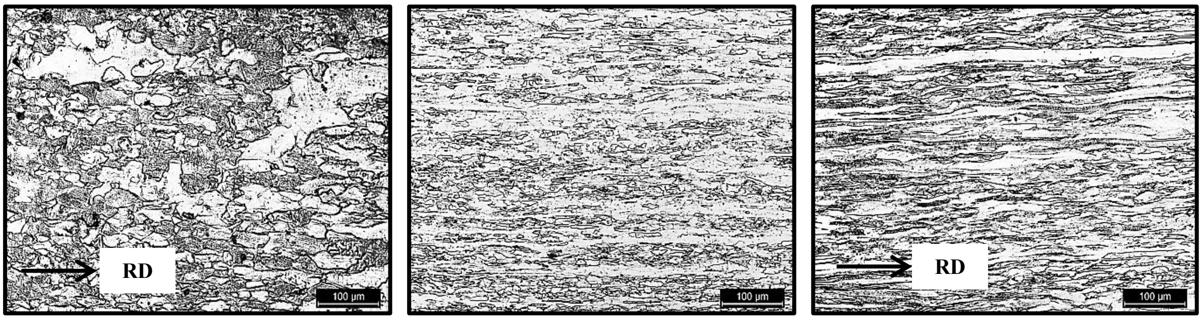

d) Annealing at 7T (RD-TD) **e)** Annealing at 7T (TD-ND) **f)** Annealing at 7T (RD-ND)

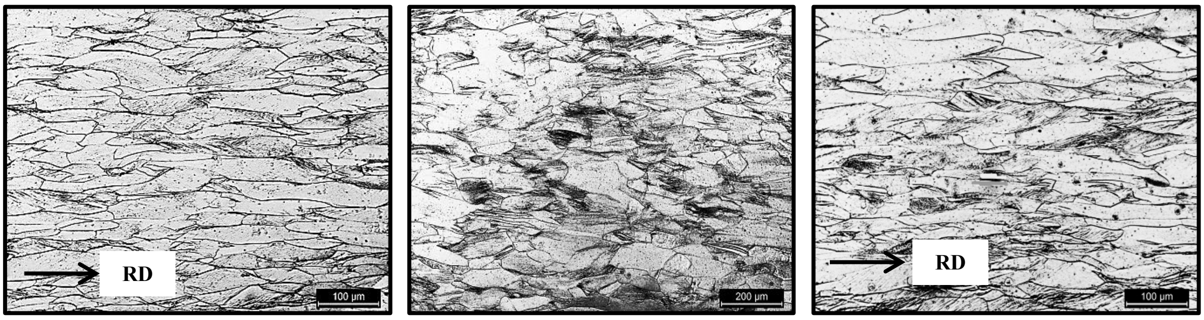

g) Annealing at14T (RD-TD) **h)** Annealing at 14T (TD-ND) **i)** Annealing at 14T (RD-ND)

Figure 4.26: Optical micrograph after two stages cold rolling annealed at 600°C/60 min with different external field at 0, 7 and 14 Tesla

Figure 4.27 shows the pole figure evolution after annealing the samples at 600°C/60min with zero Tesla external field, the result observed increasing of the intensity spread along θ fiber <001>||ND between (001)[1-10] rotated cube component to the cube component (001)[0-10] and to (001)[-1-10] rotated cube as shown in Fig. 4.30a, particularly increasing at the Euler angles of the orientation (φ_1 ,Φ, φ_2) ≈ [11, 0, 45] is observed. These angles correspond approximately to the (001)[-2 -3 0] set of Miller indices [47]. Also, the results observed at Zero Tesla a homogeneous intensity spread along γ fiber (<111>||ND), and the (114)[1-10] crystallographic texture component is appeared.

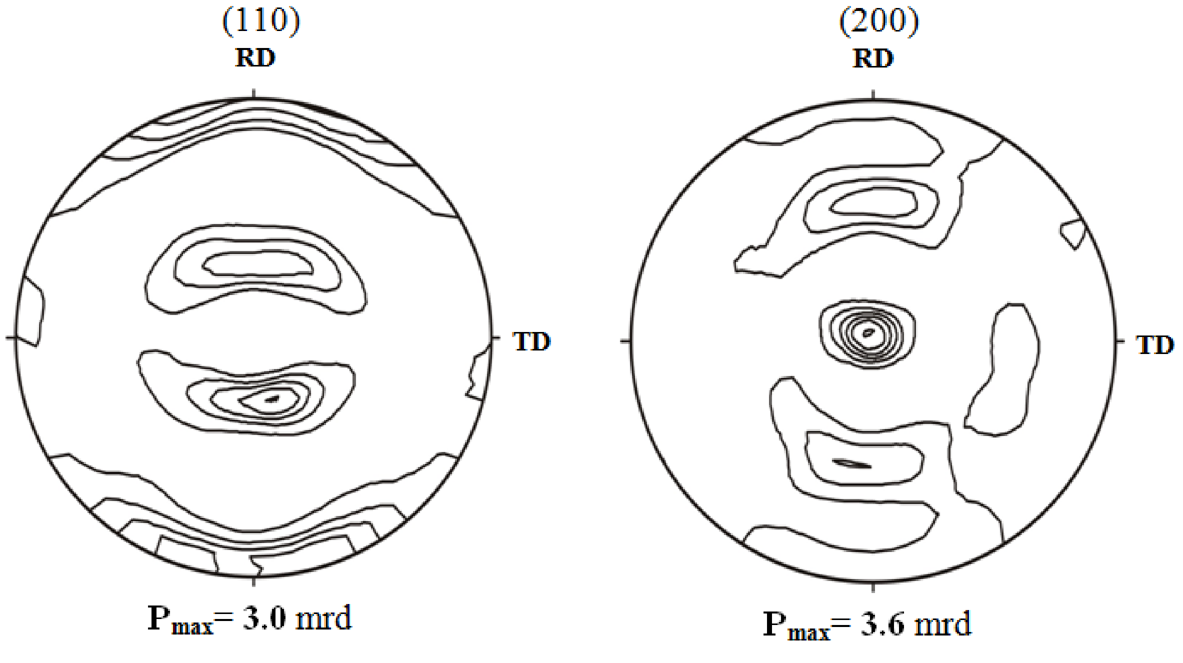

a) **b)**

Figure 4.27: **a)** (110) **b)** (200) pole figure for Fe-2.6%Si after 60% cold rolling and subsequent magnetic annealing at 600°C in $\mu_o H = 0$ Tesla

Figure 4.28 shows the pole figure after annealing the samples at 600°C/60 min at 7 Tesla external field, the result pronounced at 7 Tesla increasing of the intensity spread along the θ fiber <001>||ND as shown in Fig. 4.30b, particularly increases the intensity of (001)[1-10] rotated cube component and more homogeneous intensity spread along the γ fiber (<111>||ND) are observed, particularly at (111)[121] and (111)[112] crystallographic texture components.

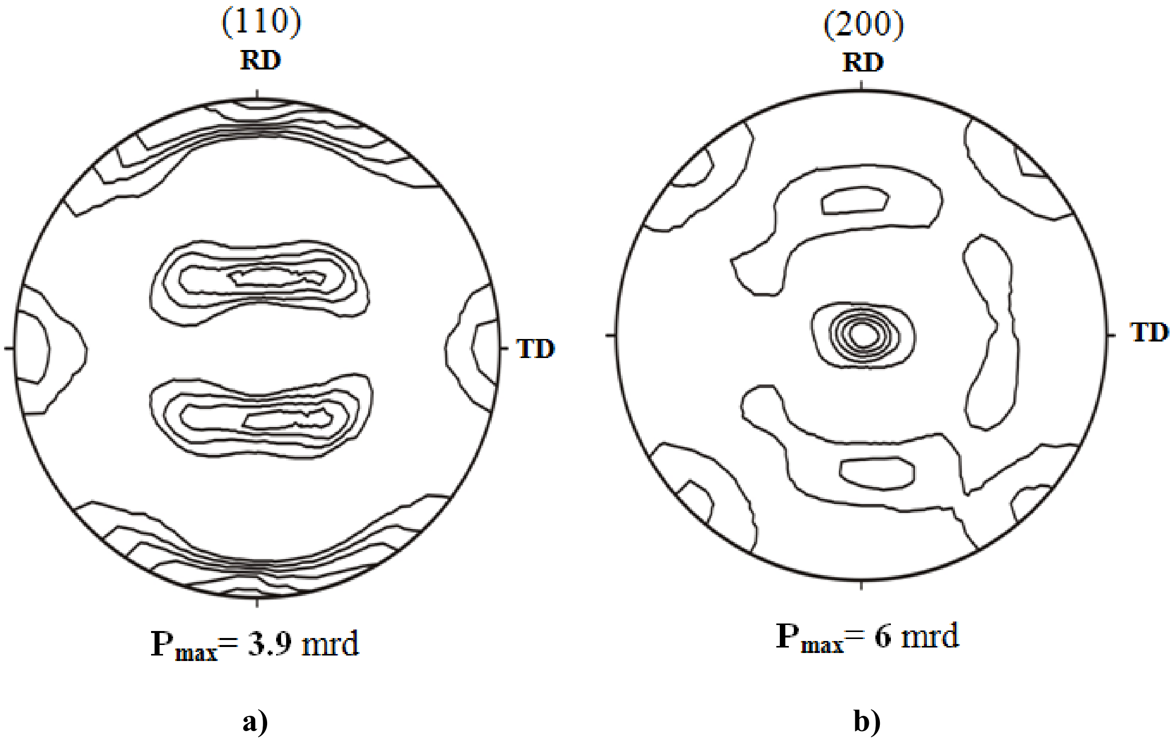

a) **b)**

Figure 4.28: **a)** (110) **b)** (200) pole figure for Fe-2.6%Si after 60% cold rolling and subsequent magnetic annealing at 600°C in $\mu_o H$ = 7 Tesla

Figure 4.29 shows the pole figure after annealing the samples at 600°C/60 min at 14 Tesla, the result observed at 14 Tesla as shown in Fig. 30c increasing of the intensity spread along θ fiber <001>||ND between (001)[1-10] rotated cube component to the cube component (001)[0-10] and to (001)[-1-10] rotated cube. Particularly, slightly an increasing at the Euler angles of the orientation (φ_1, Φ, φ_2) ≈ [11, 0, 45] is observed. These angles correspond approximately to the (001)[-2 -3 0] set of Miller indices [47] and more homogeneous intensity spread along the γ fiber (<111>||ND) more than at 0 tesla, particularly at two crystallographic texture components (111)[121] and (111)[112] are observed.

A more detailed overview of the angle-dependent intensity spreads for the three magnetic fields used in this investigation is given in figure Fig. 4.31 where beside the α fiber and the γ fiber also the η, θ fibers and the ε fibers.

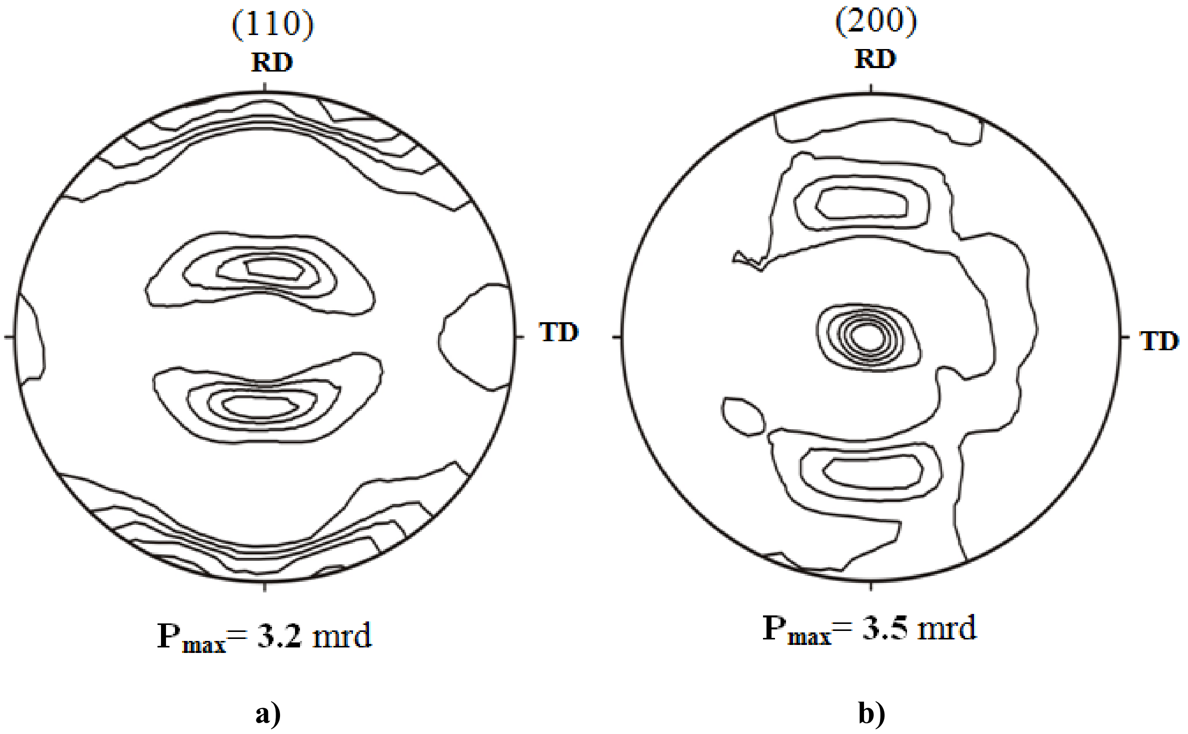

Figure 4.29: **a)** (110) **b)** (200) pole figure for Fe-2.6%Si after 60% cold rolling and subsequent magnetic annealing at 600°C in $\mu_o H = 14$ Tesla

The results observed that the low magnetic field at 7 Tesla increases the crystallographic texture components at the <110> direction. Obviously the free energy of grains with <100> orientation parallel to the magnetic field is lowest and they have the largest driving force for recrystallization, then the <110> oriented grains and the <111> oriented grains, while for Fe-2.6%Si at 7 Tesla more intensity spread along θ and γ fiber, which suggests that nucleation of grains with <110> orientation because the must preferred orientation during magnetic annealing at 7 Tesla. The angle between <100> direction and <112> direction about 35.3°, therefore when increasing the magnetic field at 14 Tesla at the initial stage of recrystallization the <112> oriented nuclei are consider to be favored orientation at high external field at 14 Tesla, which make the nucleation and growth of <112> oriented nuclei in field specimen become easier and homogeneous grains distribution along the rolling direction than at the non-field annealed the specimens.

Besides, the selected the annealing temperature of 600°C it is the recrystallization temperature and lies within the ferromagnetic temperature range closely from Curie temperature point, which might make the preferred orientation mechanism induced by magnetic free energy anisotropy play an important role in recrystallization nucleation.

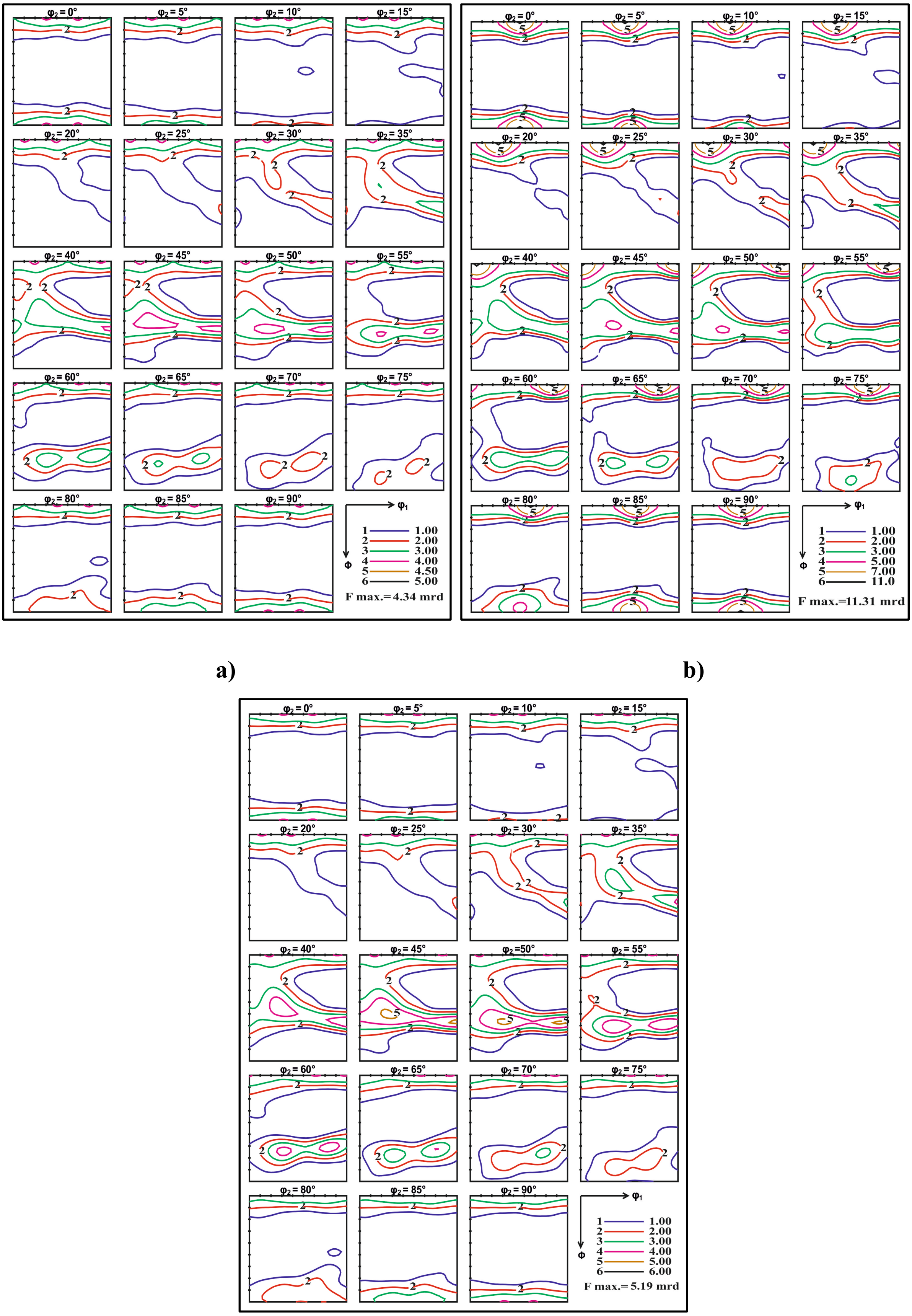

a) b)

c)

Figure 4.30: ODF sections showing texture after two stages cold rolling annealing at 600°C/60min at different external field at **a)** 0 Tesla **b)** 7 Tesla **c)** 14 Tesla

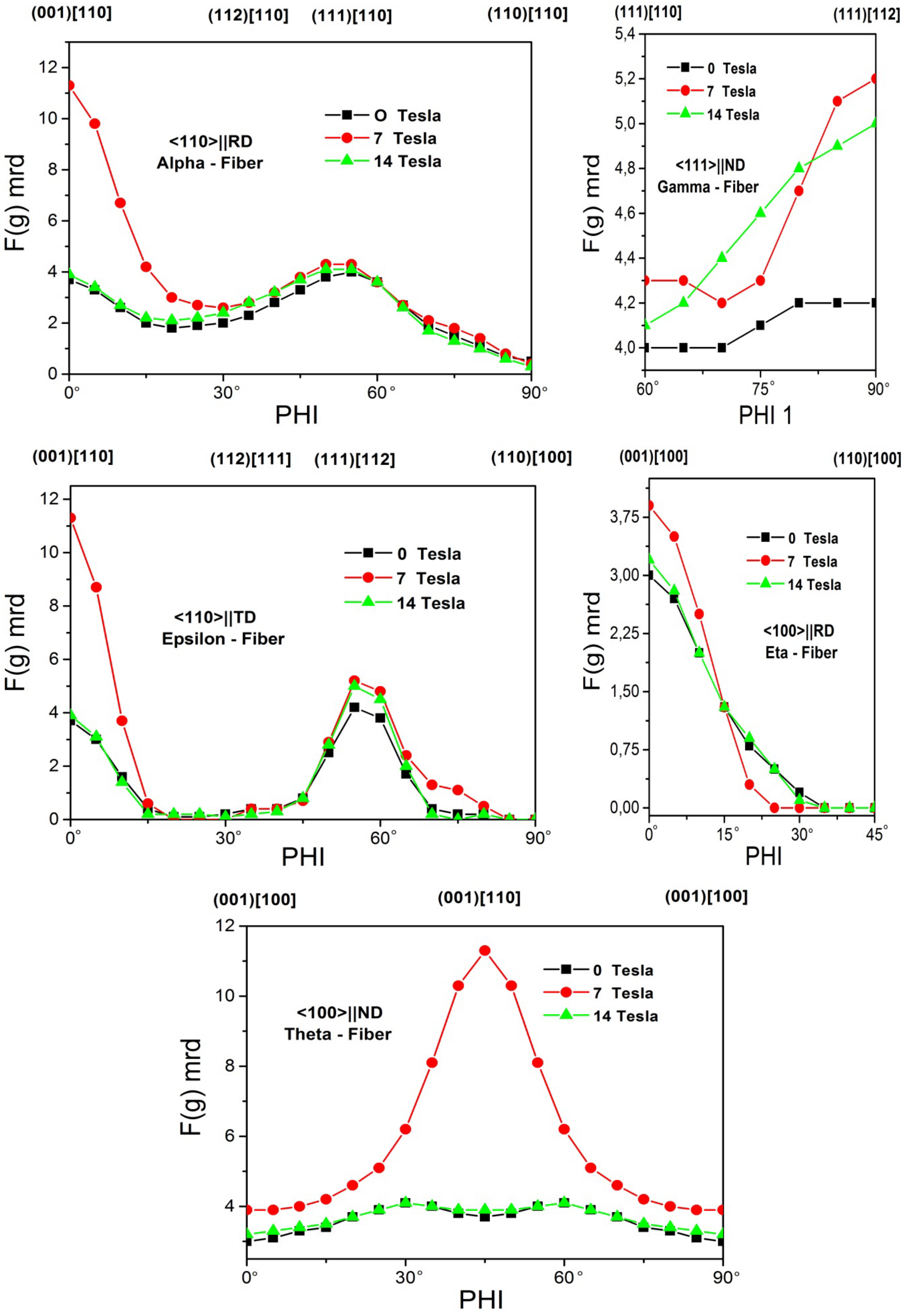

Figure 4.31: The neutron-scattering intensity spreads along the α, γ, η, ε and θ fibers of Fe-2.6%Si for the magnetic fields used during the magnetic annealing process

4.3 Dislocation Density

During cold rolling and annealing, crystallographic texture and microstructure will change heavily. The influence of thermo-mechanical treatment on the defect evolutions is the main goal. For Fe2.6%Si steels grain size is normally large enough to have no domain size line broadening effect. That means, line broadening consists only on the instrumental line broadening and microstrain line broadening related to dislocations, stacking faults and so on. Typical diffraction investigations of microstructures take only a selected number of grains into account well oriented to the Bragg's conditions.

The FWHM values were plotted against the Bragg angle of the reflection in Fig. 4.32 at transverse direction (TD) and Fig. 4.33 at rolling direction (RD).

The standard sample shows no slope as well as the steel sample with final annealing, which means both are free of microstrain. The difference in line broadening between this two strain free samples is due to the sample thickness.

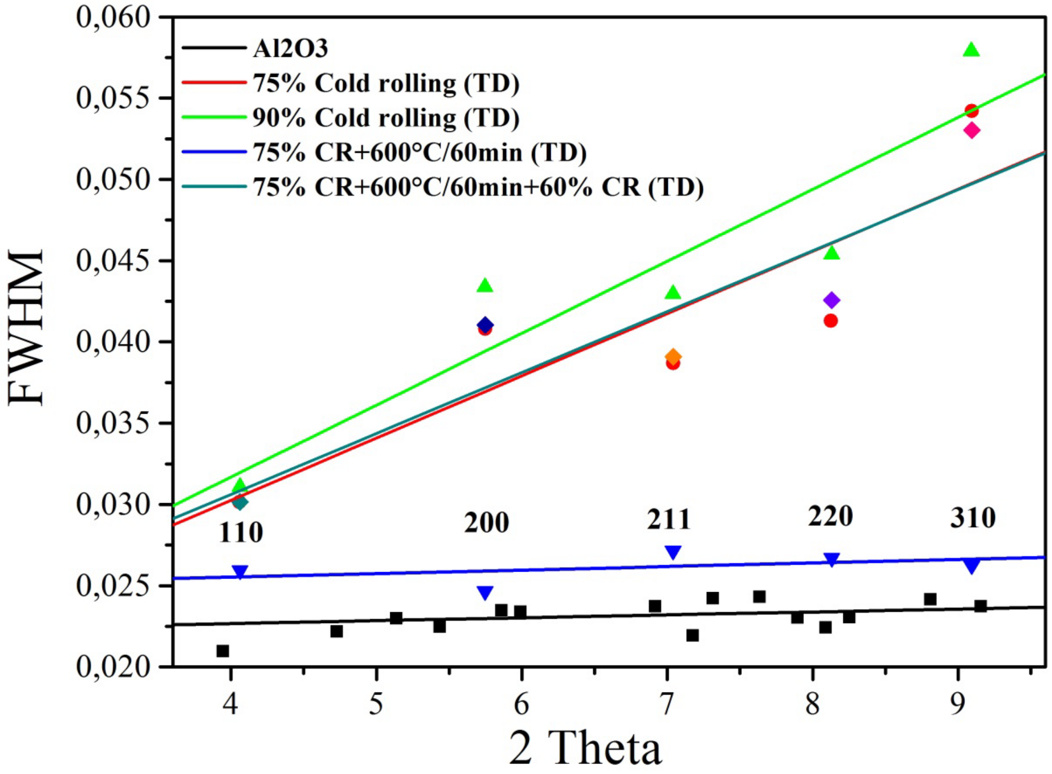

Figure 4.32: FWHM for all reflections at transverse direction (TD)

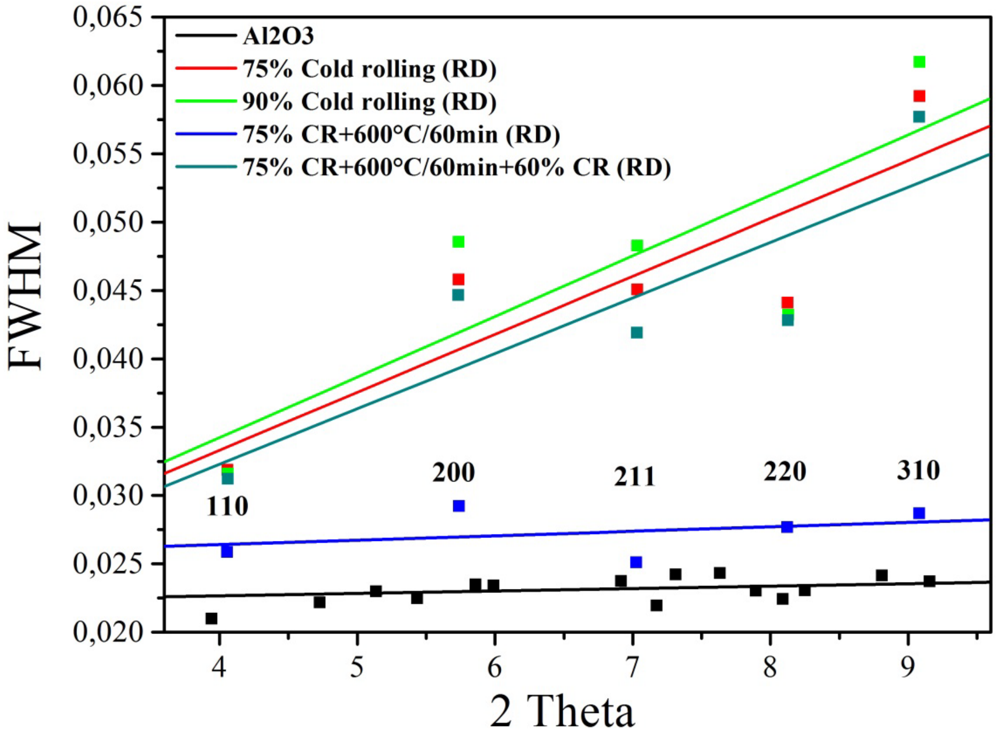

Figure 4.33: FWHM for all reflections at rolling direction (RD)

Using the modified Williams and Hall plot [170], the defect densities at transvers and rolling direction respectively has been calculated after subtraction the thickness effect and instrumental function on the peak Broadening using NIST Al2O3 plate. The elastic constant of Fe 2.6% Si (C_{11} = 277.1, C_{12} = 130.25 and C_{44} = 110.61) GPa [171], the value of $\underline{C_{h0.0}}$ can be obtain from the Aniz C program [172] for the calculation of diffraction contrast factors of dislocations in elastically anisotropic cubic and hexagonal polycrystalline material, where is assumed that edge and screw dislocations are present in equal proportion.

Figure 4.34 shows the modified Williamson-Hall plots for Fe-2.6%Si after (75% cold rolling, 90% cold rolling and after two stage cold rolling (at 60% reduction) with intermediate annealing process at 600°C/60 min) from this figure , one can see that the slop of Williamson-Hall plot increases with increasing the deformation reduction, which means rising dislocation density.

The defect density has been calculated at transvers and rolling direction respectively to ($2.5\text{x}10^{14}$ m^{-2} and $2.9\text{x}10^{14}$ m^{-2}) for 75% cold rolling, to ($3.04\text{x}10^{14}$ $m^{-2}$and 3.08 $\text{x}10^{14}$ m^{-2}) for 90% cold rolling, and to ($2.38\text{x}10^{14}$ m^{-2} and $2.8\text{x}10^{14}$ m^{-2}) for the sample with intermediate annealing.

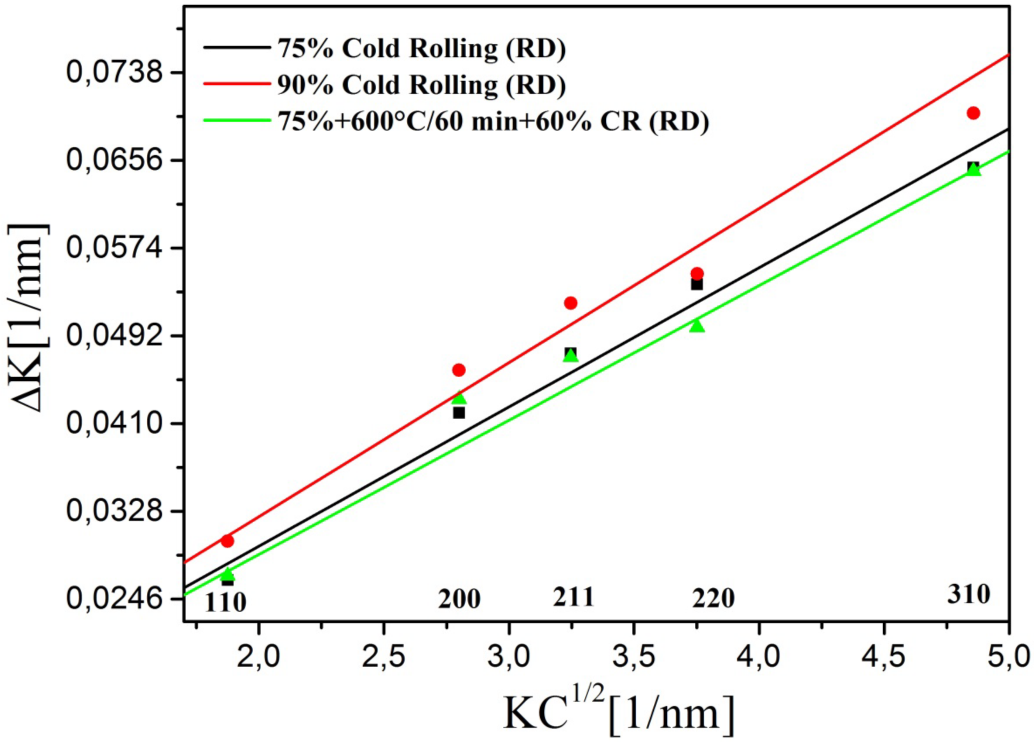

Figure 4.34: Modified Williamson-Hall plot

TEM Images of Fe-2.6% Si were recorded from samples after 97% hot-rolling, 75% cold-rolling and 60% cold rolling after an intermediate annealing process, respectively. The micrographs are shown in Fig. 4.35. It is obvious that the dislocation density is significantly lower in the hot rolled sample (Fig. 4.35 a) and the dislocation structure mainly consists of long straight dislocation segments. When comparing this hot rolled state with the different cold rolled states a significant increase in dislocation density can be observed. This is especially true for the two cold rolled specimen states without intermediate annealing (Fig. 4.35 b and c). In these two specimens heavily entangled dislocations are observed which are spaced that closely that single dislocations cannot always be resolved. However, qualitatively the dislocation density appears to increase with deformation when comparing the 75 % and 90 % cold rolled samples. It has to be remarked that dislocations in regions which appear to be dislocation free in these two specimens are out of contrast due to local bending of the heavily deformed specimens which was confirmed by tilting. The intermediate annealing alters the dislocation structure further. While still areas with very high dislocation density are present these are arranged in a kind of wall structure with regions of significantly lower dislocation density in between. In contrast to the two cold rolled specimens it could be confirmed by tilting that this really resulted from a lower dislocation density and not from dislocations locally out of contrast. One can conclude from the TEM investigations that the defect density and arrangement in the specimens is predominantly determined by the cold rolling steps. Even the regions with relatively low dislocation density in the sample which experienced intermediate annealing do not reassemble the appearance of the dislocation structure in the hot rolled sample.

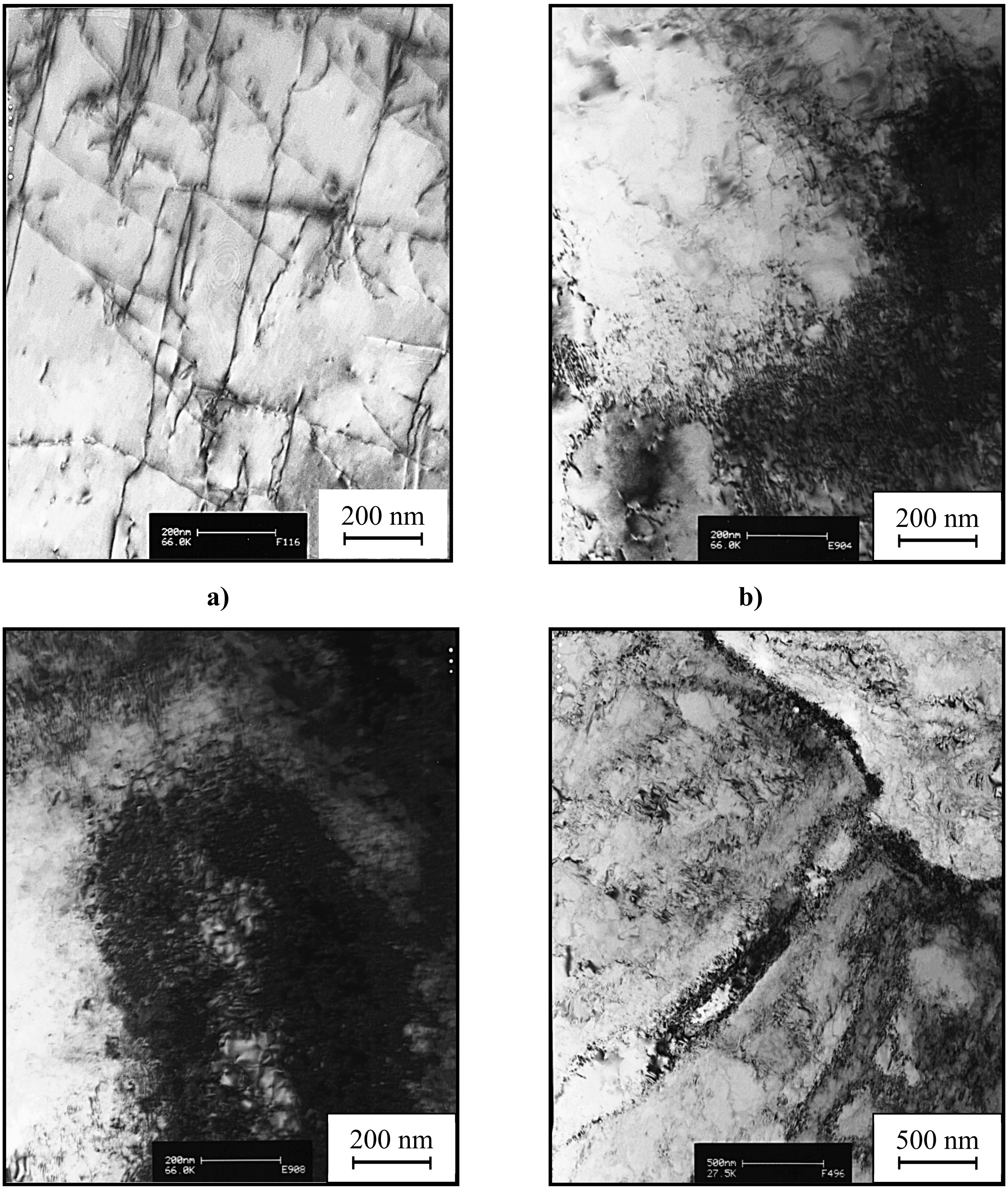

a) b) c) d)

Figure 4.35: TEM images of Fe-2.6% Si for **a)** 97% hot rolling **b)** 75% cold rolling **c)** 90% cold rolling **d)** 60% cold rolling with intermediate annealing process

4.4 Magnetic Properties

The measurement of magnetic properties of Fe 2.6%Si samples shows variation on magnetic characteristics values at rolling direction (RD) and transverse direction (TD). Due to the effect of crystallographic texture, grain size, misorientation of the grain boundaries, domains structures, movement of domain boundaries and the impurities such as dislocation, grain boundary and precipitation are affected the magnetic properties at rolling and transverse direction.

The magnetic properties of Fe 2.6% Si samples were measured at magnetizing frequencies of 10Hz and 50Hz and a maximum polarization of J_0=1.8T and the samples at transvers direction (TD) measured at a magnetizing frequency of 10Hz maximum polarization of J_0=1.6 Tesla. The saturation polarization was estimated to be J_s=2.04T which corresponds to the values found in literature for Fe 2.6% Si [2].

As can be seen in all tables below the power losses are increased with frequency. This is due to an increase of classical and anomalous losses which are frequency dependent [2][16].

Related to eddy currents in the sample the permeability is slightly decreased. Permeability values measured in rolling direction of the as-received samples are nearly twice of the values measured in transversal direction as shown in table 4.1. This indicates anisotropy of the grains oriented with magnetics easy axis in rolling direction.

Astonishingly the cold rolling process changes the permeability to higher values and simultaneously the power losses and coercive forces to lower values as shown in table 4.1. Usually the rolling process should induce so many dislocations that the permeability is decreased and coercive forces and power losses are increased. This is not the case and therefore can be assumed that the dislocation density in the as-received material is of similar height as in the material after the cold rolling process. Furthermore, these results leads to the assumption that the cold rolling process after the first hot rolling process leads already to a preferred crystallographic orientation of the grains resulting in better magnetic properties. This effect is higher for the 75% cold rolled materials than for the 90% cold rolled alloys [177].

Table 4.1: The magnetic properties measured for as-received material, 75% and 90% cold rolled.

	Permeability		Power loss kJ/m^3		Coercive force A/m	
	10Hz	50Hz	10Hz	50Hz	10Hz	50Hz
As-received (RD)	76	74	3.10	11.76	435	1757
As-received (TD)	47	46	1.30	2.423	156	386
75 % Cold Rolling (RD)	92	93	2.82	3.62	323	526
75 % Cold Rolling (TD)	73		2.71		541	
90 % Cold Rolling (RD)	77	76	3.10	4.22	420	640
90 % Cold Rolling (TD)	78		3.20		656	

The values of magnetic properties were measured at rolling and transvers direction for one stage cold rolling plus different annealing temperatures for 20 min as shown in table 4.2. The results observed changes of the magnetic properties values (see table 4.2). This indicates anisotropy of the grains oriented with magnetics easy axis in rolling direction and the effect of domains structure and domain boundaries on magnetic properties.

The results observed as shown in table 4.2 the thermal treatment of 20 min at 900°C seems to leads to an optimum in magnetic properties in the investigated range. According to Fig. 20 the mean grain size in such samples is around 122µm. A further increase of the grain sizes by higher annealing temperatures does not lead to lower coercive force or power loss and higher permeability values although the number of imperfections in the material is reduced. This behavior is well known as the so called Brown's paradoxon [175].

Related to the change of the texture an effect on magnetic materials properties can be seen in Fig. 4.36 showing the dependence of the texture components developed after recrystallization and grain growth on the permeability and power loss. It can be seen that the permeability increases with increasing annealing temperature due to an increase of texture components (112)[7 -11 2] while the power loss decreases with increasing the annealing temperature up to 900°C. Exceeding this annealing temperature (up to 1100°C) causes a rise in the power loss in spite of the improvement of the texture. However, as it is already mentioned, the power losses are connected with the number of active domain walls, which is dependent on impurities and crystal defects. Impurities like dislocations and grain boundaries are sources for magnetic stray fields. The energy stored in these magnetic stray fields can be reduced by the nucleation of domain walls. The higher number of magnetic domain walls leads to a reduction of power loss during magnetization reversal [174]. Additional, the determinative effect of thermal stresses by rapid heating to high temperatures on the magnetic properties of fully processed electrical steels when further grain growth does not lead to improvement of the magnetic properties was shown in [27]. With decreasing power loss the permeability is increased for annealing temperatures up to 900°C according to the texture generation.

Table 4.2: The magnetic properties measured for 90% cold rolled plus different temperatures for 20 min.

	Permeability		Power loss kJ/m^3		Coercive force A/m	
	10Hz	50Hz	10Hz	50Hz	10Hz	50Hz
Annealing at 600°C (RD)	89	89	1.31	2.39	148	366
Annealing at 600°C (TD)	84		0.93		133	
Annealing at 700°C (RD)	105	101	1.02	2.02	142	328
Annealing at 700°C (TD)	68		0.84		119	
Annealing at 900°C (RD)	112	112	0.74	1.43	101	269
Annealing at 900°C (TD)	45		0.64		103	
Annealing at 1100°C (RD)	49	49	0.98	2.70	113	401
Annealing at 1100°C (TD)	52		0.73		99	

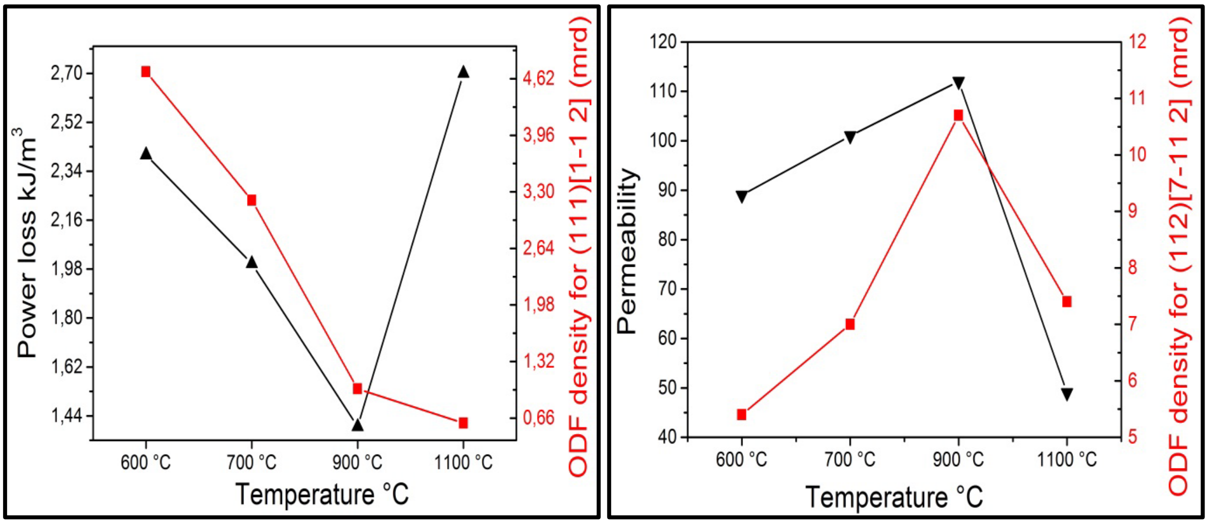

a) **b)**

Figure 4.36: The effect of two components a) (111)[1-1 2] , and b) (112)[7 -11 2] on the magnetic properties for 90% cold rolling plus different temperatures for 20 min

The values of magnetic properties were measured at rolling and transvers direction for one stage cold rolling plus different annealing temperatures for 60 min as shown in table 4.3. The results observed changes of the magnetic properties values (see table 4.3). This indicates anisotropy of the grains oriented with magnetics easy axis in rolling direction and the effect of domains structure and domain boundaries on magnetic properties.

Regarding to the values is shown in table 4.3 for different annealing temperatures for 60 min, the results observed the thermal treatment of 1 hour at 700°C seems to lead to an optimum in magnetic properties. According to Fig. 4.20 the mean grain size in such samples is around 35µm. A further increase of the grain sizes by higher annealing temperatures does not lead to lower coercive force or power loss and higher permeability values although the number of imperfections in the material is reduced. This behavior is well known as the so called Brown's paradoxon [175].

Table 4.3: The magnetic properties measured for 90% cold rolled plus different temperatures for 60 min.

	Permeability		Power loss kJ/m^3		Coercive force A/m	
	10Hz	50Hz	10Hz	50Hz	10Hz	50Hz
Annealing at 600°C (RD)	122	125	1.40	2.70	181	316
Annealing at 600°C (TD)	79		0.65		114	
Annealing at 700°C (RD)	106	108	0.80	1.48	73	215
Annealing at 700°C (TD)	85		1.05		125	
Annealing at 900°C (RD)	79	81	0.82	1.47	99	257
Annealing at 900°C (TD)	73		0.58		86	
Annealing at 1100°C (RD)	93	96	0.83	1.83	96	297
Annealing at 1100°C (TD)	42		0.60		108	

According to the change of the crystallographic texture an effect on magnetic materials properties can be seen in Fig. 4.37 showing the dependence of the texture components developed after full recrystallization and grain growth on the permeability and power loss. It can be seen that the permeability is decreasing with increasing annealing temperature due to an increasing of texture components (112)[7 -11 2] while the power loss decreases with increasing the annealing temperature up to 900°C. Exceeding this annealing temperature (up to 1100°C) causes a rise in the power loss in spite of the improvement of the texture. Also, the increasing the annealing temperatures for full recrystallization process for 60 min caused decreased on the permeability. However, the permeability is connected with the number of active domain walls, which is dependent on impurities and crystal defects. Additional, the determinative effect of thermal stresses by rapid heating to high temperatures on the magnetic properties of fully processed electrical steels when further grain growth does not lead to improvement of the magnetic properties was shown in literature [27]. With decreasing power loss the permeability is increased for annealing temperatures up to 900°C according to the texture generation.

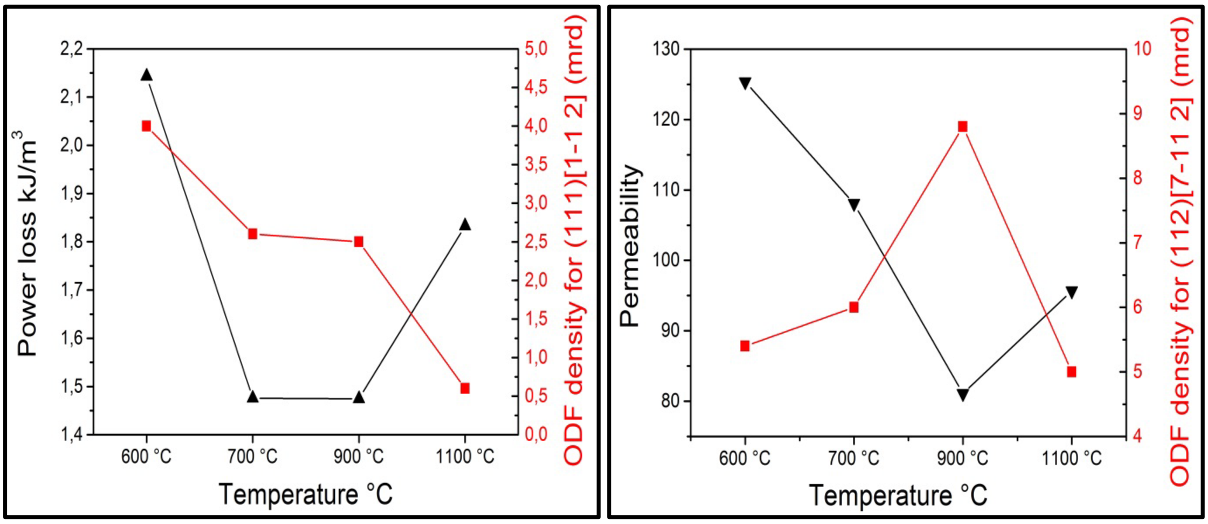

a) **b)**

Figure 4.37: The effect of two components a) (111)[1-1 2] , and b) (112)[7 -11 2] on the magnetic properties for 90% cold rolling plus different temperatures for 60 min [177]

The results of the two stages cold rolling (at 75% and 60% reduction) with intermediate annealing process leads to an increase in the permeability values and simultaneously to a decrease of power losses and coercive forces. Regarding to the values is shown in table 4.4, the annealing process with 800°C/60 min shows the highest increase in the permeability the biggest and decrease in the power losses and coercive force in both directions than the other thermal annealing processes including that ones for one stage cold rolling. According to Fig. 4.21 the mean grain size in such samples annealed at 800°C/60 min is around 75µm. The effect of cold rolling process and the degree of the plastic deformation play a crucial role in the development of the crystallographic texture and magnetic properties of Fe-2.6%Si. However, the permeability is connected with the number of active domain walls, which is dependent on impurities and crystal defects. Additional it was observed, the effecting of the heating and cooling rate on the magnetic properties are affected the magnetic properties such as permeability, power loss and coercive force. Also, the two important components for soft magnetic materials, a cube component (001)[100] and Goss component {110}<001>, can be produced by two steps cold rolling process with intermediate annealing. These components can be also developed in a one stage cold rolling process, but magnetic properties are better after using the two stages process.

Table 4.4: The magnetic properties measured for two stages cold rolling with intermediate annealing processes.

	Permeability		Power loss kJ/m^3		Coercive force A/m	
	10Hz	50Hz	10Hz	50Hz	10Hz	50Hz
Annealing at 600°C/ 60 min (RD)	116	122	1.32	2.23	172	355
Annealing at 600°C/ 60 min (TD)	108		1.10		142	
60 % Cold Rolling (RD)	84	82	2.96	3.57	420	570
60 % Cold Rolling (TD)	67		2.28		457	
Annealing at 800°C/ 60 min (RD)	121	130	1.05	1.86	106	266
Annealing at 800°C/ 60 min (TD)	91		0.76		86	

The external field has affected the crystallographic texture, microstructure and magnetic properties. Regarding to the values is shown in table 4.5, the magnetic annealing process at 14 Tesla was observed the highest increase in the permeability and decrease in the power losses and coercive force than at (0 and 7) Tesla. According to the literature [186] the high magnetic field at 14 Tesla was improved the magnetic properties if the crystallite were formed during the cooling from the melt. The orientations of crystallites are all aligned nearly parallel to the direction of final magnetization. The domain boundaries are displaced by application of an external field that the domains are elongated in the direction in which the magnetic field was applied during heat treatments [187]. The results are indicated the effect of high external field during annealing process on the grain orientation toward the external field. Also, the high external field is affected the magnetic properties particularly on the permeability. However, the permeability is connected with the number of active domain walls, which is dependent on impurities, crystal defects and the orientation of the crystals. The direction of external field is affected on the domain wall during heat treatments. The domains are distributed by changing in a size and shape of the domains by the movement of domain boundaries. This indicates domains have been stabilized parallel to the specimen's axis and then become oriented with the direction of the external field (*H*).

Table 4.5: The magnetic properties measured for magnetic annealing samples at 10Hz.

	Permeability	Power loss kJ/m^3	Coercive force A/m
0 Tesla (RD)	38	0.71	136
7 Tesla (RD)	33	1.17	241
14 Tesla (RD)	324	0.81	132

According to the change of the crystallographic texture an effect on magnetic properties can be seen in Fig. 4.38 shows the dependence of the texture components (111)[1-12] developed after recrystallization and grain growth on the power loss. It can be seen that the power loss is decreasing with decreasing of texture components (111)[1-12].

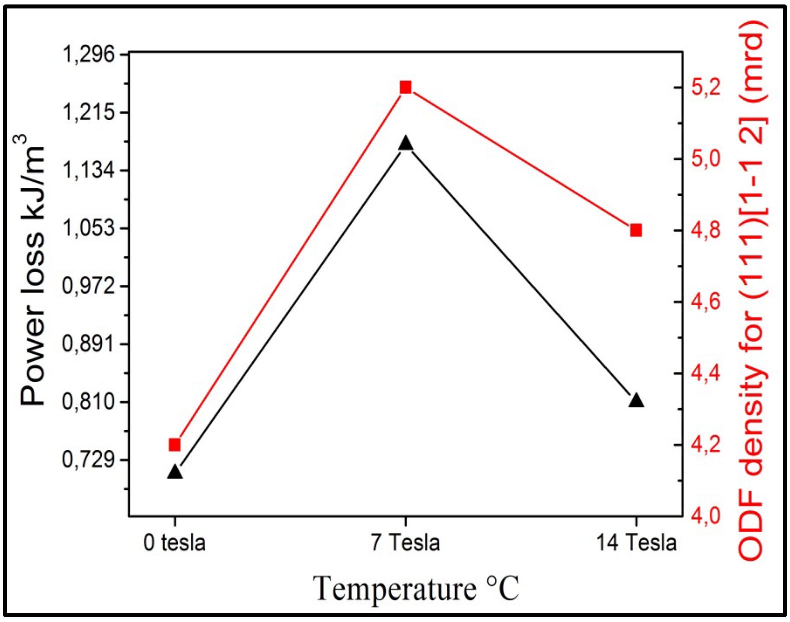

Figure 4.38: The effect of components (111)[1-1 2] on power loss for different magnetic annealing

4.6 Hardness

The variation of hardness values caused by the effect of different rolling process and heat treatments such as the hot rolled, (75% and 90%) cold rolled at one stage, annealing treatments after 90% one stage cold rolled at different temperature and time and two stages cold rolling with intermediate annealing process as shown in Fig. 4.39 (a and b). The results observed that the hardness strongly related to the percentage of cold rolling reduction and annealing treatments, annealing treatments induce change on the microstructure, dislocation density, magnetic properties and crystallographic texture, hardness continuously decreasing with increasing both the annealing temperature and annealing time [182]. The effect of external field on the hardness shows in Fig. 4.39c, we observed a slightly increases on hardness when increases the external field caused by the change on crystallographic texture.

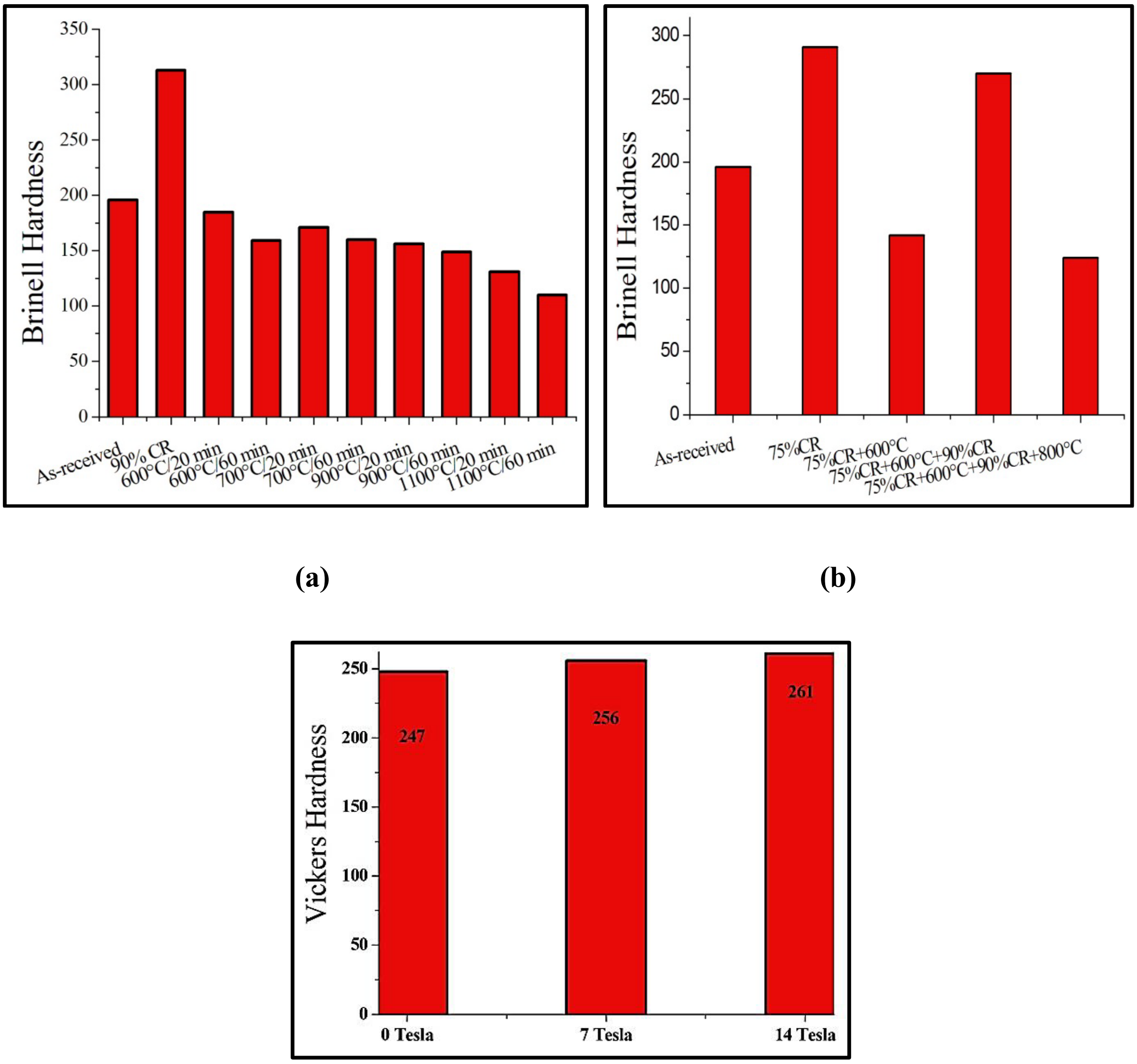

(a) **(b)**

(c)

Figure 4.39: The average hardness for **a)** 90% cold rolling plus different annealing temperature for (20 and 60) min. **b)** Two stage cold rolling processes **c)** Magnetic annealing at 600°C/60 min for different external force at (0, 7, 14) Tesla

Conclusions and Recommendations

Conclusions

The objective of this work was to investigate the effect of different cold rolling processes (Hot rolling, cross cold rolling, cross cold rolling with intermediate annealing process) and different annealing processes at different annealing temperatures, annealing time and magnetic annealing with different external fields on the crystallographic texture, microstructure and magnetic properties of Fe-2.6% Si.

The works are divided in three groups. The purpose of the first group of experiments was to study the effect of different annealing temperatures at different annealing times after 90% cold rolling on the crystallographic texture and magnetic properties.

The purpose of the second group of the experiments was to study the effect of two stages of cold rolling (at 75% and 60% reduction) with intermediate annealing process and annealed the sample at 800°C to improve the crystallographic texture and magnetic properties.

The purpose of third group of experiments was to study the effect of the magnetic annealing (annealed the sample at 600°C at different external field) on crystallographic texture and magnetic properties.

As received materials (97% hot rolled) was submitted to different sequences of cold rolling at 75% and 90% cold rolling. The results observed a strong texture component {001}<110> rotate cube components increasing after 75% and 90% cold rolling. Also the results show an increasing the intensity spread along the α fiber <110>||RD when increasing the rolling reduction.

The results of the first group of experiments shows the crystallographic texture and the magnetic properties of Fe 2.6%Si steel are strongly dependent on the annealing temperature and starting texture. Recrystallization and grain growth lead to develop a crystallographic texture in which mainly two texture components, (112)[7 -11 2] and (111)[1-1 2], can be observed affecting the magnetic properties. Also the results show an increasing the intensity spread along the γ fiber <111>||ND when increasing the temperatures.

The results pronounce at annealing of the sample for 20 minute at different temperatures up to 1100°C for 20 minute decreases in permeability values. Recrystallization and grain growth lead to develop a crystallographic texture in which mainly two texture components, (112)[7 -11 2] and (111)[1-1 2], can be observed affecting the magnetic properties. The annealing of the sample at different temperatures up to 900°C for 20 min results in a decreasing power loss while simultaneously, the intensity of (111)[1-12] decreases.

The annealing of the sample at different temperatures up to 900°C for one hour results in a decreasing permeability while simultaneously, the intensity of (112)[7 -11 2] increases. Simultaneously, also, the development of the (111)[1-12] texture component leads to a decrease of power loss coinciding with an increase in grain size.

The results of the second group of experiments shows the effect of cold rolling process plays a crucial role in the development of the crystallographic texture and magnetic properties of Fe-2.6%Si. It was observed, that the two important components for soft magnetic materials, a cube component (001)[100] and Goss component {110}<001>, can be produce by two steps cold rolling process with intermediate annealing. These components can be also developed in a one stage cold rolling process, but magnetic properties are better after using the two stage process. Additionally it was found, that not the biggest grain size produced by high annealing temperature leads to best magnetic properties.

The results of the third group of experiments shows the variation on cryptographic texture and improvement on the magnetic properties such as (a high permeability, low power loss and low coercive force) caused by the effect of external field. Also, the results observed the effect of (111)[1-12] texture components on the magnetic properties. However, the decreasing of the (111)[1-12] texture component leads to a decrease of power loss.

During different rolling process, crystallographic texture and microstructure will change heavily. The defect density is directly proportional with reduction steps increasing also the effect of rolling process we can see it’s very clearly at TEM image how the contrast is changed during rolling process.

Finally, the results are observed the effect of different rolling processes and different heat treatments at different conditions it’s very important on understanding and improving transformers steels because of the economic as well as technological profits stemming from this kind of research.

Recommendations

For further investigations in this field of study, the following areas are recommended:

1. Investigations should be carried out on Fe-2.6%Si for two stages cold rolling to 95% reduction using different intermediate annealing temperatures (600°C, 700°C, 800°C, 900°C and 1100°C).

2. After severe cold rolling (to than 95% reduction) under different external magnetic fields, the effect of intermediate annealing temperatures (600°C, 700°C, 800°C, 900°C and 1100°C) should be studied.

3. The effect of short intermediate annealing time (1 to 60 seconds) under different magnetic external field should be studied.

4. In situ tensile test of differently processed sheet should be investigated using synchrotron radiation.

5. As effect of magnetic field on the phase equilibrium of steel changes the phase transformation kinetics, further investigation of heat-treatment under even higher magnetic external fields should be studied according to the final steel microstructure.

References

[1] C. W. Chen: Magnetism and Metallurgy of Soft Magnetic Materials, Dover Publications-INC, New York, (1986).

[2] R. M. Bozorth: Ferromagnetism, IEEE Press, New York, (1978).

[3] J. T. Park, J. A. Szpunar, Acta Mater, vol. 51, (2003), pp. 30-37.

[4] M. A. da Cunha, Sebastio C. Paolinelli, Effect of the annealing temperature on the structure and magnetic properties of 3% Si non oriented steel, Journal of magnetism and magneticm materials, vol. 254-255, (2003), pp. 379-381.

[5] P. Weiss and R. Forrer, Ann. Phys., vol. 12, (1929), pp. 297-321.

[6] H. J. Bunge and C. Esling, Advances and application of quantitative texture analysis, papers presented at a course of advance instruction, (1989), Clausthal (FRG).

[7] G. Krauss, Steel processing, structure and performance, ASM international, Book (2005).

[8] P. W. Schilk, J. J. Pepe and R. C. Schwant in 77th Steel bar Product Guidelines, ISS, Warrendale, PA, (1994), pp. 1–10.

[9] G. Frommeyer, U. Bruex and P. Neumann, Supra-ductile and high-strength manganese-TRIP/TWIP steels for high energy absorption purposes. ISIJ International, vol.43, No.3, (2003), pp. 438-446

[10] W. Ozgowicz, A. K .Lisiecka and A. Grajcar, Corrosion Behavior of Cold Deformed Austenitic Alloys, doi.org.10.5772.53590.

[11] O. Fischer and J. Schneider, influence of deformation process on the improvement of no-oriented electric steel, vol.254-255, (2003), pp. 302-306.

[12] J. S. Kallend, U. F. Kocks, A. D. Rollett and H. R. Wenk: Materials Science and Engineering, vol. A132, (1991), pp. 1-11.

[13] R. P. Kumar, I. Samajdar, N. N. Viswanathan, V. Singal and V. Seshadri: Journal of Magnetism and Magnetic Materials, vol. 264(1), (2003), pp. 75-80.

[14] N. P. Goss, New Development in Electrical Strip Steels Characterized by Fine Grain Structure Approaching the Properties of a Single Crystal, Transactions of the American Society for Metals, vol. 23,(1935), pp. 511-531.

[15] G. Wasserman, J. Ggrewen: Texturen metallischer Werkstoffe.2 aufl. Springer Verl. Berlin/Göttingen/Heidelberg (1972).

[16] B. D. Culity and C. D Graham, Introduction to magnetic materials, IEEE press. 2009 book

[17] P. Van Houtte, L. Delannay, I. Samajdar, Texture and Microstructure. vol. 31, (1999), pp. 109-149.

[18] H. Hsun, texture of metals, Texture, vol. 1, (1974), pp. 233-258

[19] L. K. Varga, H. A. Davies, Challenges in Optimization the Magnetic properties of Bulk soft Magnetic Materials, Journal of Magnetism and Magnetic Materials, vol. 320, (2008), pp. 2411-2422.

[20] P. Gobermado, R. Detrov, D. Ruiz, E. leunis and L. A. I. Kestens, Texture evaluation in Si-Alloyed ultra-low-carbon steels after severe plastic deformation, Adv. Eng. materials, Vol. 12, (2010), pp. 1077-1081.

[21] W. F. Barrett, W. Brown and R.A. Hadfeiled, Sci. Trans. Dublin Soc., vol.1, (1900), pp. 76.

[22] N. Takahshi and J. Harase, Recent Development of Technology of Grain Oriented Silicon Steel, Materials Science Forms, vol. 204-206, (1996), pp. 143-154.

[23] A. J. Moses, Electric steels: past present and future developments, IEE Proceedings, vol. 137(5), (1990), pp. 233-245.

[24] A. D. Rollet, M. L. Storch, E. J. Hilinski, S.R. Goodman, Metall. Mater. Trans. vol. 32A, (2001), pp. 2595-2603.

[25] F. J. G. Landgraf, S. C. Paolinelli, M. A. Cunha, M. F. de Campos, Mater. Sci. Forum, vol. 495–497, (2005), pp. 543-552.

[26] P. Baudouin, A. Belhadj, Y. Houbaert, J. Magn. Magn. Mater, vol. 238, (2002), pp. 221-225.

[27] J. A. Szpunar, in: H.J. Bunge (Ed.), Texture, Anisotropy in Magnetic Steels, Directional Properties of Materials, Cuvllier Verlag, Gottingen, (1988), pp. 129-133.

[28] J. E. May, D. Turnbull, Trans. Metall. Soc. AIME 212, (1958), pp.769-781.

[29] Z. Xia, et al., J. Magn. Magn. Mater. (2008), doi:10.1016/j.jmmm.2008.07.

[30] H.-R. Wenk, P. Van. Houtte. Texture and anisotropy, Rep. Prog. Phys, vol. 67 (2004), pp.1376-1428.

[31] H. J. Bunge. Texture Analysis in Materials Science, Cuvillier Verlage, Göttingen, (1993).

[32] H. J. Bunge, C. Esling. Quantitative Texture Analysis. DGM informationsgesellschaft, Oberursel, (1982).

[33] H. J. Bunge. Texture and magnetic properties, Texture and Microstructure, vol. 11, (1989), pp. 75-91

[34] V. Randle, O. Engler, Introduction to Texture Analysis, Macrotexture and orientation Mapping Part1, Fundamental Issues , (2000).

[35] H. J. Bunge (Ed.), Quantitative Texture Analysis, General Outline and series Expansion Methode, C. Esling, (1986).

[36] H. J. Bunge, Texture Analysis in Materials Science, Butterworth, London, (1982).

[37] O. Engler and V. Randle, Introduction to Texture Analysis, CRC Press, Book (2010).

[38] ASM, Metals Reference Book, 3rd Edition, (1993), pp. 67.

[39] H.-G. Brokmeier, S. Yi, in: W. Reimers, A. Pyzalla, A. Schreyer, H. Clemens (Eds.), Neutrons and Synchrotron Radiation in Engineering Materials Science, Weinheim, (2008), pp. 57-77.

[40] D. Raabe, Textures and Microstructures, vol. 23, (1995), pp. 115-129.

[41] H. J. Bunge, Zeit. Metallkunde, vol. 56, (1965), pp. 872.

[42] H. J. Bunge, Zeit. Metallkunde, vol. 70, (1979), pp. 411.

[43] H. J. Bunge, D. Schleusener, D. Schläfer, Neutron diffraction texture studies of recrystallization in cold rolled low-C steel, Metal. Sci., vol. 8, (1974), pp.413-423.

[44] R. D. Williams, Appl. Phys., vol. 39, (1968), pp. 4297-4329.

[45] D. Ruer, R. Baro, Adv. X-ray Anal., vol. 20, (1977), pp. 187-200.

[46] J. Imhof, Zeit. Metallkunde, vol. 68, (1977), pp. 37-39.

[47] J. Hansen, J. Pospiech and K. Lücke, Tables for Texture Analysis of Cubic Crystals, Springer-Verlag, Berlin (1978).

[48] K. Pawlik, Phys. Stat. Sol. B, vol. 134, (1986), pp. 477-483.

[49] K. Pawlik, J. Pospiech, K. Lticke, in: Proc. of ICOTOM 9, H. J. Bunge (Ed.), vol. 14, (1991), pp. 25.

[50] U. F. Kocks; Texture and Anisotropy: Preferred Orientations in Polycrystals and Their Effect on Materials Properties, Cambridge University Press, 1998.

[51] R. J. Roe: Journal of Applied Physics, vol.36, (1965), pp.2024-2031.

[52] M. Z. Quadir and B. J. Duggam, Acta materalica, vol. 52, (2004), pp.4011-4021.

[53] H. J. Bunge, M. Dahms, The Iterative Series-Expansion Method for quantitative Texture analysis, J. Appl. Cryst., vol. 22, (1989), pp. 439-447.

[54] F. Wever, Z. f. Physik, vol. 28, (1924), pp. 69-80.

[55] L. G. Schultz, J. Appl. Phys. vol. 20B, (1949), pp. 1030-1033.

[56] B. N. Brockhouse , Can. J. Phys. vol. 31, (1953), pp. 339-355.

[57] J. Tobisch, M. Betzl, , and P. Reichel, , Z. Exp. Techn. Phys., vol. 5, (1969), pp. 391.

[58] J. Szpunar, J. Mater. Sci., vol. 19, (1984), pp. 3467.

[59] P. I. Welch, Experimental Techniques of Texture Analysis (Ed. H.-J. Bunge), DGM Inf. Ges., Oberursel, Germany, (1986), pp. 183.

[60] H.-R. Wenk, J. Appl. Crystallogr., vol. 24, (1991), pp. 920.

[61] H.-R. Wenk, Rev. Mineral. Geochem., vol. 63, (2006), pp. 399.

[62] H.-G. Brokmeier, Physica B, vol. 385–386, (2006), pp. 623

[63] B. D. Cullity; Elements of X-Ray Diffraction, Prentice Hall, New Jersey, (2001).

[64] G. E. Bacon, Neutron Diffraction, Claren Don Press. Oxford, Book (1975).

[65] G. E. Bacon, X-ray and Neutron Diffraction, Per Gamon Press, Book (1966).

[66] F. Hipprt, E. Geisslr, J. Hodeau, E. Lelevre and J-R. Regnard, neutron and X-ray spectroscopy, Springer, Book (2006).

[67] H.-G. Brokmeier. advances and applications of neutron texture analysis. Texture and Microstructure, vol. 33 (1999), pp. 13-33.

[68] H.-G.Brokmeier. Neutrons Diffraction Texture Analysis of Multi–Phase System, Textures and Microstructure. vol.10, (1989), pp. 325-346.

[69] H.-G. Brokmeier, Physical B, vol. 234-236, (1997), pp. 977-979.

[70] H. J. Bunge, Advantages of Neutron Diffraction in Texture Analysis, Textures and Microstructures, vol. 10, (1989), pp.265-307.

[71] H. Ashauer, A. Fleischman, C. Schanzer, E. Steichele, Physica B, vol. 283, (2001), pp.323-329.

[72] W. Brefeld and P. Gürtler in: Handbook on Synchrotron Radiation, edited by S. Ebashi, M. Koch, and E. Rubinstein (Elsevier Science Publishers, Amsterdam 1991)

[73] R. E. Watson and M. L. Perlman: Science, vol. 199, (1978), pp. 1295-1302.

[74] G. Höhler, J. Kühn, T. Müller, A. Ruckenstein, F. Steiner, J. Trümper, P. Wölfle: Nuclear Condensed Matter Physics with Synchrotron Radiation Springer Tracts in Modern Physics, (2004).

[75] H. F. Poulsen and D. J. Jensen, Mater. Sci. Forum., vol. 408–412, (2002), pp. 49-66.

[76] H. J. Bunge, L. Wcislak, H. Klein, U. Garbe, R. Nowak and J.R. Schneider. Orientation Imaging of Crystals in Polycrystalline Materials. Adv. Eng. Mater. vol. 4 , (2002), pp. 300-305.

[77] H. J. Bunge and R. A. Schwarzer. Orientation StereologyA new Branch in Texture Research. Adv. Eng. Mater. vol. 3, (2001), pp. 25-39.

[78] H.J. Bunge, L. Wcislak, H. Klein, U. Garbe and J.R. Schneider. Texture and Microstructure Imaging in Six Dimensions with High-Energy Synchrotron Radiation. J. Appl. Cryst. vol. 36, (2003), pp.1240-1255.

[79] H.J. Bunge, H. Klein, L. Wcislak, U. Garbe, W. Weiß and J.R. Schneider. Texture and Microstructure, vol. 35, (2003), pp. 253-271.

[80] H. F. Poulsen and D. J. Jensen, in Proceedings of the 16th International Symposium (Eds. N. Hansen et al.), Riso National Laboratory, Roskilde, Denmark, (1995), pp.503.

[81] F. Heidelbach, C. Riekel and H.-R. Wenk, J. Applied Crystallography. vol. 32, (1999), pp. 841-849.

[82] W. Reimers, A. R. Pyzalla, A. Schreyer and H. Clemens, Neutrons and Synchrotron radiation in Engineering materials Science, Wiley , Book (2008).

[83] F. J. Humphreys, M. Hatherly: Recrystallization and Related Annealing Phenomena, Elsevier, (2004).

[84] M. Hatherley and W. B. Hutchinson, An Introduction to Textures in Metals, Chamelon Press Ltd., London, (1979).

[85] J. Barros, J. Schneider, K. Verbeken, Y. Houbaert, On The Correlation Between Microstructure and Magnetic Losses in Electric Steel, JMMM, vol. 320, (2008), pp. 2490-2493.

[86] H. Shimanaka, Y. Ito, K. Matsumur and Fukuda, Recent Develoment of Non-Oriented Electric Steel Sheets, J. Mag. Magn. Mat., vol. 26, (1982), pp.57-64

[87] D. Vanderschueren, L. Kestens, P. van Houtte, E. Aernoudt, J. Dilewijns, U. Meers, The Effect of Cross Rolling on Texture and Magnetic Properties of Non-Oriented Steels, Texture and Microstructure, vol. 14-18, (1991), pp. 921-926.

[88] R. Petrov, L. Kestens, A. Wasilkowska, Y. Houbaert, Microstroucture and Texture of Lightly Deform TRIP-Assisted Steel Characterized by Means of The EBSD Technique, Material Science and Engineering A, vol. 447, (2007), pp.285-297.

[89] T. Tomida., S. Uenoya and N. Sano, Fine-Grained Doubly Oriented Silicon Steel Sheets and Mechanism of Cube Texture Development, Materials Transactions, vol. 44, (2003), pp. 1106-1115.

[90] H. Homma, S. Nakamura and N. Yoshinaga, On {h, 1, 1}<1/h, 1, 2> The Recrystallization Texture of Heavily Cold Rolled BCC steel, Materials Science Forum, vol. 467-470, (2004), pp. 269-274.

[91] J. Sidor, A. Mirox, R. Petrov and L. Kestens, Microstructural and Crystallographic Aspects of Conventional and Asymmetric Rolling Process, Act Materialia, vol. 56, (2008), pp. 2495-2507.

[92] R. Petrov, L. Kestens, K. Verbecken and Y. Houbaert, Grain Growth after Intercritical rolling, materials Science forms, vols. 467-470, (2004), pp. 305-310.

[93] P.G. Xu, Y. Tomota, H. Suzuki, T. Suzuki, S. Machiya and F. X. Yin, Bulk Texture Measurement of Interstitial-Free Annealed Steel using Gaussian Integrated Intensities of Neutron Diffraction Spectra, Materias Transactions, vol. 49, No.9, (2008), pp. 2033-2039.

[94] R. K. Khatirkar, S Kumar, Comparison of Recrystallization Textures in Interstitial Free and Interstitial Free High Strength Steels, Materials Chemistry and physics, vol. 127, (2011), pp.128-136.

[95] Y. Onuki, R. Hongo, K. Okayasu, H. Fukutomi, Texture development in Fe-3% Si during high-temperature deformation, Acta Materialia, vol. 61, (2012), pp.1294-1302.

[96] J. Asensio, G. Romano, V. J. Martiez, J. I. Verdeja, J. A. Pero-sanz, Ferritic Steels Optimization of Hot-Rolled Textures Through Cold Rolling and Annealing, Materials Characterization, vol. 47, (2001), pp.119-127.

[97] K. Lee, G. Kim and L. Kestens, Effect of Initial Texture on The Evolution of Texture and Stored Energy During Recrystallization of Interstitial Free Steel, Materials Science Forum, vols. 495-497, (2005), pp. 357-362.

[98] K. Verbeken, L. Kestens, Oriented Nucleation and Selective Growth during Secondary Recrystallization in Ultra Low Carbon steel, Materials Science Forum, vol. 467-470, (2004), pp. 941-948.

[99] T. Nguyen Minh, J. Sidor, R. Petrov, L.A.I.Kestens, Texture Evaluation During Asymmetrical Warm Rolling and Subsequent Annealing of Electrical Steel, Materials Science Forum, vol. 702-703, (2012), pp.758-761.

[100] M. A da Cnha, S. C. paolinelli, Evolution of Non-Oriented Silicon Steel Texture on Recrystallization and Grain Growth, Materials Science Forum, vol. 467-470, (2004), pp. 869-874.

[101] B. Y. Huang, K. Yamamoto, C. Kaido, and Y. Yamashiro, The Effect of Cold Rolling on The Magnetic Properties of Non-Oriented Silicon Steel Sheets, IEEE, vol. 35, (1999), pp. 3376-3378.

[102] Y. Sidor, F. Kovac, T. Kvackaj, Grain Growth Phenomena and Heat Transport in Non-Oriented Electric Steels, Acta Materialia, vol. 55, (2007), pp.1711-1722.

[103] L. Seidel, M. Hölscher and K. Lücke : Rolling and recrystallization Textures in Iron-3% Silicon, Textures and Microstructures, vol. 11, (1989), pp.171-185

[104] E. J. Gutierrez-Castaneda, A. Salinas-Rodriguez, Effect of Annealing Prior to Cold Rolling on Magnetic and Mechanical Properties of Low Carbon Non-Oriented Electric Steels, JMMM, vol. 323, (2011), pp. 2524-2530.

[105] B. Y. Huang, K. Yamamoto, C. Kaido, and Y. Yamashiro, The Effect of Cold Rolling on The Magnetic Properties of Non-Oriented Silicon Steel Sheets (part II) , IEEE, vol. 209, (2000), pp. 197-200.

[106] O. Hubert, L. Daniel, R. Billardon, Experimental Analysis of the Magneto Elastic Anisotropy of a Non-Oriented Silicon Iron Alloy, JMMM, vol. 254-255, (2003), pp. 352-354.

[107] B. B. Rath, Recrystallization Texture in Iron Crystals, ICTOM, Vol.7, (1984), pp. 281-286.

[108] M. Matsuo, H. Hayakawa and S. Hayami, Texture Formation In Continuous Annealing with Emphasis on the Effect of Coiling Temperature of Hot Strip, ICTOM, vol.7, (1984), pp. 275-284.

[109] M. Takahashi and A. Okamoto, Effect of Nitrogen Content on Recrystallization Textures of Low-Carbon Steel Sheets, Texture Formation in Continuous Annealing with Emphasis on The Effect of Coiling Temperature of Hot Strip, ICTOM, vol.7, (1984), pp. 265-274.

[110] U. Frhr. V. Schlippenbach and K. Lücke, Deformation and Recrystallization Textures in Low-C-Steel Texture Formation in Continuous Annealing with Emphasis on The Effect of Coiling Temperature of Hot Strip, ICTOM, vol.7, (1984), pp. 159-164.

[111] W. Österle, Influence of Temperature and Impurity Content on the Development of Texture and Microstructure of Cold Rolled Iron, Texture Formation in Continuous Annealing with Emphasis on the Effect of Coiling Temperature of Hot Strip, ICTOM, vol.7, (1984), pp. 123-128.

[112] K. Lücke, The Formation of Recrystallization Textures in Metals and Alloys, Texture Formation in Continuous Annealing with Emphasis on The Effect of Coiling Temperature of Hot strip, ICTOM, vol.7, (1984), pp. 195-210.

[113] H. J. Bonge, H. P .Lee, E. Dahlem, Growth Selection Texture Changes During Continuous Grain Growth, ICTOM, vol.7, (1984), pp. 217-220.

[114] Hsun Hu, Mechanism of Recrystallization Texture Formation in Deep Drawing Steel, ICTOM, vol.7, (1984), pp. 1-20.

[115] M. Konishi, T. Obara, T. Tanaka and N. Ohashi, Effect of Heat Prior to Cold Rolling on Recrystallization Texture in Iron Carbon Single Crystals, Texture of materials, vol 2, (1978), pp. 255-264.

[116] C. S. Barrett and T. B. Massalski, structure of metals , 3rd. ed. (McGraw-Hill, New York), Book (1966)

[117] A. E. Berkowitz and E. Kneller., Magnetism and Metallurgy, Academic Press , Vol. 2, Book (1969).

[118] R. M. Bozorth, Feromagnetisim , van Nostrand, New York, Book (1951).

[119] R. E. Reed-Hill, Physical Metallurgy Principles, D. van Nostrand Co., New York, 2nd ed., Book (1973).

[120] J. Smit, Magnetic properties of materials, McGraw-Hill Book co., New York, Book (1971).

[121] K. H. J. Boschow, Handbook of magnetic materials, Elsevier, Vol. 8, (1995).

[122] H. Kronmüller, S. Parkin, Handbook of Magnetism and Advance Magnetic Materials, J. Wiley and Sons, Book (2007).

[123] A. Hubert, R. Schäfer, Magnetic Domains, Springer, Book (1998).

[124] E. D. Torre, Magnetic Hysteresis, IEEE Press, Book (1999).

[125] N. A. Spaldin, Magnetic materials fundamentals and applications, Cambridge, Book (2010).

[126] W. D. Callister, Jr. David G. Rethwisch , Materials Science and Engineering an Introduction, Book (2009).

[127] N. Masahashi, M. Matsuo and K. Watanabe: Journal of Materials Research, vol. 13, (1998), pp. 457-461.

[128] T. Watanabe, Y. Suzuki, S. Tanii and H. Oikawa: Philosophical Magazine Letters, vol. 62, (1990), pp. 9-17.

[129] T. Matsuzaki, T. Sasaki, S. Tsurekawa and T. Watanabe: The Forth International Conference on Recrystallization and Related Phenomena, The Japan Institute of Metals, (1999).

[130] B. G. Kim and S.D. Park: Journal of Korean Institute of Metal and Materials, vol. 39, (2001), pp. 1284-1289.

[131] W. W. Mullins: Acta Metallurgica, vol.4, (1956), pp. 421-432.

[132] A. D. Sheikh-Ali, D. A. Molodov and H. Garmestani: Scripta Materialia, vol. 46, (2002), pp. 857-862.

[133] Y. N. Markov and R. A. Adamescu: Fizika Metallurgica and Metalloved, vol. 32, (1971), pp. 800.

[134] H. O. Martikainen and V.K. Lindroos: Scandinavian Journal of Metallurgy, vol.10, (1981), pp. 3-8

[135] J. K. Choi, H. Ohtsuka, Y. Xu and W. Y. Choo: Scripta Materialia, vol.43, (2000), pp. 221-226.

[136] S. Nakaura and H. Homa, Matter Science Forum, vol. 467-470, (2004), pp. 269-274.

[137] R. E. Rad-Hill, Physical Metallurgy Principles, Von Nostrand Reinhold, Book (1973).

[138] D. R. Askeland, P. P. Fulay and W.J. Wright, The Science and Engineering of Materials, Book (2011).

[139] A. Nafalski, Magnetic Materials and Magnetic Techniques, Electric Engineering, vol. 8, (2004), pp. 159-166.

[140] T. Unger, J. Gubicza, G. Ribarik and A. Borbely, j. Appl. Cryst., vol. 34, (2001), pp. 298-310.

[141] G. K. Williamson and W. H. Hall, Acta Metall. vol. 1, (1953), pp. 22-25.

[142] B. E. Warren, Prog. Met. Phys. vol. 8, (1959), pp. 147-202.

[143] B. E. Warren and B. L. Averbach, J. Appl. Phys. vol. 21, (1950), pp. 595-595.

[144] M. Wilkens, phys. stat. sol. vol.2, (1970), pp.359-370.

[145] T. Ungár and A. Borbeály, Appl. Phys. Lett., vol. 69, (1996), pp. 3173-3175.

[146] A. J. C. Wilson, Nouvo Cimento, vol.1, (1955), pp. 277-283.

[147] H.-G. Brokmeier, W. M. Gan, C. Randau, M. Völler, J. Rebelo-Kornmeier, M. Hofmann, Nucl. Ins. and Metho. in Phys. Resear., vol. A642, (2011), pp. 87-92.

[148] M. Hofmann, R. Schneider, G. A. Seidle, J. Rebelo-Kornmeier, R. C. Wimpory, U. Garbe, H.-G. Brokmeier, physica B, vol. 385-386, (2006), pp.1035-1037.

[149] J. Tobisch and H. J. Bunge, The Sepherical Sample Methode in Neutron Diffraction Texture Determination, Texture, vol. 1, (1972), pp. 125-127.

[150] C. Randau, U. Garbe, H.-G. Brokmeier, J. Appl. Crystallogr, vol. 44, (2011), pp. 641-646.

[151] H. J. Bunge, H. Klein: Z. Metallkunde, vol. 87, (1996), pp.465-475.

[152] M. Z. Salih, Z.Y. Zhong , H.G. Brokmeier B. Schwebke and N. Schell, The Effect of Cold Rolling and Annealing on line Broadening of Fe2.6%Si, Desy Annoual Report (2012).

[153] M. Anhalt and B. Weidenfeller, Theoretical an Experimental Approach to Characteristic Measurement Data of Polymer Bonded Soft Magnetic Composites, Journal of Applied Physics, vol. 105, (2009), 113903.

[154] R. Kern, H. P Lee, H. J. Bunge, The Rolling Texture of Iron of different purities, Steel Research, vol. 57, (1986), pp. 365-571.

[155] R. Kern: Prakt. Metallogr., Vol. 21, (1984), No.6, P. 273-293.

[156] John J. Jonas, Transformation Textures Associated with Steel Processing, Microstructure and Texture of Steel Conferences, (2008).

[157] L. Kestens, S. Jacobs, Texture Control During the Manufacturing of non-oriented Electrical Steels, Texture, Stress, and Microstructure, (2008), doi 10.1155/2008/173083.

[158] L. Kestens and J. J. Jonas, Transformation and Recrystallization Textures Associated with Steel Processing, in Metal working: Bulk forming, S. L. Semiatin, Ed., vol. 14A of ASM handbook, (2005), pp. 685-700, ASM International, Materials park.

[159] H. Inagaki, Stable end orientations in the rolling textures of the polycrystalline Iron, Zeitschrift für Metallkunde, vol. 87, (1987), pp. 431-439.

[160] G. Gottstein and K. lücke, Texture of materials, vol 2, (1978).

[161] P. Van Houtte. Manual of MTM-FHM, MTM- Kuleuvent, Belgium, (1982).

[162] I. Samjdar, B. verlinden, P. Van houtte, ISIJ Int. 38, (1998), pp.759-765.

[163] H. Denma, Y. Ishihara, T. Todaka and M. Doi: Journal of Magnetism and Magnetic Materials, vol. 215, (2000), pp. 106-109.

[164] E.T. Stephenson and A.R. Marder: IEEE Transactions on Magnetics, vol. Mag-22, (1986), pp. 101.

[165] F. J. G. Landgraf, J. C. Teixeira, M. Emura M, M.F. de Campos and C. S. Muranaka: Materials Science Forum, vol. 303-302, (1999), pp. 440.

[166] K. Matsumura and B. Fukuda: IEEE Transactions on Magnetics, vol. Mag-20, (1984), pp. 1533-1538.

[167] D. Schläfer and H. J. Bunge, neue Hütte, vol. 18, (1973), pp. 299.

[168] R. Kern, J. Grwen and H. J. Bunge, Development of The Recrystallization Texture and Microstructure of High Purity Iron, ICTOM 7, (1984), pp. 221-262.

[169] U. Frhr. V. Schlippenbach and K. lücke, Texture of materials, vol 2, (1978).

[170] I. C. Dragomir and T. Ungar, Powder Diffraction, vol.17, (2002), pp. 104-111.

[171] H. Zhang, M. P. J. Punkkinen, Börje Johansson, S. Hertzman and L. Vitos, Single-Crystal Elastic Constants of Ferromagnetic Bcc Fe-based Random Alloys from first-principles theory, DOI : 10.1103/PhysRev B.81.184105 (2010).

[172] A. Borbély, I. Dragomir-Cernatescu, G. Ribárik and T. Ungár: “Computer program ANIZC and Trigonal Crystals”, In J. Appl. Cryst., vol. 36, (2003), pp.160-162.

[173] B. Weidenfeller, W. Riehemann, Effects of surface treatments on the hysteresis losses of GO iron silicon steel, Journal of Magnetism and Magnetic Materials, vol. 292, (2005), pp. 210-214.

[174] B. Weidenfeller, W. Rieheman, Domain Refinement and Domain wall Activation of Surface Treated Fe-Si sheets Journal of Magnetism and Magnetic Materials, vol. 160, (1996), pp. 136-138.

[175] B. Weidenfeller, W. Riehemann, Effects of Surface Treatments on The Hysteresis Losses of GO Iron Silicon Steel, Journal of Magnetism and Magnetic Materials, vol. 292, (2005), pp. 210-214.

[176] T. Shimazu, M. Shiozaki and K. Kawasaki, Effect of Temper Rolling on Texture Formation of Semi-Processed Non-Oriented Steel, Journal of Magnetism and Magnetic Materials, vol. 133 , (1994), pp.147-149.

[177] M. Z. Salih, B. Weidenfeller, N. Al-hamdany, H.-G. Brokmeier and W. Gan, Magnetic Properties and Crystallographic Texture of Fe-2.6% Si after 90% Cold Rolling Plus Different Annealing, Journal of Magnetism and Magnetic Materials, vol. 354, (2014), pp. 105-111.

[178] R. Smoluchowski and R. W. Turner: J. Appl. Phys. vol. 20, (1949), pp. 745–746.

[179] V. S. Bhandary and B. D. Cullity: Trans. Metall. Soc. AIME 224 (1962), pp.1194–1200.

[180] H. O. Martikainen and V. K. Lindroos: Scand. J. Metall., vol. 10, (1981), pp.3-8

[181] C. S. He, Y. D. Zhang, X. Zhao, L. Zuo, J. C. He, K. Watanabe, T. Zhang, G. Nishijima and C. Esling: Adv. Eng. Mater., vol. 5, (2003), pp. 579–583.

[182] C. S. He, Y. D. Zhang, X. Zhao, L. Zuo and C. Esling: Mater. Sci. Forum, vol. 495–497, (2005), pp. 465-470.

[183] D. A. Molodov, S. Bhaumik, X. Molodova and G. Gottstein: Scripta Mater., vol. 54, (2006), pp. 2161-2164.

[184] S. Bhaumik, X. Molodova, D. A. Molodov and G. Gottstein: Scripta Mater., vol. 55, (2006), pp. 995-998.

[185] H. O. Martikainen, V. K .Lindroos, Scandinavian Journal of Metallurgy., vol. 10, (1981), pp. 3.

[186] M. McCaig, Magnetostriction of Anisotropy Permanent Magnet Alloys. Proc. Phys. Soc., vol. B62, (1949), pp. 652-658.

[187] E. A. Nesbitt, Mechanism of Magnetization in Alnico, Phys. Rev., vol. 80, (1950), pp.112-115.

[188] M. Z. Salih, B.Weidenfeller, N. Al-hamdany, H.-G. Brokmeier and W. M. Gan, Journal of Magnetism and Magnetic Materials, vol. 362, (2014), pp. 141-149.

Curriclum Vitae

Salih, Mohammed Zakria Salih

Personal Information

Surname, name:	Salih, Mohammed Zakria Salih
Sex:	Male
Date of birth:	27.04.1983
Place of birth:	Baghdad, Iraq
Nationality:	Iraqi
Marital status:	Single
Address:	Teichberg 25 21502, Geesthacht, Germany
Tel.:	+49 (0) 151 4 55 33 111
E-mail:	mohammedzs2007@hotmail.com dr.mohammed.zakria.salih@outlook.com

Academic Qualifications

09/2001– 06/2004	Bachelor degree Mechanical Engineering Al-Nahrain University
09/2004 – 08/2007	M.Sc. degree Applied Mechanical Engineering Al-Nahrain University
Since 10/2010	PhD student Institute of Materials Science and Engineering Clausthal University of Technology - Germany

Employment

04/2007 – 07/2008	Maintenance junior at Caterpillar Company
09/2008 – 06/2010	Teaching assistant at Al-Mansour collage University at Department, Faculty of Engineering : - Software Engineering - Computer Communication Engineering - Computer Technology Engineering
Since 10/2010	Research assistant at the Institute of Materials Science and Engineering Clausthal University of Technology-Germany

Research Experience

- Crystallographic texture and Residual stress measurement by using laboratory X-ray, and neutron diffraction
- In situ tensile test and phase analysis by using synchrotron radiation
- Improvement of magnetic properties for Steels and Steels alloys by using different thermo-mechanical processes

Research Interests

- Analysis of X-ray line profile to study micro-strains and crystal defects produced in surface layers after performing mechanical surface treatments on Steel alloys
- Use of electron backscatter diffraction (EBSD) to study crystal orientation mapping, crystal defects and grain boundaries in Steel alloys after performing severe plastic deformation (SPD)

Work Responsibilities

- Measurement of residual stress and crystallographic texture by using X-ray diffraction, hard X-ray (Synchrotron) and Neutron diffraction
- Phase analysis of various alloys by using X-ray diffraction
- Teaching assistant for “X-ray and Neutron Diffraction” course

Geesthacht, den 17.07.2014

Mohammed Zakria Salih

Publications

Year	Publications
2012	M. Z. Salih, Z. Y. Zhong, H.-G. Brokmeier, B. Schwebke and N. Schell, The effect of cold rolling and annealing on the broadening of Fe-2.6%Si, Annual Desy report 2012.
	M. Z. Salih, N. Al-hamdany, Z. Y. Zhong, H.-G. Brokmeier, B. Schwebke and N. Schell, The effect of rolling degree on Fe-2.6%Si, Annual Desy report 2012.
2013	M. Z. Salih, H.-G. Brokmeier, B.Weidenfeller, Z. Y. Zhong, N. Al-hamdany, B. Schwebke, N. Schell and W. M. Gan, Influence of the cold rolling process on texture and magnetic properties of Fe-2.6%Si, HASYLAB user meeting 2013.
	N. Al-hamdany, H.-G. Brokmeier, Z. Y. Zhong, B. Schwebke, M. Z. Salih and N. Schell, Texture inhomogeneity through the thickness for copper tube, HASYLAB users meeting 2013.
	H. -G. Brokmeier, Z. Y. Zhong, M. Z. Salih, M. Jang, B. Schwebke, N. Schell, T. Lippmann, E. Maawad, W. M. Gan, Texture Analysis at HEMS and Harwi II.
	M. Z. Salih, B.Weidenfeller, N. Al-hamdany, H.-G. Brokmeier and W. M. Gan, Magnetic properties and crystallographic texture of Fe-2.6% Si after 90% cold rolling plus different annealing, Journal of Magnetism and Magnetic Material, vol 354, (2014), pp. 105-111
	M. Z. Salih, B.Weidenfeller, N. Al-hamdany, H.-G. Brokmeier and W. M. Gan, The effect of intermediate annealing between cold rolled steps on crystallographic texture and the magnetic properties of Fe-2.6% Si, Journal of Magnetism and Magnetic Materials, vol. 362, (2014), pp. 141-149.
2014	-M. Z. Salih, H.-G. Brokmeier, B.Weidenfeller, Z. Y. Zhong, N. Al-hamdany, B. Schwebke, N. Schell and W. M. Gan, Magnetic properties and crystallographic texture of Fe-2.6 % Si after different thermo-mechanical treatment, HASYLAB user meeting 2014.
	M. Z. Salih, H.-G. Brokmeier, M. Uhlarz, B. Weidenfeller, Z. Y. Zhong, N. Al-hamdany, B. Schwebke, N. Schell and W. M. Gan, The effect of magnetic annealing on crystallographic Texture and microstructure of Fe-2.6%Si on crystallographic texture and microstructure of Fe-2.6 % Si, HASYLAB user meeting 2014.
	E. Maawad, H.-G. Brokmeier, Z. Y. Zhong, N. Al-hamdany, M. Z. Salih, L. Wagner and N. Schell, Determination of polycrystalline diffraction elastic constants of Ti-2.5Cu by using in-situ tensile loading and synchrotron radiation, Material Science and Engineering A, vol. 594, (2014), pp. 62-67.
	H. AL-khazraji, M. Z. Salih, Z. Zhong, M. Mhaede, H.-G. Brokmeier, N. Schell, and L. Wagner, Estimation of Dislocation Density in Cold Rolled CP-Titanium By Using Synchrotron diffraction, Metallurgical and materials transactions B, accepted (2014).